

UNIVERSITY OF CALIFORNIA,
IRVINE

Spin torque driven magnetization dynamics in nanoscale magnetic tunnel junctions

DISSERTATION

submitted in partial satisfaction of the requirements
for the degree of

DOCTOR OF PHILOSOPHY

in Physics

by

Chengcen Sha

Dissertation Committee:
Professor Ilya Krivorotov, Chair
Professor Zuzanna Siwy
Professor Wilson Ho

2018

© 2018 Chengcen Sha

DEDICATION

To My parents, Zhenglian and Wenyu.

TABLE OF CONTENTS

	Page
LIST OF FIGURES	v
LIST OF TABLES	xi
ACKNOWLEDGMENTS	xii
ABSTRACT OF THE DISSERTATION	xiii
1 Introduction	1
2 Background	3
2.1 Spintronics	3
2.2 Tunnel Magnetoresistance	4
2.3 Spin transfer torque	7
2.4 Magnetic Switching	10
2.5 Magnetic Tunnel Junctions	12
2.5.1 Critical Switching Voltage	16
2.6 Ferromagnetic Resonance	17
2.7 Spin-torque Ferromagnetic Resonance	20
3 Field-Modulated Spin-torque Ferromagnetic Resonance	21
3.1 Spin-torque Ferromagnetic Resonance	21
3.2 Experimental Technique	23
3.3 Gilbert Damping Evaluation	26
3.4 Continous wave Micromagnetic Simulations	31
3.5 Micromagnetic Simulations of higher order modes	38
3.6 Circular STT-MRAM Devices with Broken Symmetry	42
3.7 Possible Origin of WER Correlation with ST-FMR	49
3.8 Field Modulated Mag-noise Measurement	50
3.9 In-plane ST-FMR measurement and Mode identification	56
3.10 Angular Dependence ST-FMR Measurement	60
4 Time-domain measurement of spin-torque switching in MTJs	67
4.1 Experimental Setup	68
4.2 Results and Discussion	70

5 Write Error Rate measurement	75
5.1 Experimental Setup	76
5.2 Results and Discussion	81
6 Determination of Exchange Stiffness of STT-MRAM devices with broken symmetry	84
6.1 Measurement of ST-FMR on nominal circular devices	85
6.2 Summary of Circular Devices: Experimental Data	88
6.3 Micromagnetic Simulations of the Mode Spacing	91
6.4 Study of signal amplitude of ST-FMR signal	97
6.5 Summary of Stadium shapes MTJs devices with 60 nm width	104
6.5.1 Micromagnetic simulations of stadium devices	106
6.6 Summary of stadium shapes MTJs devices with 45 nm width	110
Bibliography	114
A Appendix Title	123
A.1 Detailed System Design of Perpendicular station	123
A.2 Statitscs of mode position of circular devices	129

LIST OF FIGURES

	Page
2.1 A magnet made of alnico, an iron alloy, with its keeper.	3
2.2 Band structure for ferromagnet. Due to energy split, the majority and minority spin bands have different of states at the Fermi level.	6
2.3 Illustration of tunnel magnetoresistance effect. (a)Configuration of two layers are parallel.(b)Configurations of two layers are anti-parallel.	6
2.4 Schematic of electrons transmitting through and getting reflected from ferromagnet metal, with the transverse spin component absorbed during the process.	8
2.5 Direction of torques presented in the system.	9
2.6 Differential resistance with respect to dc current. Arrows indicate magnetic state to be either parallel and anti-parallel.	10
2.7 An example of a simulated spin transfer switching event.(a)Switching trajectory. Dotted lines show initial state of free layer. Solid line shows the switching (b) Normalized resistance value as a function of time	11
2.8 Schematic representation of (a) fieldinduced switching MRAM and (b) STTM-RAM. In the first case, the curling arrows represent the magnetic field direction generated by the electrodes	13
2.9 Schematic illustration of CoFeB-based MTJs with perpendicular anisotropy .	14
3.1 Sketch of our field-modulation set-up.	24
3.2 (a) Typical ST-FMR spectrum taken with conventional amplitude modulation.(b) ST-FMR spectrum taken with field modulation at the same sample.	25
3.3 (a)Magneto-resistance plot of the sample studied. SAFTop layer start to flop around 4.5kG. (b)Blue dot:Typical ST-FMR spectrum with only lowest-frequency mode. Red dash line: Fitted curve to extract resonance frequency and linewidth.	26
3.4 (a) Fitted resonance frequency plotted against external magnetic field (b)Fitted linewidth plotted as a function of resonance frequency.	27
3.5 ST-FMR spectrum measured without a long attenuating cable attached to the sample (left) is significantly distorted by standing waves in the microwave circuit. (right) The same spectrum measured with a long attenuating cable eliminates the standing wave artifacts.	29

3.6	ST-FMR spectra measured as a function of out-of-plane magnetic field. Q labels the quasi-uniform mode of the free layer while F2 and F3 are the higher order spin wave modes of the free layer. S labels the acoustic SAF mode.	30
3.7	Spectral linewidth of the free layer quasi-uniform mode versus frequency of the mode. Line is the best fit to the data outside of the SAF spin flop and SAF resonant coupling regions.	32
3.8	Spectral linewidth of the free layer quasi-uniform mode versus frequency of the mode. Line is the best fit to the data outside of the SAF spin flop and SAF resonant coupling regions.	33
3.9	(a)Blue dot: Simulated amplitude versus driven frequency. Red line: Fitted Lorentizan curve. (b)Spatial profile of mode amplitude(Top) and phase(Bottom) of the mode excited in the continuous wave. The amplitude and phase are both uniform across the device, indicating a quasi-uniform eigenmode.	34
3.10	ST-FMR spectra measured as a function of out-of-plane magnetic field. Q labels the quasi-uniform mode of the free layer while F2 and F3 are the higher order spin wave modes of the free layer. S labels the acoustic SAF mode.	35
3.11	(a).Simulated spectrum with random magnetic anisotropy(in red dot) compared with spectrum with uniform magnetic anisotropy(blue dot) (b) Top: Spatial profile of the mode amplitude excited. Bottom: Spatial profile of the mode phase. (c)Spatial distributions of the magnetic anisotropy when introducing the random distributed magnetic anisotropy in OOMMF.	36
3.12	Summary of simulated linewidth plotted versus resonance frequency with different material parameters. From the plot only random magnetic anisotropy combined with small exchange stiffness leads to a significant linewidth intercept at zero resonance frequency.	37
3.13	(a) ST-FMR spectrum of a 30 nm by 150 nm stadium-shaped STT-MRAM element. Several spin wave eignemode resonances are seen in the spectrum. (b)Fitted spectrum from micromagnetic simluations.	39
3.14	Spatial mapping of modes excited in the micromagnetic simulations.	40
3.15	(a) ST-FMR spectrum of a 30 nm by 150 nm stadium-shaped STT-MRAM element. Several spin wave eignemode resonances are seen in the spectrum. (b)Fitted spectrum from micromagnetic simluations.	41
3.16	ST-FMR spectra of circular STT-MRAM cells with 250 nm diameter (left) and 80 nm diameter (right) measured as a function of the out-of-plane magnetic field applied to the nanopillar.	43
3.17	Three lowest-frequency spin wave eigenmodes of the free layer of a circular STT-MRAM sample with 60 nm diameter. The top image shows the spatial map of the amplitude of the mode while the bottom image shows the spatial map of the spin wave modes phase	44
3.18	(a) Statistics of the mode frequencies at zero field for different modes. (b) Statistics of mode splitting between the (1,0) and (0,1) modes for 80 nm samples.	45
3.19	Statistics of mode splitting for 80 nm sample. (a):Frequency of the Mode 1 versus frequency of the Mode 0. (b):Frequency of the Mode 2 versus frequency of the Mode 0	45

3.20 (a) ST-FMR spectrum of spin wave eignemodes in a circular 60 nm diameter MTJ nanopillar measured at 1 kG out-of-plane field. (b)Simulated ST-FMR spectrum of a 60 nm circular STT-MRAM element. Vertical dashed lines indicate measured mode positions. Micromagnetic simulated mode profiles are shown next to each mode.	46
3.21 ST-FMR spectrum of spin wave eignemodes in a circular 60 nm diameter MTJ nanopillar measured at 1 kG out-of-plane field. Five modes are visible at low frequency. (b)Simulated ST-FMR spectrum of a 5268 nm ² elliptical STT-MRAM element. Vertical dashed lines indicate measured mode positions. Micromagnetic simulated mode profiles are shown next to each mode. (right) Simulated splitting (frequency gap) of (n=0,L=+1) mode plotted versus eccentricity	47
3.22 Three lowest-frequency spin wave eigenmodes of the free layer of a circular STT-MRAM sample with 60 nm diameter. The top image shows the spatial map of the amplitude of the mode while the bottom image shows the spatial map of the spin wave modes phase	48
3.23 ST-FMR spectrum of spin wave eignemodes in a circular 40 nm diameter MTJ nanopillar with known anomalous WER behavior measured as a function of out-of-plane magnetic field. The SAF spin wave mode and the quasi-uniform free layer mode are labeled by dashed lines in the figure.	49
3.24 Set-up for Magnoise measurement	50
3.25 Summary of the magnoise measurement. Top: Raw spectrum taken without the field modulation. Middle: Integration of the spectrum taken with the field modulation. Bottom: Raw spectrum taken with the field modulation technique.	51
3.26 (a) The magnetoresistive curve of the studied sample with the TMR ratio around 180 % and the coercive field close to 2 kG. (b) measured ST-FMR 2D spectrum of this device. Three spin-wave modes are visible.	53
3.27 (a) Direct measurement of the bias-dependent magnoise measurement. (b) Integration of the raw spectrum under dc-bias. Three spin wave modes are visible as labelled.	53
3.28 (a) ST-FMR data on the frequency domain as a function of dc bias voltage (b) Magnoise data on the frequency domain as a function of dc bias voltage .	54
3.29 (a) ST-FMR data on the field domain as a function of dc bias voltage (b) Magnoise data on the field domain as a function of dc bias voltage	54
3.30 2D contour plot of ST-FMR spectrum taken at AP state(left) and P state(right). Both AP and P state has four lowest obvious spin-wave modes but with different mode spacings.	56
3.31 Bias dependent ST-FMR spectrum taken at the constant driven frequency 16 GHz for both AP state(left) and P state(right). All the spin-wave modes have the same curvature versus bias.	58
3.32 2D contour plot of ST-FMR spectrum taken at AP state with out-of-plane field applied(left) and in-plane field(right). Both spectrum has four lowest spin-wave modes with different relative amplitude.	58

3.33 (a) Resistance versus Magnetic Field for different magnetic field angles with respect to the sample normal. (b) Example ST-FMR spectrum at 9 GHz for AP state.	60
3.34 (a) ST-FMR 2D contour plot at AP state with field applied perpendicular to the MTJ. (b) ST-FMR 2D contour plot at AP state with field applied parallel to the MTJ.	61
3.35 (a) Resonance field versus resonance frequency at AP state. (b) HWHM Linewidth versus resonance frequency (lower scale) and magnetic field (upper scale).	62
3.36 (a) Sketches of different angles notations. (b) Example ST-FMR spectrum at 20 GHz for three angles.	62
3.37 (a) Resonance field plotted versus resonance frequency at AP state for different angles. (b) HWHM Linewidth plotted versus resonance frequency at AP state for different angles.	63
3.38 (a) Resistance versus Magnetic Field for P state. (b) ST-FMR 2D contour plot at P state with field applied perpendicular to the MTJ.	64
3.39 (a) Resonance field plotted versus resonance frequency at P state. (b) HWHM Linewidth plotted versus resonance frequency (lower scale) and magnetic field (upper scale).	64
3.40 ST-FMR signal (symmetric and anti-symmetric components) plotted versus resonance frequency	65
3.41 (a) Example ST-FMR spectrum at 20 GHz for three angles at P state. (b) Resonance field plotted versus resonance frequency at P state for different angles.	66
3.42 HWHM Linewidth plotted versus resonance frequency at P state for different angles	66
4.1 Original time-domain setup	68
4.2 Improve time-domain set-up	70
4.3 A switching signal from time-domain measurement. Anti-parallel signal(blue), PtoAP signal(red) along with the voltage difference(Green)	71
4.4 (a) Zoomed PtoAP signal(red) and AP state background(blue) (b)Zoomed voltage signal difference.	72
4.5 Switching events for different individual events.(a)(b)(c) show switching events which switch at 2.6 ns, 6.7 ns and 9 ns respectively. (d) shows the non-switching event.	73
4.6 Distribution of switching time at constant voltage 425 mV.	74
5.1 Write Error Rate measurement set-up, here we include AC and DC circuit . .	76
5.2 Pulse shape used in Write Error Rate Measurement	77
5.3 Resistance versus dc voltage at zero magnetic field	81
5.4 Write Error Rate curve for one typical device studied in the experiment. . .	82

6.1	(a) Example magnetoresistance of one 80 nm MTJ device (b) 2D contour plot of the ST-FMR signal of this device with -2 dBm power applied at the AP state	85
6.2	Top: the frequency versus resonance field for three lowest modes. Bottom: the HWHM linewidth versus resonance field for all the three modes.	86
6.3	Summary of main mode of all the three modes. The error bar indicates the standard deviations obtained from sample statistics.	88
6.4	(a) Main mode frequency is plotted as a function of device diameter. (b) Mode Gap plotted as a function $1/d^2$ with d represents the diameter of the device.	89
6.5	Simulated MTJs structures. The magnetization and thickness parameters are listed for each magnetic layer.	91
6.6	(a) Simulated 70 nm diameter spectrum with mode profiles showing around the peak. (b) Simulated spectrum with different elliptical shapes. (c) The mode profile splitting of the first higher order mode into two modes in the ellipse with nodes along short and long axis.	92
6.7	Top: Simulated mode frequencies for the first two modes excited in the 55 nm diameter circular devices as a function of the exchange constant. Bottom: The mode spacings as a function the exchange constant with linear fitting.	93
6.8	Circular Device Simulation Summary. For each nominal device, we list the simulated diameter(15 nm smaller). The exchange stiffness and the standard variations are listed.	95
6.9	Simulations of the mode spacings as a function of the exchange stiffness for different diameters. The MTJs only has a magnetic free layer.	96
6.10	(a) Example magnetoresistance of one 60 nm * 80 nm stadium-shaped MTJ device. (b) The resistance versus current loop, with AP state switching to P state at negative dc current and vice versa. (c) 2D contour plot of the ST-FMR signal of this device with -2 dBm power applied at the AP state	98
6.11	(a) The resonance field fitting result for all the three modes. (b) The ST-FMR signal (symmetric and anti-symmetric component) plot versus resonance field. (c) The ratio of two components versus resonance magnetic field.	98
6.12	(a) The power-dependent ST-FMR field sweep spectrum at AP state with 12 GHz. (b) The amplitude versus the square of rf voltage.	99
6.13	(a) The resonance Field versus rf voltage squared for all the modes at 12 GHz. (b) The Mode 0 HWHM linewidth versus rf voltage squared.	100
6.14	(a) The bias-dependent ST-FMR field sweep spectrum at AP state with 12 GHz. (b) FMR signal amplitude versus applied dc voltage.	100
6.15	Fitting of the FMR symmetric amplitude versus DC voltage as a sum of linear term and quadric term.	101
6.16	Demo of Perpendicular magnetized MTJs angle oscillation with out-of-plane magnetic field.	102
6.17	(a) The resonance field versus bias for three modes. (b) Mode 0 HWHM linewidth versus applied dc bias.	103
6.18	(a) Magneto-resistance curve for 210 nm * 60 nm devices (b) ST-FMR field sweep 2D spectrum at AP state with example scan at 12 GHz.	104

6.19 Main mode frequency with standard deviations versus device length for 60 width devices. The plotted device length is 15 nm smaller than nominal size	105
6.20 Mode gap with standard deviations versus device length for nominal 60 nm width devices. The mode gap is decreasing as increasing length.	105
6.21 Example of simulation spectrum for $45*65\text{ nm}^2$ device.	106
6.22 (a) Experimental mode frequencies compared with simulation values in different exchange stiffness (unit in pJ/m). (b) Experimental mode spacing compared with simulation values in different exchange stiffness (unit in pJ/m).	107
6.23 Mode Gap plotted versus simulated exchange stiffness for $45*65\text{ nm}^2$ device.	108
6.24 Mode Gap plotted versus simulated exchange stiffness for $45*65\text{ nm}^2$ device.	108
6.25 (a) Examples of 2D ST-FMR contour plot for nominal $45*60\text{ nm}^2$ device. (b) Examples of 2D ST-FMR contour plot for nominal $45*70\text{ nm}^2$ device.	110
6.26 (a) Average main (0) mode frequency (with standard deviations) plotted versus actual device length (b) Mode Gap 1-0 shows a 1/length fit	111
6.27 (a) AP state main mode frequency plotted versus AP state Resistance. (b) Mode Gap frequency plotted versus AP state Resistance	112
6.28 mode gap plotted versus simulated exchange stiffness for different geometries with same 30 nm width	112
6.29 Summary of exchange stiffness fitting: size dependence of width 45 nm . . .	113

LIST OF TABLES

	Page
3.1 Summary of continuous micromagnetic simulations result.	38
3.2 Comparisons between four lowest spin-wave modes at AP state at zero magnetic field with different magnetic field direction(easy-axis out-of-plane and hard-axis in-plane) applied.	59
6.1 The simulated mode frequencies with different geometries and comparisons with the experimental data. All the numbers are in GHz unit.	93
6.2 Circular Device Simulation Summary. For different sizes, Both the frequencies of the two modes and the mode spacing are plotted against the exchange constant	94
6.3 Summary of fitted exchange stiffness for different diameters.	96

ACKNOWLEDGMENTS

I would like to express my deepest appreciation to Professor Ilya Krivorotov. It is quite a privilege to work with him. I really learned a lot from his great knowledge of physics and sharp insights into problem solving. I still remember almost six years ago I had my first Skype interview with Ilya and he asked me about exchange bias effect. Without his guidance and help this dissertation would not be possible.

I would also like to thank all my lab mates : Zheng Duan, Igor Barsukov, Eric Montoya, Brian Youngblood, Yu-Jin Chen, Andrew Smith, Han Kyu Lee, Jenru Chen, Jieyi Zhang, Alejandro Jara, Chris Safranski and Josh Dill. I have been received a great amount of help since the first day I joined the lab. When I first joined the lab, I did not know even most simple thing, such as using a torque wrench and basis soldering. These guys helped me overcome a lot of difficulties and provided help whenever I asked. I never wished I could be surrounded by such a amazing group of people and I really feel honored to call these guys my lab mate.

During the last five years in the United States, I am happy to keep in touch with my good friends over the world. I would like to thank Jiao Li, Rui Da, Ruohui Yang, Xun Liu, Hongyu Zhu and Qingyu Zhu. Those people are all pursuing or have already obtained their Ph.D. degree and we have had lots of useful/useless discussions about our common experiences. We shared numerous joy and distress over the past five years and each one of them spent their time to listen to me venting my life(maybe too much). I might not be able to see these friends quite often and in fact, I have not met some of them for almost five years. However, their support is greatly valuable to me and I really hope nothing but the best for all of them from my heart.

Of course I am extremely luck to have a loving family.

ABSTRACT OF THE DISSERTATION

Spin torque driven magnetization dynamics in nanoscale magnetic tunnel junctions

By

Chengcen Sha

Doctor of Philosophy in Physics

University of California, Irvine, 2018

Professor Ilya Krivorotov, Chair

The abstract of your contribution goes here.

Chapter 1

Introduction

Spin transfer torque is generated by the transfer of angular momentum from spin polarized electrons to a ferromagnet. This spin transfer torque provides an efficient way to manipulate the dynamic motion of the magnetization of a nanomagnet, and can be strong enough to induce magnetization switching and steady-state precession. This field of study draws enormous attention not only because spin transfer torque is essential in understanding fundamental physical phenomena, but also it makes the building block for future applications such as spin torque oscillators, magnetic random access memory. We have developed several new techniques to characterize such dynamics in nanoscale magnetic tunnel junctions.

In chapter 2, we will first discuss necessary background knowledge in this field. In chapter 3, we develop a new reliable methods to characterize material parameters such as magnetic anisotropy and Gilbert damping using spin-torque ferromagnetic magnetic resonance with field-modulation. By performing micromagnetic simulations, we can determine other spatial-dependent parameters.

In chapter 4, we demonstrate a single-shot electrical technique to capture the magnetic dynamics during the spin torque switching of a magnetic tunnel junction in real time. With improved sensitivity, we can directly observe real-time oscillation before switching.

In chapter 5, we focus on measurement of switching probability of magnetic tunnel junctions by applying electric pulses. We observe anomalous write error rate behavior in our magnetic tunnel junctions samples. Possible origins of this anomalous write error rate has been discussed.

Chapter 2

Background

2.1 Spintronics

Nearly five thousand years ago, people already discovered the natural magnets and they found out that when you move two magnets closer to each other, they can either be attractive or repulsive depending on the relative directions. Without understanding the mechanism, people already made some useful stuff such as a horseshoe magnet[1].



Figure 2.1: A magnet made of alnico, an iron alloy, with its keeper.

However, it was not until 1925 that the underlying mystery of ferromagnetism started to reveal itself. George Uhlenbeck and Samuel Goudsmit proposed the idea that each electron spins

with an angular momentum of one half Planck constant and carries a magnetic moment of one Bohr magneton. Even though the famous Hendrik Lorentz pointed out that the idea of a spinning electron would be incompatible with classical electrodynamics, those two physicists went ahead and published their results. Of course, they were right and Lorentz was wrong. Uhlenbeck and Goudsmit maybe could not image their findings to have such a great impact on modern information technology. While electronics, the manipulations of electron charges in various kinds of devices, has been developed greatly since 1950s and shaped a new world, the development of spintronics started to influence the modern technology since 1980s. Johnson and Silsbee[2] observed spin-polarized electron injection from a ferromagnetic metal to a normal metal. Albert Fert[3] and Peter Grünberg[4] independently discovered the phenomena of Giant magnetoresistance(GMR) and they have been rewarded The Nobel Prize in Physics 2007 for the practise significance of this work. Spintronics have several major advantages over conventional electronics. Unlike the conventional electronics which relies on the transportation of electrons charges, which inevitably creates heating dissipation and power loss, spintronics can perform with pure spin currents and movements of spin angular momentum without heat. Moreover, once formed, the spins does not need energy to maintain it. The non-volatility takes a huge advantages in static power consumption. Spintronics has a great ongoing and potential applications in memory storage, signal processing and logical devices.

2.2 Tunnel Magnetoresistance

The Tunnel Magnetoresistance effect[5] refers to the change of resistance of a ferromagnetic/non-magnetic barrier/ferromagnetic metallic multilayer structure as the relative orientation of the magnetizations of two ferromagnetic layers changes. When the two layers have parallel magnetizations, the resistance is lowest and the resistance is maximum when magnetizations of

two ferromagnetic layers are anti-parallel. Nowadays, the resistance difference between the maximum and minimum values can be as much as 100 per cent.

We first consider a simple case when electrons are passing through a single ferromagnetic layer. For a 3d transitional ferromagnetic layer like Ni, Co and Fe, ferromagnetism is coming from the exchange coupling of 3d electrons. In a simplified band structure for ferromagnetic metals, the exchange coupling results in an split of energy band for 3d electrons. As a result when the spin-up band and spin-down band are filled up to the Fermi level, there will be more spin-up electrons than spin-down electrons, which induces a net magnetization. On the other hand, the majority and minority spin bands also have different density of states at the Fermi level. The conduction properties of a metal are primarily determined by the electrons near the Fermi level. When spin unpolarized electrons consisting of equal numbers of spin-up and spin-down electrons travel in a ferromagnet, different spins experiences different resistances. Besides, different types of spins also experience different scattering at the interface due to the band structure mismatch. Overall, one type of spins has higher probability to transmit through than the other type.

Now, we have two magnetic layers separated by a tunnel barrier. As it has been proposed by Julliere in 1975, the tunneling probability across the tunnel barrier,which can be treated as conductance in this case, is proportional to the density of states of both initial and final states. Then we have

$$\begin{aligned} G_p &\propto \rho_{L\uparrow}\rho_{R\uparrow} + \rho_{L\downarrow}\rho_{R\downarrow} \\ G_{Ap} &\propto \rho_{L\uparrow}\rho_{R\downarrow} + \rho_{L\downarrow}\rho_{R\uparrow} \end{aligned} \tag{2.1}$$

where $G_P(G_{AP})$ is the parallel(anti-parallel) conductance, $\rho_{L\uparrow}$ and $\rho_{L\downarrow}$ ($\rho_{R\uparrow}$ and $\rho_{R\downarrow}$) are densities of states for up and down spins of the left(right) ferromagnet. By definition, the spin

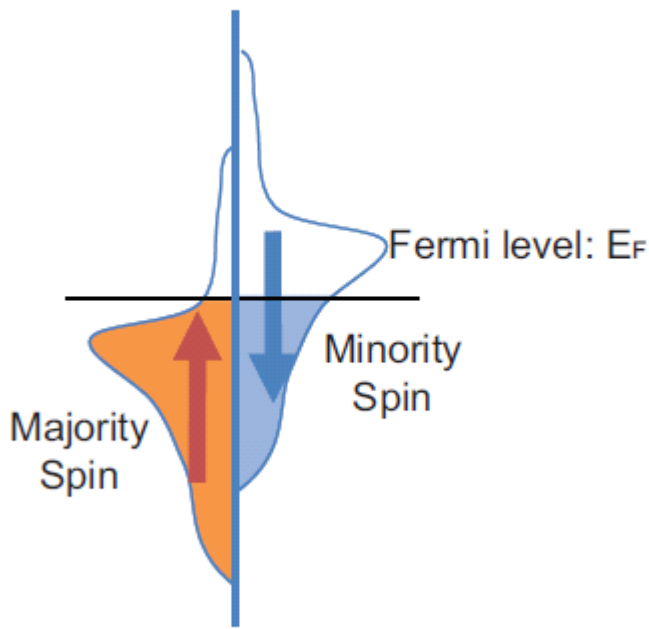


Figure 2.2: Band structure for ferromagnet. Due to energy split, the majority and minority spin bands have different of states at the Fermi level.

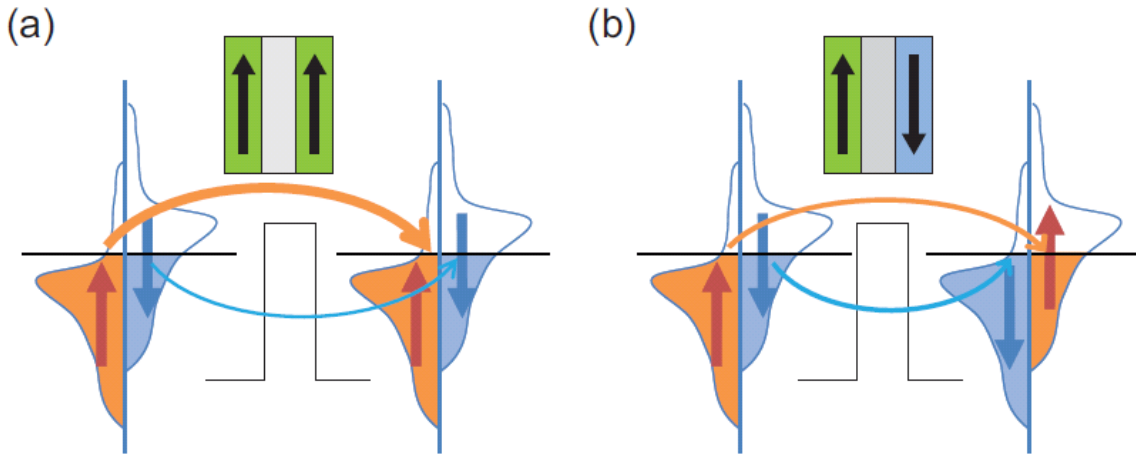


Figure 2.3: Illustration of tunnel magnetoresistance effect. (a) Configuration of two layers are parallel.(b) Configurations of two layers are anti-parallel.

polarization P is

$$P = \frac{\rho_{\uparrow} - \rho_{\downarrow}}{\rho_{\uparrow} + \rho_{\downarrow}} \quad (2.2)$$

Therefore the tunnel magnetoresistance ratio can be calculated as

$$TMR = \frac{R_{AP} - R_P}{R_P} = \frac{G_P - G_{AP}}{G_{AP}} = \frac{2P_L P_R}{1 - P_L P_R} \quad (2.3)$$

In early studies of MTJs,a TMR ratio of a few 10's of percent was achieved with amorphous aluminum oxide(AlO)barries. Most recently, single crystalline magnesium oxide(MgO) barries were predicted to provide a much higher TMR ratio due to the wavefunction match between the ferromagnetic electrodes and the tunnel barrier. TMR ratios of around 200 percent were then demonstrated and led to intensive studies in MgO bases MTJs mainly because of the high TMR ratio founded in this family[6].

2.3 Spin transfer torque

Spin transfer torque refers to the torque between electrons and local magnetization. As it is shown in 2.4, the direction of incident electron is randomly distributed in all directions. When electrons are entering a ferromagnetic layer, due to the fixed magnetization of this FM layer, electrons are parallel to the local magnetization will have high probability of transmission and on the other hand, the electrons having opposite direction will mostly be reflected. As a result, transmitted electrons will be aligned to the local magnetization and reflected. In this process, the angular momentum of incident electrons has been changed by local magnetization. On the other hand, the local magnetization also experience torque from incident electrons as well. This torque is called the spin transfer torque[7] [8] and can provide an efficient way to manipulate local magnetization as we shall see next.

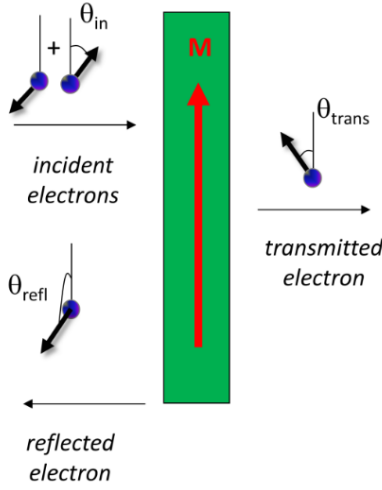


Figure 2.4: Schematic of electrons transmitting through and getting reflected from ferromagnet metal, with the transverse spin component absorbed during the process.

Magnetic tunnel junction is the main device we have been studied. The device has a structure of two ferromagnetic layers separated by a spacer. The multilayers are patterned into an elliptically-shaped nanopillar with the size normally around 60nm. The top and bottom of the devices are connected to electrical leads to allow current to pass perpendicularly through the multilayers.

The dynamics of the magnetization in the presence of spin transfer torque can be described by the classical Landau-Lifshitz-Gilbert(LLG) equation including an additional term for the spin torque:

$$\frac{dM}{dt} = \gamma M \times H_{eff} + \alpha M \times \frac{dM}{dt} + g(\theta) \frac{\gamma \hbar I}{eV_{free}M_s} M \times (M \times M_{fix}) \quad (2.4)$$

where H_{eff} is the total effective field including the applied field $H_{applied}$ and the anisotropy field H_{ani} and α is the damping constant. The first term is the field torque term which makes the magnetization precess around the effective field direction. The second term is

the damping torque which relates the energy dissipation. On average it points towards the equilibrium position of the magnetization, so that without any external excitation the magnetization will relax back to the equilibrium. The third term is the spin transfer torque. The direction of this torque depends on the direction of the electron flow. For electron flow from the fixed layer to the free layer, this torque is in the same direction as the damping torque assuming the fixed layer also along the effective field direction, in this case spin transfer torque works as additional damping torque. On the other hand, for electron flow from the free layer to the fixed layer, this torque works against the damping torque and thus can reduce the relaxation.

The first case we discussed is of less interest. For the second case we have the competition between spin transfer torque and damping torque[9]. Usually the spin transfer torque is small compared to the field torque. So the effect of spin transfer torque can be viewed as either increasing or decreasing the amplitude of the magnetic precession. In general, the magnetic dynamics excited by spin transfer torque can be categorized in to two types: switching and persistent precession.

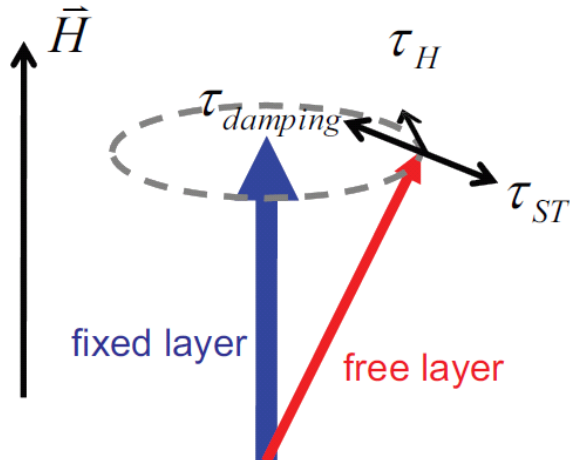


Figure 2.5: Direction of torques presented in the system.

2.4 Magnetic Switching

At zero or small field, both direction along the easy axis correspond to local energy minimums so it is possible to switch the magnetization between these two directions with spin transfer torque. For example, for a device with both free and fixed layers keeping at the easy axis direction and parallel to each other, if we flow a positive current defined as current flow from free to fixed layer, according to previous analysis, the spin transfer torque acts on the free layer is pointing away from the fixed layer and destabilizes this configuration so that the magnetic moment of the free layer goes into a precession around the easy axis. If we keep increasing the current, the amplitude of the free layer precession increases until it reaches the energy barrier which is around 90 degree. After the free layer changes direction, now the spin transfer torque will act as damping torque again and stabilize the magnetization. Similarly, if the magnetic tunnel junction starts in the anti-parallel configuration, a strong enough negative current can switch the free layer back to the parallel configuration. If we monitor the resistance of the device, it will exhibit a hysteresis loop as we sweep the current, as shown in the example

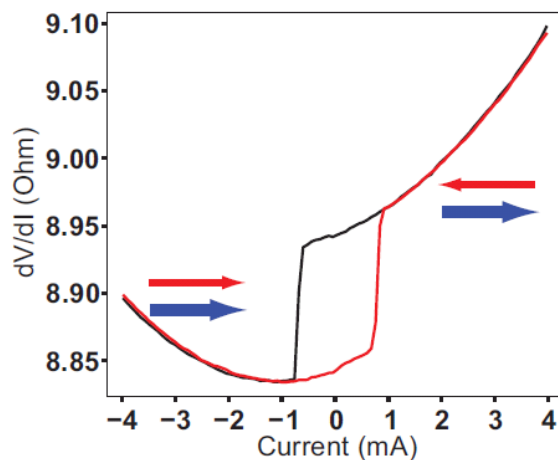


Figure 2.6: Differential resistance with respect to dc current. Arrows indicate magnetic state to be either parallel and anti-parallel.

The critical switching current I_c is defined as the current required to achieve switching at zero temperature(no thermal excitations) . Above I_c , the spin torque is stronger than the damping torque and drives the free layer moment to switch direction.

Fig.2.7 illustrate the switching process. The switching proceeds via a precessional motion of the magnetization with increasing amplitude[10]. The switching time is defined as the following :

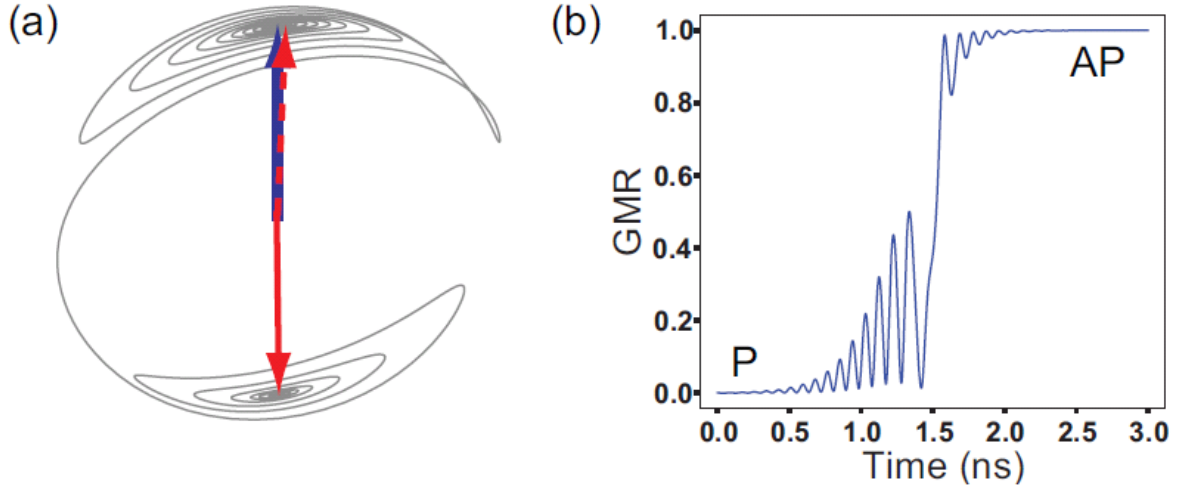


Figure 2.7: An example of a simulated spin transfer switching event.(a)Switching trajectory. Dotted lines show initial state of free layer. Solid line shows the switching (b) Normalized resistance value as a function of time

$$t_s \propto \frac{1}{I - I_c} \quad (2.5)$$

Now if the applied current is smaller than the critical current, the spin torque is not strong enough to drive the free layer moment to directly overcome the energy barrier to achieve switching but only to excite magnetic precession at small amplitudes. At finite temperatures, switching can still occur due to thermal excitations. This thermal-assisted magnetization

reversal can be described by the Neel-Brown relaxation time:

$$P(t) = 1 - \exp(-t/\tau) \quad (2.6)$$

where t is the observation time, and τ is the relaxation time which is given by

$$\tau = \frac{1}{f_0} \exp E_b/k_B T \quad (2.7)$$

Here f_0 is the attempt frequency, E_b is the energy barrier and T is the temperature. Thermal assisted switching can be modeled by a fluctuating field with a Gaussian stochastic process. The relaxation time τ can be modified as the following:

$$\tau = \frac{1}{f_0} \exp \left[\frac{E_b}{k_B T} \left(1 - \frac{I}{I_c} \right) \right] \quad (2.8)$$

2.5 Magnetic Tunnel Junctions

In this chapter we will discuss Magnetic Tunnel Junctions(MTJs), which is the fundamental building block for future Magnetic Random Access Memory(MRAM)[11]. MRAM has been widely studied over the past few decades due to its non-volatility and unlimited read and write endurance[12]. In order to compete with current existing and other promising semiconductor memories, it is expected that the MRAM should have low read and write power consumptions along with higher thermal stability and also good scaling to fit into modern CMOS design.

The conventional field-induced MRAM, the free layer is switched by applying a magnetic field[13]. The write operation is achieved by carrying the current flowing through the wires,

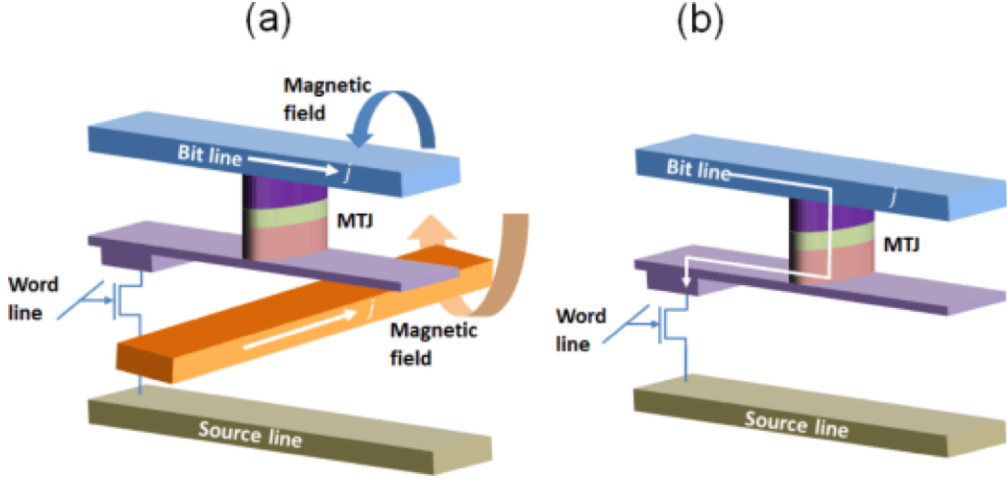


Figure 2.8: Schematic representation of (a) field-induced switching MRAM and (b) STT-MRAM. In the first case, the curling arrows represent the magnetic field direction generated by the electrodes

which then generated a magnetic field around the wires as shown in Fig.2.8(a). The major problem is the current required for field induced switching increases as the size of the devices decrease. As a result, the field-induced MRAM has a scaling limit about 90 nm.

The Spin-transfer-torque MRAM(STT-MRAM), which is based on the spin transfer torque produced by spin polarized current, is the current solution for reducing the switching current and scaling problems. The applied current first get polarized at a thicker and more robust ferromagnetic layer(fixed layer) and then enter the free layer. Depending on the relative direction between the fixed and free layer, the current can be either damping and anti-damping. If the current is large enough, the free layer can then be switched as shown in Fig.2.8(b). It has been demonstrated that the spin-torque induced switching can be seen in both aluminum oxide and magnesium oxide based MTJs[14][15] and other work has been done to incorporate MTJs into CMOS chips[16] [17][18].

The first generation of MTJs consist of in-plane magnetized free layer. One of the major disadvantage of in-plane MTJs is that when the nano pillars are patterned, vortex magnetization is formed at the edges[19][20]. To overcome this problem, the aspect ratio of the ideal devices must be larger than 2[21], which limits the density of MRAM chips. In addition, the

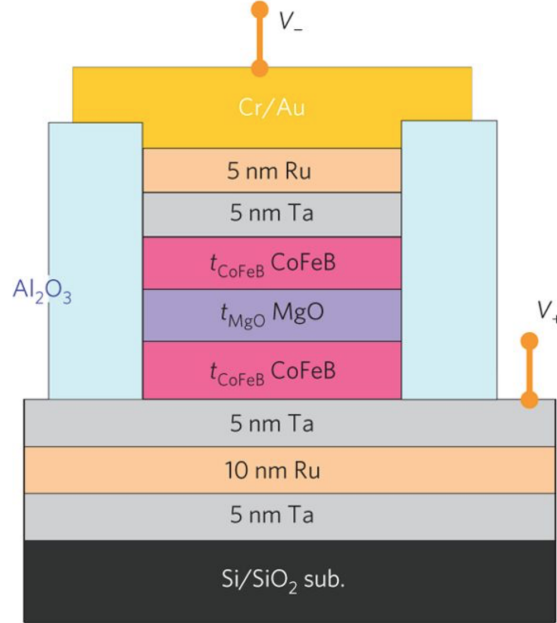


Figure 2.9: Schematic illustration of CoFeB-based MTJs with perpendicular anisotropy

magnetoresistance MR curve of the in-plane MTJ is generally not centered due to interlayer couplings[22], which reduces the tolerance of writing current.

Magnetic Tunnel Junctions with perpendicular easy axis, compared with in-plane MTJs, are of great interests due to higher thermally stability and low critical switching current[23][24][25]. Besides, the material combination of CoFeBMgO has been shown to have giant tunnel magnetoresistance even at room temperature[26][27][28]. In 2010, it has been demonstrated that perpendicular MTJs consisting of Ta/CoFeB/MgO/CoFeB/Ta show a high tunnel magnetoresistance ratio, high thermal stability and low switching current[29], which has become a mainstream of MTJ stack structures since then as shown in the Fig.2.9.

When integrating MRAM with modern circuits, the static power consumption can be greatly reduced because of the non volatility of the MTJs. However, the dynamic power consumption is still large compared with other competitors, part of the reason is that the spin-transfer-torque(STT) switch is not fast[30]. To improve the write efficiency, fast switching schemes has been developed to reduce the switching time[31][32]. On the other hand, other writing

methods(switching mechanism) has also been developed. One example is to use electric-field controlled magnetism, where applying voltage pulse to modify the magnetic anisotropy of the free layer[33]. One methods is to use electric field to reduce the magnetic anisotropy to assist STT switching[34]. It is also possible to use voltage-controlled-magnetic anisotropy(VCMA) alone to switch the MTJs[35][36][37].Besides from reducing the switching current, a higher thermal stability of the MTJs is also preferred for memory capacity with sufficient retention time. To solve this problem, double MTJs have been proposed with two SAF layers and two CoFeB-MgO interfaces[38][39][40]. Compared with single MTJs, the double MTJs now have spin-transfer torque from both direction of the free layer with the same amount of current flow and it proves up to 2 times improvement in switching efficiency[41].

Recently, Spin-orbit torque(SOT) has become an alternative way to switch the free layer of the MTJs. In this configuration, the MTJs are patterned on a nonmagnetic heavy metal layer. By applying a current in the heavy metal layer, a spin-polarized current, arising from the spin-orbit coupling, is injected into the MTJs to manipulate the magnetizations[42][43]. Based on this concept, three-terminal MTJs has been developed where the write and read operations are decoupled into different current paths. So that the read disturbance of the MTJSs can be minimized to improve the endurance. Three terminal MTJ devices have been demonstrated in both in-plane[44][45][46] and out-of-plane[47] free layers.

2.5.1 Critical Switching Voltage

In this section we would like to derive the critical switching voltage of the Magnetic Tunnel Junction(MTJ). We would like to prove that the critical voltage is symmetric between the Anti-Parallel state and the Parallel state, which is an important reason why it is crucial to characterize the MTJ in terms of bias voltage, not the bias current as used in many other magnetic materials system.

The critical switching current is given by[48]

$$I_{c0} = 2\alpha \frac{\gamma e}{\mu_B \eta} E \quad (2.9)$$

Here α is the Gilbert damping constant , γ is gyromagnetic ratio, e is the elementary charge η is the spin-transfer efficiency. The energy barrier E is given by

$$E = M_s H_K V / 2 \quad (2.10)$$

Here M_s is the saturation magnetization, H_K the anisotropy field, V is the volume. We can further rewrite the spin transfer efficiency as

$$\eta = \frac{P}{2} \frac{1}{1 + P^2 \cos \theta} \quad (2.11)$$

P is the polarization factor given by

$$P = \sqrt{\frac{G_P - G_{AP}}{G_P + G_{AP}}} \quad (2.12)$$

The conductance of the Magnetic Tunnel Junction can be given by[49]

$$G(\theta) = \frac{1}{2}(G_P + G_{AP}) + \frac{1}{2}(G_P - G_{AP}) \cos \theta = \frac{G_P + G_{AP}}{2} [1 + P^2 \cos \theta] \quad (2.13)$$

If we define $G_0 = \frac{G_P + G_{AP}}{2}$ as the average conductance and use the Ohm's Law, the critical switching voltage for MTJ should be

$$V_{C0} = \frac{I_{C0}}{G(\theta)} = 2\alpha \frac{\gamma e}{\mu_B} E \frac{1}{\eta G(\theta)} \quad (2.14)$$

Replacing gyromagnetic ratio with g factor $\gamma = \frac{g\mu_B}{\hbar}$, the above equation becomes

$$V_{C0} = 4\alpha \frac{ge}{\hbar P G_0} E \quad (2.15)$$

One can easily find from Eq.2.15, it is clear that the critical switching voltage of MTJs does depend on the relative configurations of two ferromagnetic layers of the MTJ. Parral and Anti-Parallel states have the same critical voltage(in this macrospin model).

2.6 Ferromagnetic Resonance

We start with the coordinate system that the place $y = 0$ is subjected to a d.c. field H_z and a weak microwave field H_x . The magnetization \mathbf{M} and the angular momentum density \mathbf{J} are related by $\mathbf{M} = \gamma \mathbf{J}$ [50][51], where γ is the gyromagnetic ratio. The equation of motion $\frac{\partial \mathbf{J}}{\partial t} = [\mathbf{M} \times \mathbf{H}]$ can be written as

$$\frac{\partial \mathbf{M}}{\partial t} = \gamma [\mathbf{M} \times \mathbf{H}] \quad (2.16)$$

If we want to solve for the general resonance condition for a ellipsoid with major axis parallel to the x, y, z axes of the coordinate system, we first have the demagnetization factor: N_x, N_y

and N_z . The effective values of the magnetic field components are

$$\begin{aligned} H_x^i &= H_x - N_x M_x \\ H_y^i &= -N_y M_y \\ H_z^i &= H_z - N_z M_z \end{aligned} \quad (2.17)$$

The values H_x^i , H_y^i and H_z^i should be used when substituting H in Eq.2.16. Now we can decompose Eq.2.16 into

$$\begin{aligned} \partial M_x / \partial t &= \gamma [H_z + (N_y - N_z)M_z]M_y \\ \partial M_y / \partial t &= \gamma [M_z H_x - (N_x - N_z)M_x M_z - M_x H_z] \\ \partial M_z / \partial t &\approx 0 \end{aligned} \quad (2.18)$$

If we solve these equations with time dependent $\exp i\omega t$, the susceptibility $\chi_x = M_x/H_x$ is given by

$$\chi_x = \frac{\chi_0}{1 - (\omega/\omega_0)^2} \quad (2.19)$$

where

$$\chi_0 = \frac{M_z}{H_z + (N_x - N_z)M_z} \quad (2.20)$$

and the resonance frequency is given by

$$\omega_0 = \gamma \{ [H_z + (N_y - N_z)M_z] \times [H_z + (N_x - N_z)M_z] \}^{\frac{1}{2}} \quad (2.21)$$

From Eq.2.21 we can have some special cases:

1. Plane ($N_x = N_z = 0; N_y = 4\pi$)

$$\omega_0 = \gamma(B_z H_z)^{\frac{1}{2}} \quad (2.22)$$

2. Sphere ($N_x = N_y = N_z = 4\pi/3$)

$$\omega_0 = \gamma H_z \quad (2.23)$$

3. Infinite Circular Cylinder ($N_x = N_y = 2\pi; N_z = 0$)

$$\omega_0 = \gamma(H_z + 2\pi M z) \quad (2.24)$$

It is often that the ferromagnetic crystals energies depends on the relative magnetization orientations and in order to minimize the total energy, the magnetizations would align with the easy axis. This is called the anisotropy energy. If the anisotropy is uniaxial, the first-order magnetic anisotropy can be written as

$$f = K_1 \sin \theta^2 \quad (2.25)$$

where f refers to unit volume of material. θ is the angle between the magnetizations and the easy axis of the crystal. K_1 is the first-order anisotropy constant. To account for the effect on resonance conditions, it is easier to consider the effect in terms of an equivalent magnetic field. The equivalent field H^e is defined as

$$\partial f / \partial \theta = M_s \times H^e \quad (2.26)$$

It should be noted that the direction of effective field H^e is still arbitrary and without lose any generality, we can express the effective field in terms of effective demagnetizing factor N^e as

$$\begin{aligned} H_x^e &= -N_x^e M_x \\ H_y^e &= -N_y^e M_y \end{aligned} \tag{2.27}$$

The resonance condition from Eq.2.21 can now be modified as

$$\omega_0 = \gamma \left\{ [Hz + (N_y + N_y^e - N_z)M_z] \times [Hz + (N_x + N_x^e - N_z)M_z] \right\}^{\frac{1}{2}} \tag{2.28}$$

2.7 Spin-torque Ferromagnetic Resonance

As we mentioned above, when the spin transfer torque is small, the magnetization will not reverse however experience a persistent precession. By applying AC current, excited magnetic precession can be detected by measuring a mixing DC voltage from the product of the resistance oscillation and the ac current. This Spin-transfer Ferromagnetic Resonance (ST-FMR) [52][53] is similar to the traditional ferromagnetic resonance, but can be performed in much smaller devices. The ST-FMR technique can be used to characterize important material properties such as voltage-controlled-anisotropy[35][54][55], magnetic damping[56], field-like torque[57] along with the spectrum of magnetic excitations of the MTJ[58][59], which is not important for understanding basis physic phenomena like spin-tunnel process but also essential for characterizing and optimizing the MTJs for future applications. In Chapter 3, I will describe an improved technique to measure Spin-torque Ferromagnetic Resonance with field modulations.

Chapter 3

Field-Modulated Spin-torque Ferromagnetic Resonance

3.1 Spin-torque Ferromagnetic Resonance

Ferromagnetic resonance (FMR) is the main technique to study dynamical properties of magnetic materials. However, conventional FMR detection methods lack the sensitivity to measure individual sub-100-nm-scale devices that are of interest for fundamental physics studies and for a broad range of memory and signal-processing applications[52].

Sankey and Tulapurkar et al. demonstrated that they can excite precession not by applying an ac magnetic field as is done in other forms of FMR, but by using the ac spin-transfer torque from a spin-polarized ac current. When an alternating current is applied to the sample[52][53], spin transfer torque induces magnetization dynamics, leading to a changing sample resistance from the sample magnetoresistance. Alternating current and resistance get mixed and give rise to a direct voltage, which can be measured using lock-in technique. By sweeping the frequency of the applied alternating current, a peak in the direct voltage generated by the

sample can be observed when the applied frequency matches the resonance frequency of the sample. This technique is called spin-torque ferromagnetic resonance[52] and has been widely used to understand magnetization dynamics induced by spin transfer torque. Analysis of the resonance frequencies, amplitudes, linewidths, and line shapes as a function of microwave power, dc current, and magnetic field provide detailed new information about the exchange, damping[60][61], and spin transfer torques that govern the dynamics in magnetic nanostructures[52].

When the spin polarized current is applied near the resonance frequency, it can drive the precession of magnetization by effectively pushing and pulling the magnetization (depending on the instantaneous polarity of the RF current) in phase with its natural precession. In the case of MTJs, the fixed layer acts as a spin filter which polarizes the current passing through the free layer in the direction of the fixed layers magnetization. In this discussion, it is assumed that the fixed layer magnetization is ideal and completely locked in place. This oscillation of the free layer magnetization will also produce an oscillation of the device resistance due to the varying relative angle between fixed and free layer magnetizations. The time-dependent resistance can be expressed as the expansion [52]:

$$R(t) = R_0 + \Delta R(t) = R_0 + \text{Re}(\sum_n \Delta R_{nf} e^{in\pi ft}) \quad (3.1)$$

When the ΔR_{nf} can be complex. Since the fixed layer is supposed to be stationary, the resistance thus oscillates as the magnetization of the free layer m , which is the solution of the LLGS equation. The mixing voltage signal being measured can be composed of rather complex form, however, it is possible to write the voltage as

$$V_{mix} = V_s S(\omega) + V_a A(\omega) \quad (3.2)$$

Where ω is the driven frequency and V_s and V_a are functions of the spin-torque vector and other magnetic parameters. In this case, the fitting can be simplified as only four fitting parameters. In order to study magnetic information such as anisotropy field and Gilbert damping parameter, one can measure the spectrum and fit from resonance frequency and linewidth as a function of applied field. The theoretical model used here is given by the Kittel equation[51].

$$f_{res} = \gamma(H_k \pm |H_{dip}| + H_{ext}) \quad (3.3)$$

Here f_{res} is the resonance frequency extracted from fitting the curve. H_{dip} is the center of hysteresis loop and H_{ext} is the external magnetic field. The Gilbert damping parameter, given the easy axis approximation, is

$$\alpha = \frac{\Delta f_{res}}{f_{res}} \quad (3.4)$$

It should be noticed that in this Equation 3.4, the linewidth Δf_{res} is the half-width-at-half-maximum(HWHM).

3.2 Experimental Technique

However, this frequency-domain ST-FMR method suffers from frequency-dependent non-magnetic background signals due to non-linearities and impedance mismatches within the microwave circuit. For example, measurements of MTJ with collinear free and pinned layer magnetizations (the STT-MRAM geometry) are challenging with this conventional ST-FMR technique because magnetic signals are typically weaker than the frequency-dependent non-magnetic background signal. Indeed, in the ideal case, device structures with a single perpendicular uniaxial anisotropy axis and preserved rotational symmetry around the axis should

create no spin transfer torque and thus would not resonate at FMR frequencies[62]. On the other hand, measuring ST-FMR at collinear geometry is important. When the magnetizations of free layers are not parallel to, but instead lags behind the external field direction, the linewidth from FMR spectra would be broadened by this magnetic dragging effect[63]. Applying external magnetic field in the easy-axis direction would be convenient for quantitative spin wave mode analysis. For example, measurements of MTJ with collinear free and pinned layer magnetizations (the STT-MRAM geometry) are challenging with the rectification ST-FMR because magnetic signals are typically weak. Fig.3.2(a) shows a typical spectrum measured by conventional ST-FMR with amplitude modulations. Despite the excitations of several spin wave modes, the spectrum has changing background and lots of standing wave from the circuit, thus it would be very hard to quantitatively fit to extract resonance frequency and linewidth.

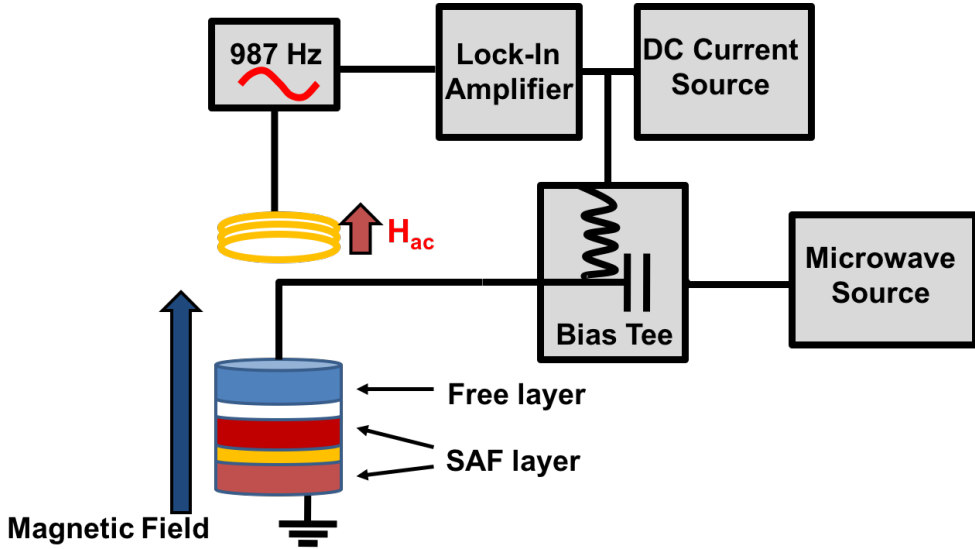


Figure 3.1: Sketch of our field-modulation set-up.

To solve this problem, We make ST-FMR measurement with field modulation technique[64]. A modulation coil is placed just above the sample as shown in Fig.3.1. We then apply kHz-range sinusoidal current of a few Amperes in the coil and generate a few Oersteds alternating magnetic field. The modulation field from the coil is perpendicular to the nanopillar. A

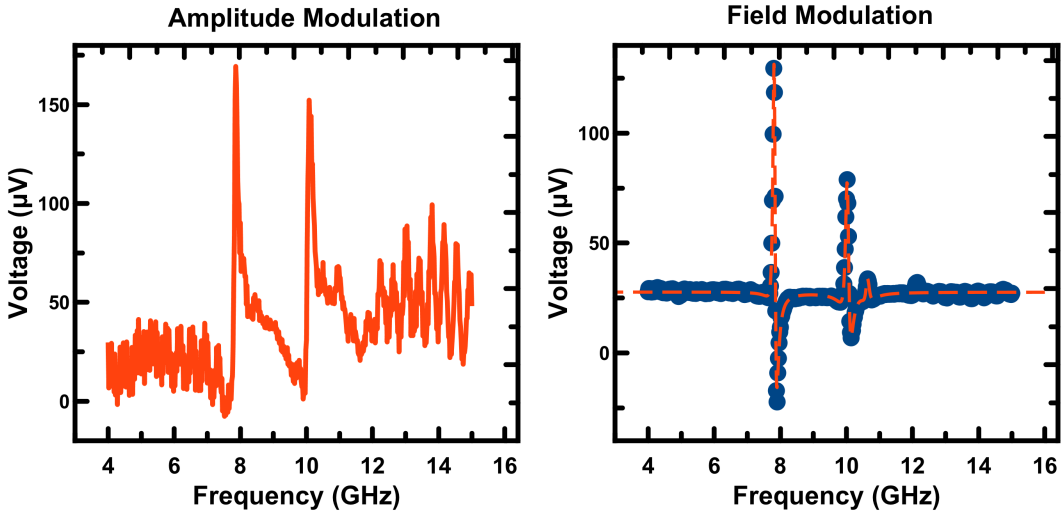


Figure 3.2: (a) Typical ST-FMR spectrum taken with conventional amplitude modulation.(b) ST-FMR spectrum taken with field modulation at the same sample.

continuous microwave current is applied to the sample via a bias tee, and a rectified voltage generated by the sample is measured by a lock-in amplifier at the field modulation frequency. In this case, by sweeping the driving frequency, any non-magnetic background noise would be eliminated. Fig.3.2(b) shows a typical field-modulation spectrum taken at the same sample comparing with Fig.3.2(a)(a). Now we have a much better flat baseline and the standing wave is greatly reduced from the signal.

The MTJ nanopillar we have measured has a lateral size of 65*30nm with a stadium shape: approximately half-circular on both ends of a rectangular. The main functional layers structure of our sample are SAFBottom(1.67)/SAF spacer(0.41)/SAFTop(1.1)MgO(0.8)FreeLayer(2.4) multilayer(thickness in nm). Fig.3.3(a) shows the magneto-resistance plot with magnetic field applied perpendicular to the sample. Around 4.5kG, the resistance of the MTJ start to decrease and eventually switch back to low-resistance parallel state. This is due to the flopping of SAFTop layer[65]. We identify 4.5kG to be the breakdown field and will use it for later discussion.Fig.3.3(b) shows the ST-FMR spectrum focusing on the lowest-frequency

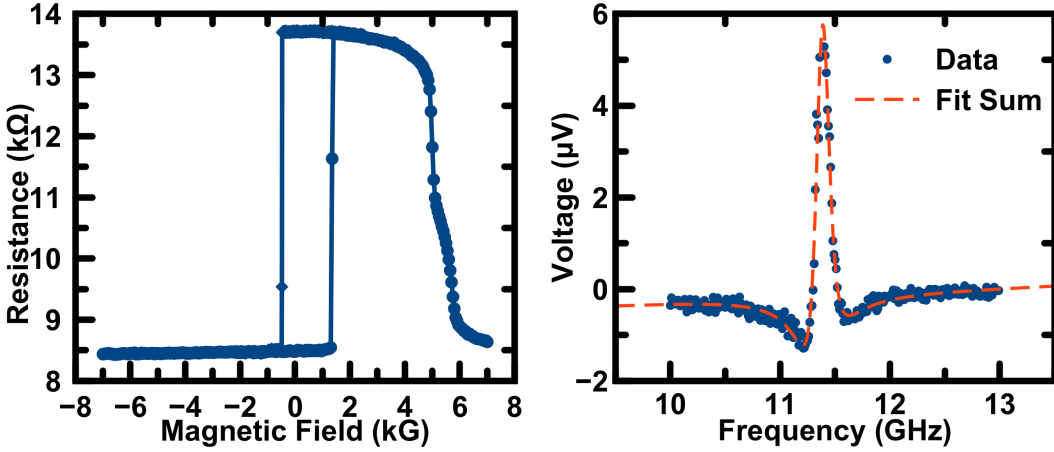


Figure 3.3: (a)Magneto-resistance plot of the sample studied. SAFTop layer start to flop around 4.5kG. (b)Blue dot:Typical ST-FMR spectrum with only lowest-frequency mode. Red dash line: Fitted curve to extract resonance frequency and linewidth.

mode. We are now going to derive the mathematical equation to extract resonance frequency and linewidth from the curve.

3.3 Gilbert Damping Evaluation

As we discussed in the previous chapter, the line shape $V_{mix}(f)$ without field modulation is a sum of symmetric $S(f)$ and antisymmetric $A(f)$ Lorentzians $V_{mix}(f) = V_sS(f) + V_aA(f)$, where $S(f) = \frac{1}{1+(f-f_r)^2/\sigma_r^2}$, $A(f) = \frac{(f-f_r)/\sigma_r}{1+(f-f_r)^2/\sigma_r^2}$, f_r is the resonance frequency and σ_r is the linewidth. When the modulation field is small, the RMS voltage signal $\tilde{V}_{mix}(f)$ measured

by the lock-in amplifier is proportional to the first derivative of the rectified voltage $V_{mix}(f)$ with respect to the modulated variable-the external magnetic field B .

$$\begin{aligned}\tilde{V}_{mix}(f) = & B_m \frac{dV_{mix}(f)}{dB} = B_m \left[\frac{dV_s}{dB} S(f) + \frac{dV_s}{dB} A(f) \right. \\ & + \frac{1}{\sigma_r} \frac{d\sigma_r}{dB} \times (2V_s A^2(f) + V_a [2A^3(f)/S(f) - A(f)]) \\ & \left. + \frac{1}{\sigma_r} \frac{df_r}{dB} (2V_s S(f) A(f) + V_a [A^2(f) - S^2(f)]) \right]\end{aligned}\quad (3.5)$$

Here B_m is the RMS amplitude of the modulation field, and the last term proportional to df_r/dB is usually dominant. If V_s and V_a are weak functions of magnetic field then the symmetric part of $\tilde{V}_{mix}(f)$ is proportional to V_a and the anti symmetric part is proportional to V_f .

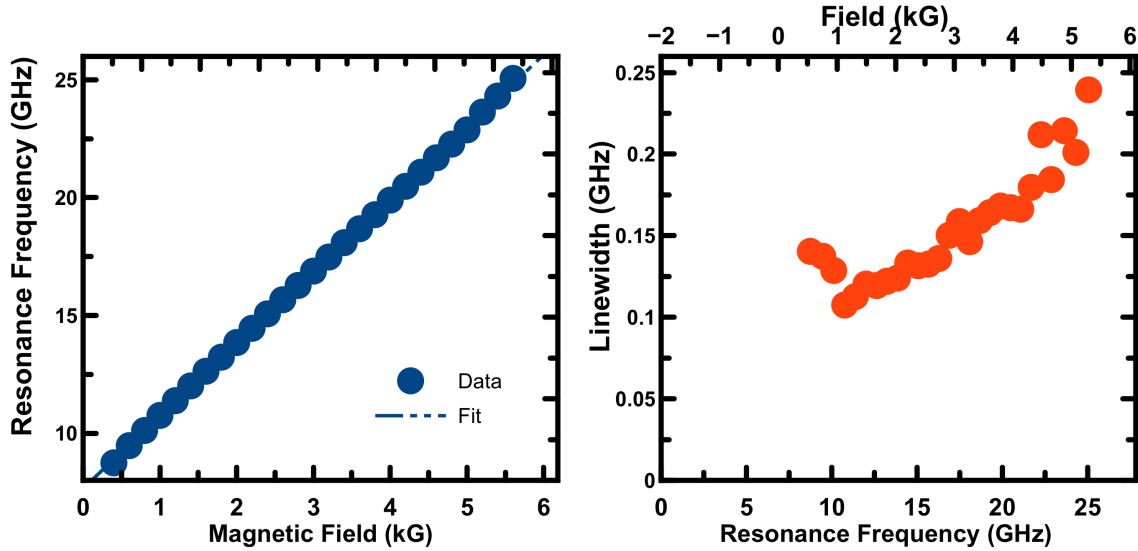


Figure 3.4: (a) Fitted resonance frequency plotted against external magnetic field (b)Fitted linewidth plotted as a function of resonance frequency.

Fig.3.4(a) shows the fitted resonance frequency of the quasi-uniform modes respect to the external magnetic field. As we expect from Kittel equation, there is a good linear relation.

Making an easy axis approximation, the Kittel equation is

$$f = \gamma(H_k \pm |H_{dip}| + H_{ext}) \quad (3.6)$$

Here H_{dip} is the center of hysteresis loop and H_{ext} is the external magnetic field. The quasi-uniform mode frequency at zero field gives magnetic anisotropy field of the free layer ($H_k = 2.5$ kG).

Next we try to fit for the damping parameter. Precision measurements of the spectral linewidth of the quasi-uniform mode required some improvements of our ST-FMR setup. We found that standing waves in the microwave measurement circuit can introduce significant errors into the measured line width. In order to alleviate the standing wave problem, we introduced a significant length (1.5–2 meters) of a microwave cable between the sample and the bias tee used in the ST-FMR setup. This additional length acted as a microwave attenuator that does not generate significant signal reflection (adiabatic absorptive attenuator). Fig.3.5 illustrates the degree of improvement of the ST-FMR signal quality offered by the cable attenuator—the spectral peak splitting artifact is completely eliminated and reliable measurements of the spectral linewidth become possible.

Previous work has been shown that Gilbert damping parameter can be determined from the linewidth from the FMR signal[9]. Fig.3.4(b) shows the linewidth plotted as a function of resonance frequency. We would expect to observe a linear relation if only considering Gilbert damping contribution. From our data, however, we can observe obvious two regions which deviate from a simple linear fitting. Firstly, at low frequency around 10GHz, the linewidth was clearly broadened and was larger than other region. Secondly, at higher frequency above 20GHz, the linewidth has more noise in terms of relative fluctuations. Moreover, if we try to fit the linewidth data and extrapolate to zero frequency, we found there is a large non-zero intercept. It is not clear whether this non-zero intercept is due to some

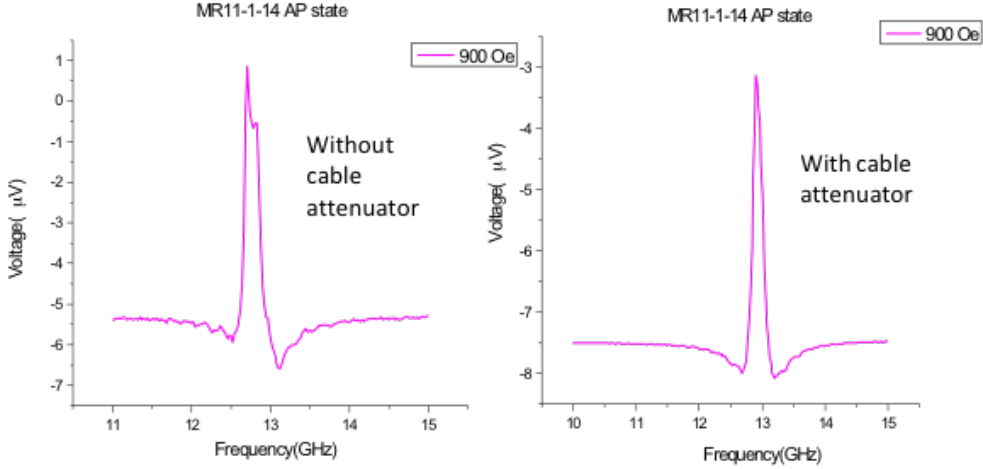


Figure 3.5: ST-FMR spectrum measured without a long attenuating cable attached to the sample (left) is significantly distorted by standing waves in the microwave circuit. (right) The same spectrum measured with a long attenuating cable eliminates the standing wave artifacts.

inhomogeneous broadening in our sample or some other mechanism. There exist different mechanism responsible for possible linewidth broadening[66].

To fully understand the magnetic dynamics excited in the magnetic tunnel junctions, we make the full ST-FMR measurement and shows the 2D contour plot of the results in Fig.3.6. At lower magnetic field(0-2kG), we can mainly observe three free layer modes. These three modes are parallel to each other and the lowest frequency Q mode is the quasi-uniform mode, which has been used to determine the anisotropy constant. Two higher order mode labeled as F1 and F2 are distinct from this 2D contour plot although they are hard to distinguish from single spectrum. Starting from 2kG, at lower frequency, there is another mode appearing in the contour plot. This mode, labeled as S mode, has a different dispersion relation: the resonance frequency decreases with increasing magnetic field. This mode can be identified as acoustic mode generating from the SAF layer. The important feature here is that, if we extrapolate the S mode into lower magnetic field, the S mode will be coupled with Q mode around 10GHz at zero field.

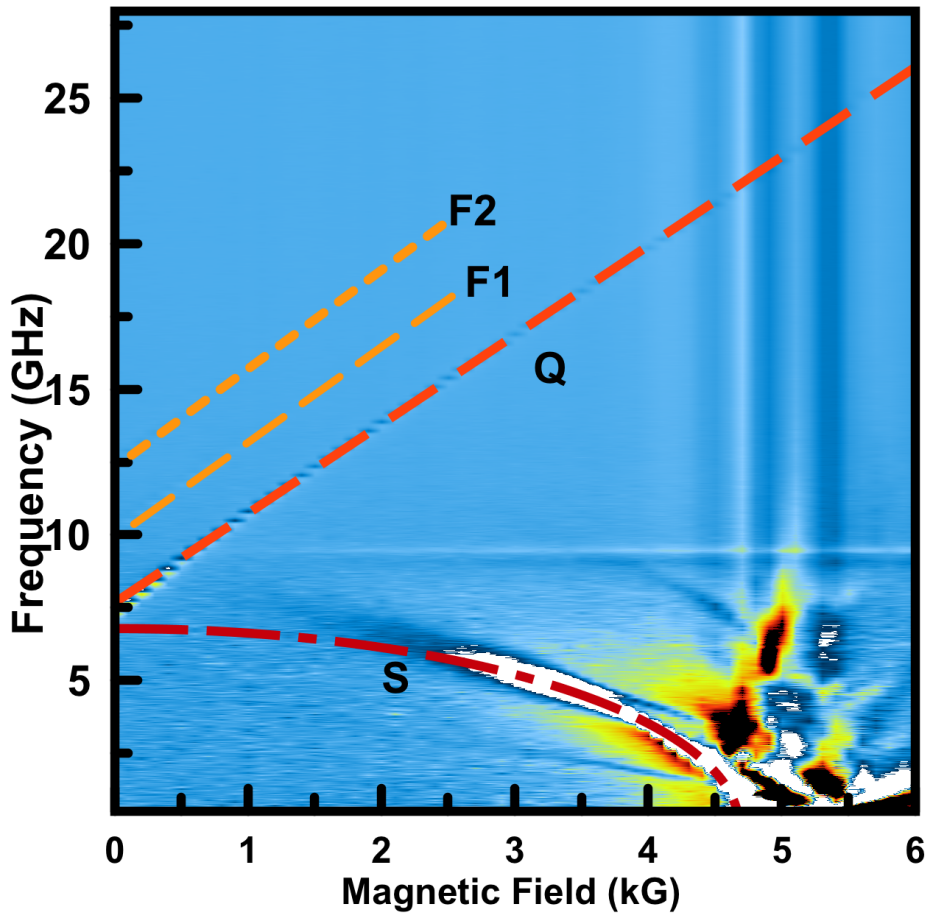


Figure 3.6: ST-FMR spectra measured as a function of out-of-plane magnetic field. Q labels the quasi-uniform mode of the free layer while F2 and F3 are the higher order spin wave modes of the free layer. S labels the acoustic SAF mode.

When we have the resonant coupling between these two modes, the linewidth would be broadened by this resonant coupling mechanism. This is exactly what we have found from Fig.3.6 in the lower frequency region.

In the 2D contour plot, around 4kG magnetic field, as we can see from Fig.??, the SAF layer becomes unstable and enter the spin-flop region. In this region, because of unstable SAF layer, the stray field from SAF layer acting on the free layer is also very unstable and

produce large magnetic noise during the ST-FMR measurement. As a result, we find there are more fluctuations in the linewidth data as we see from Fig.3.4(b) around 20GHz.

As we have learned from the 2D contour plot, in order to reliably fit for the damping parameter in the free layer, we need to first exclude the resonant coupling region in the lower frequency, in which the linewidth was broadened by the interaction between free and SAF layer. We also need to avoid the high frequency region. In Fig.3.7 we only include the linewidth data from 10GHz to 20GHz and determine the Gilbert damping to be 0.007 from the slope.

Here the intercept Δf_0 is linewidth at zero resonance frequency, which is often due to inhomogeneous effects such as the dispersion in effective anisotropy field from the distributions of demagnetization field and stray field[67]. From the fitting of the slope, we obtain a low Gilbert damping value around 0.006, which is consistent with other measured Gilbert damping value for the CoFeB-based free layer in similar work[68]. Such a small value of Gilbert damping is essential for lowering critical switching voltage as we previously discussed. The critical switching voltage given by Eq.2.15 is 0.85 V. From the intercept at zero resonance frequency, we obtained the intercept Δf_0 around 0.0392 GHz. We would like to further investigate the non-zero intercept and the inhomogeneity in the free layer of the MTJs by micromagnetic simulations.

3.4 Continuous wave Micromagnetic Simulations

To understand the linewidth and nature of non-intercept intercept we observed, we perform continuous wave micromagnetic simulations of magnetization dynamics using OOMMF software[69]. To fully account the magnetic dynamics in all layers, we employ a three-dimensional with three ferromagnetic layers: free, SAF top and SAF bottom. We use ma-

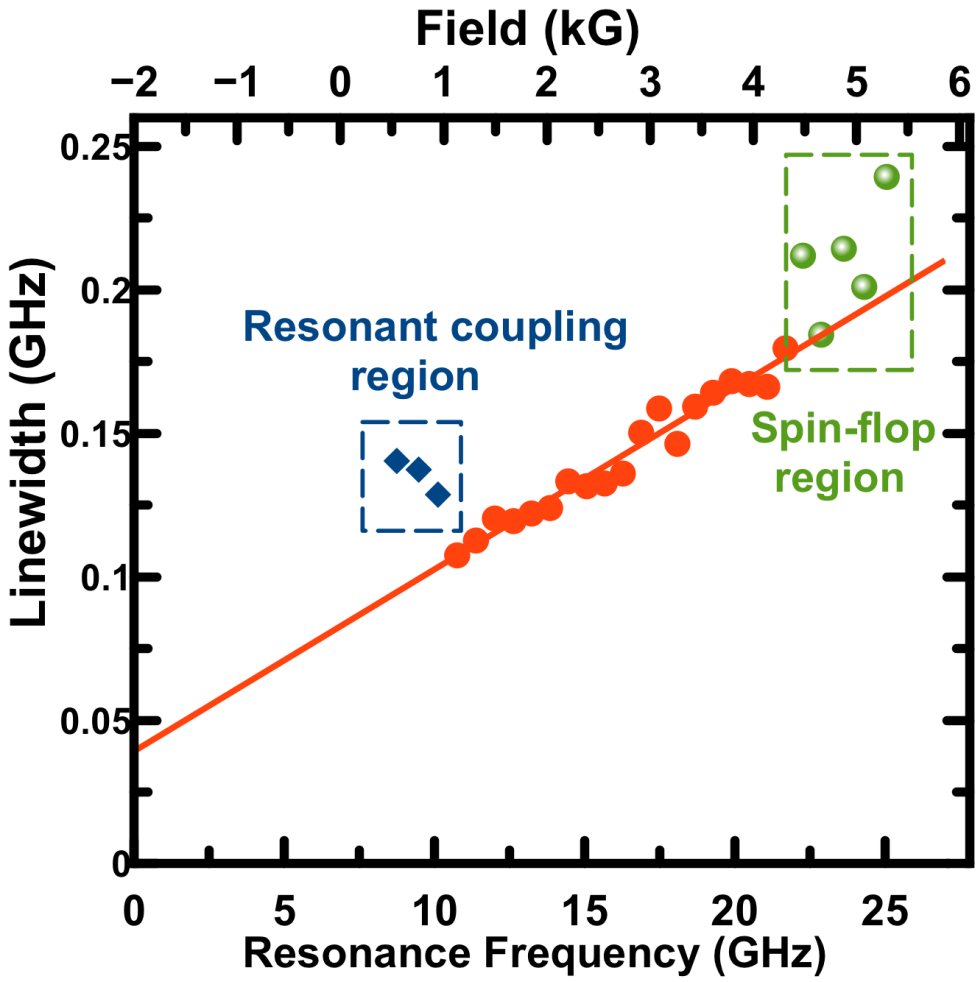


Figure 3.7: Spectral linewidth of the free layer quasi-uniform mode versus frequency of the mode. Line is the best fit to the data outside of the SAF spin flop and SAF resonant coupling regions.

terial parameters obtained from independent measurements and/or their accepted literature values. The cell size used is 0.25 nm, which is comparable to the grain size observed in the CoFeB system[70].

In the simulations, the spin wave dynamics is excited by a combined pulse of spin-torque and Oersted field, both resulting from a sine-wave-driven current. During the simulation process, we first relax the system under static magnetic field to reach the ground state. Then the magnetization is excited by sine-wave drive and oscillate with increasing ampli-

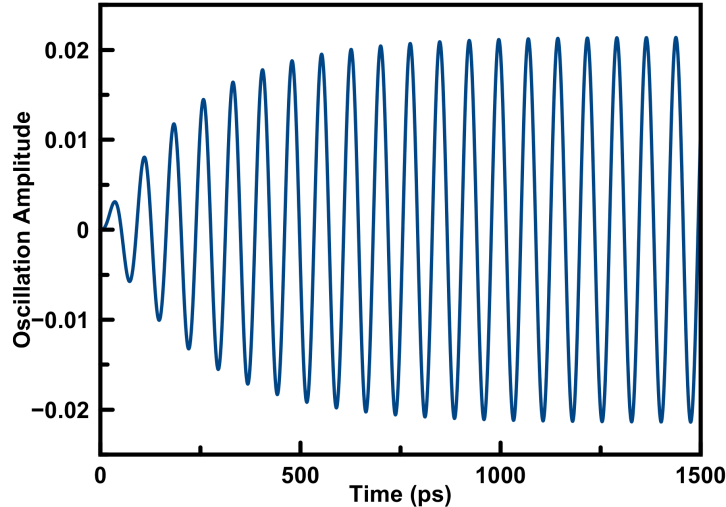


Figure 3.8: Spectral linewidth of the free layer quasi-uniform mode versus frequency of the mode. Line is the best fit to the data outside of the SAF spin flop and SAF resonant coupling regions.

tude. After a certain period of transient time, the magnetization will precess steadily and enter dynamic equilibrium. To illustrate this process, we can plot the magnetization as a function of simulation time as shown in Fig.3.8. The magnetization first undergoes a period of transient time and then enter a steady oscillations, which yields a certain value of oscillation amplitude and phase. For each driven frequency, we can determine corresponding amplitude of the oscillation at a constant magnetic field. The blue dot from Fig.?? show the oscillation amplitude of the in-plane component of magnetization as a function of applied frequency at 2000 Oe field, which shows a typical Lorentzian curve as expected[53]. From the simulation, We can adjust the perpendicular uniaxial anisotropy in order to reproduce the same experimental resonance frequency(7.54 GHz) at zero magnetic fields. The fitted uniaxial anisotropy is $4.05 \times 10^5 J/m^3$. Compared with the magnetic anisotropy field we

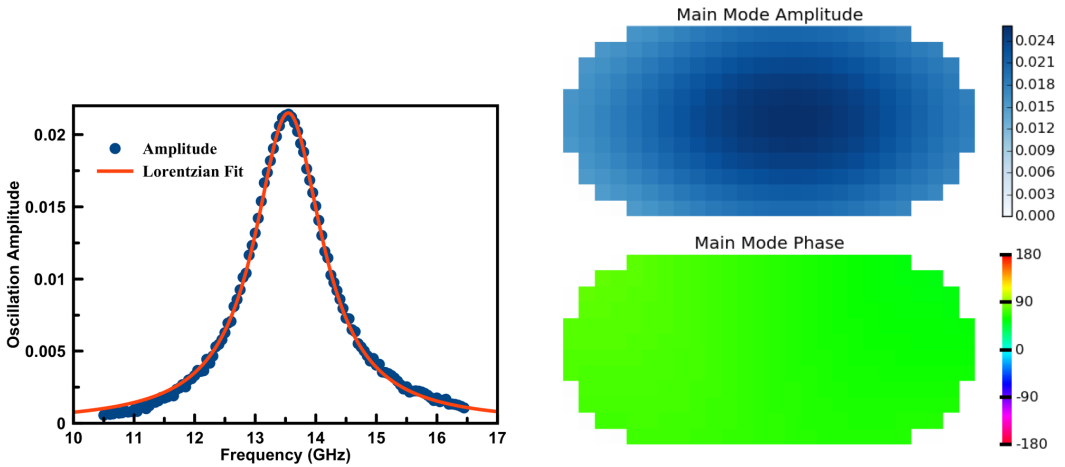


Figure 3.9: (a)Blue dot: Simulated amplitude versus driven frequency. Red line: Fitted Lorentzian curve. (b)Spatial profile of mode amplitude(Top) and phase(Bottom) of the mode excited in the continuous wave. The amplitude and phase are both uniform across the device, indicating a quasi-uniform eigenmode.

measured from field-modulated ST-FMR methods, we can also calculate the perpendicular uniaxial anisotropy field from the following equation [71]

$$H_k = 2K_u/M_s - 4\pi M_s. \quad (3.7)$$

Here H_k is the effective magnetic anisotropy, K_u is the uniaxial perpendicular magnetic anisotropy and M_s is the saturation magnetization. The PMA calculated from experimental value is $4.73 \times 10^5 J/m^3$, which has around 15% deviation from micromagnetic simulated value. This discrepancy in the magnetic anisotropy shows the deviations between the macrospin Kittel equation and the simulated micromagnetic model.

Let us now focus the simulated linewidth from this continuous wave simulations. In this type of simulation, we adopt the Gilbert damping value of 0.05 to avoid longer relaxation and simulation time. By simulating the spectrum at the different magnetic field, we can also

fit for the resonance frequency and linewidth as we have done experimentally in Fig.3.4(b). The blue dot and dashed line in Fig.3.10 shows such data from this simulation. The fitted Gilbert damping constant α is 0.05 with an intercept at zero frequency Δf_0 0.002, which shows that at this perfectly uniform model, the inhomogeneous broadening should be really weak and the Δf_0 should be close to zero. We find that this type of finite cell simulation does not introduce a large non-zero intercept at zero frequency as we observed from the experiment.

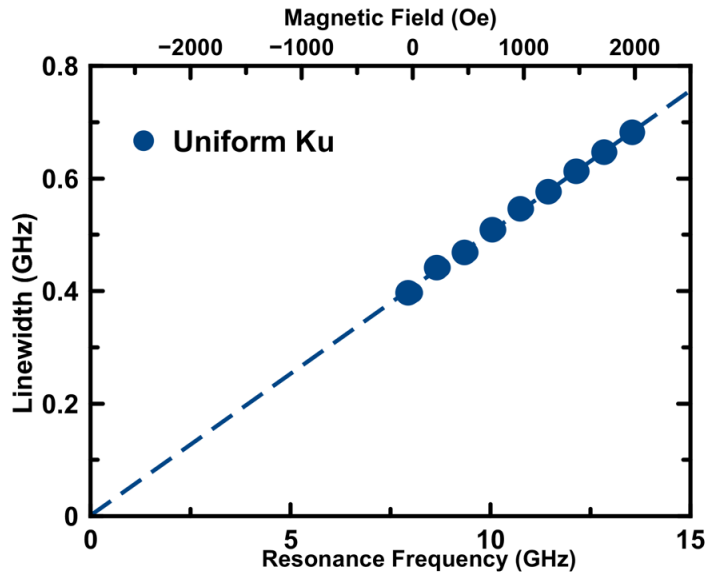


Figure 3.10: ST-FMR spectra measured as a function of out-of-plane magnetic field. Q labels the quasi-uniform mode of the free layer while F2 and F3 are the higher order spin wave modes of the free layer. S labels the acoustic SAF mode.

In the next step of the micromagnetic simulation, we introduce a random anisotropy field that varies spatially. The perpendicular uniaxial anisotropy value at the micromagnetic cell is drawn uniformly from the minimum and the maximum value, which are $3.55 \times 10^5 J/m^3$ and $4.55 \times 10^5 J/m^3$ respectively. This variation in the perpendicular uniaxial anisotropy corresponding to the effective magnetic anisotropy to range from in-plane direction 0.1 kG to perpendicular direction 0.21 kG in the simulations(assuming uniform magnetizations across the free layer). We can then repeat the simulation procedure as described above. The red dot and fitted curve at Fig. 3.11(a) shows the amplitude versus frequency response with

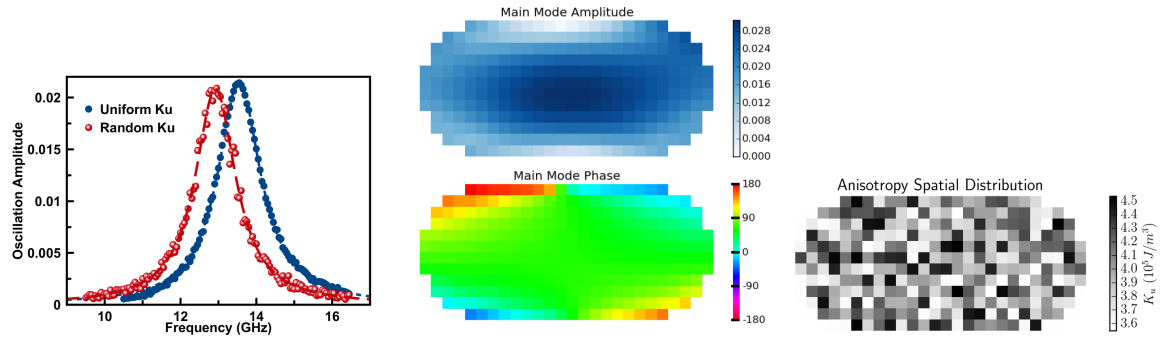


Figure 3.11: (a).Simulated spectrum with random magnetic anisotropy(in red dot) compared with spectrum with uniform magnetic anisotropy(blue dot) (b) Top: Spatial profile of the mode amplitude excited. Bottom: Spatial profile of the mode phase. (c)Spatial distributions of the magnetic anisotropy when introducing the random distributed magnetic anisotropy in OOMMF.

this anisotropy fluctuations. Now we still have a Lorentzian curve with some extra noise, which is due to the randomness of anisotropy introduced in the free layer. We can still look at the mode amplitude and phase, as shown in Fig.3.11(b). Compared with Fig.3.9(b) we start to see some deviations from uniform excitations, with nodes along the edges. Fig.3.11(c) shows the spatial distributions of the random anisotropy across the sample. We can also plot the linewidth as a function of resonance frequency as shown in the green dot in Fig.3.12. The fitted Gilbert damping value is 0.051 with a intercept -0.0027 GHz. From here we can conclude that only introducing random fluctuations of anisotropy does not reproduce the experimental intercept value.

In the final step of the simulation, we decrease the exchange constant between each grain from 20 pJ/m to 5 pJ/m. We can also plot the linewidth versus frequency as it is shown in the red dot from Fig.3.12. The slope of this green line gives a Gilbert damping value of 0.04733, which is slightly different from the input damping value. Most importantly, the intercept at zero frequency Δf_0 is broadened to 0.043. This value is indeed close to our experimentally determined Δf_0 , 0.0392.

In fact, since the CoFeB free layer is composed of grains, each with slightly different anisotropy, with strong exchange coupling inside of the grain and weaker exchange coupling among the grains[70]. In our simulation, by introducing random anisotropy field and decreasing the exchange stiffness with micromagnetic cell size close to the typical grain size of the CoFe crystals, we are reproducing the locally variant anisotropy field among the free layer, which contributes to the non-zero intercept Δf_0 we observed from previous ST-FMR measurement. Thus, we can qualitatively quantify the degree of random fluctuations of the magnetic anisotropy in the free layer of the MTJs.

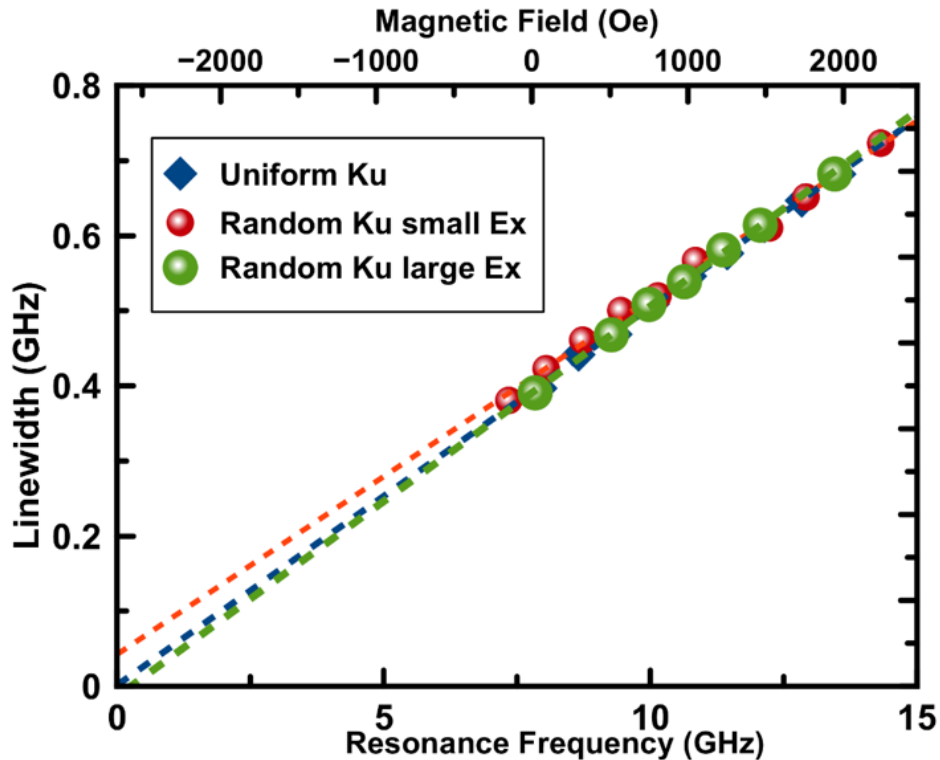


Figure 3.12: Summary of simulated linewidth plotted versus resonance frequency with different material parameters. From the plot only random magnetic anisotropy combined with small exchange stiffness leads to a significant linewidth intercept at zero resonance frequency.

We can summarize the simulation results from Table3.1. It is clear that only combining low exchange stiffness with random fluctuations of magnetic anisotropy would lead to linewidth broadening at zero resonance frequency.

	Gilbert damping α	Intercept Δf_0
Uniform Uniform	0.05	0.0016 ± 0.0064
Random Ku with small Ex	0.047	0.043 ± 0.013
Random Ku with large Ex	0.051	-0.0027 ± 0.0088

Table 3.1: Summary of continuous micromagnetic simulations result.

3.5 Micromagnetic Simulations of higher order modes

In order to fully understand the magnetic dynamics being excited in the Magnetic Tunnel Junctions, we perform micromagnetic simulations using OOMMF package[69]. To fully account for all magnetic interactions in the MTJ, we use a three dimensional model with three main functional layers: free layer, SAF top and SAF bottom layer. In the simulation, spin wave dynamics is excited by a combined pulse of ST and Oersted field, both resulting from a sinc-shaped spatially uniform current pulse with the amplitude $J_C \frac{\sin(2\pi f_{ct'})}{2\pi f_{ct'}}$ with the amplitude the cut-off frequency around 20 GHz, and the time variable $t_0 = 500$ ps. The need to combine the excitation from Spin torque and Oersted field is to include the uniform and non-uniform spin wave modes in the MTJs[72]. The spatial profile of the Oersted field is assumed to be that of a long wire with elliptical cross section. The direction of the ST vector acting on the free layer is determined by the magnetization orientation of the SAF top layer. Spectrum of spin wave eigenmodes is obtained via the Fast-Fourier-transform (FFT) of the time dependent in-plane component of the MTJ net magnetic moment.

Fig.3.13(a) shows a typical ST-FMR spectrum from our measurement. For this sample, we can identify five spin wave modes. The zero mode is the uniform excitation and we have already used this mode to fit for magnetic anisotropy and Gilbert damping value. The other four modes are non-uniform modes excited along the edges. On the left, Fig.3.13(b) shows the simulated spectrum from our micromagnetic calculations. As we discussed before, we perform the Fast-Fourier-transform on the in-plane component of the MTJ net magnetic moment and plot it against driven frequency. The top layer is the free layer and the middle(bottom) is the

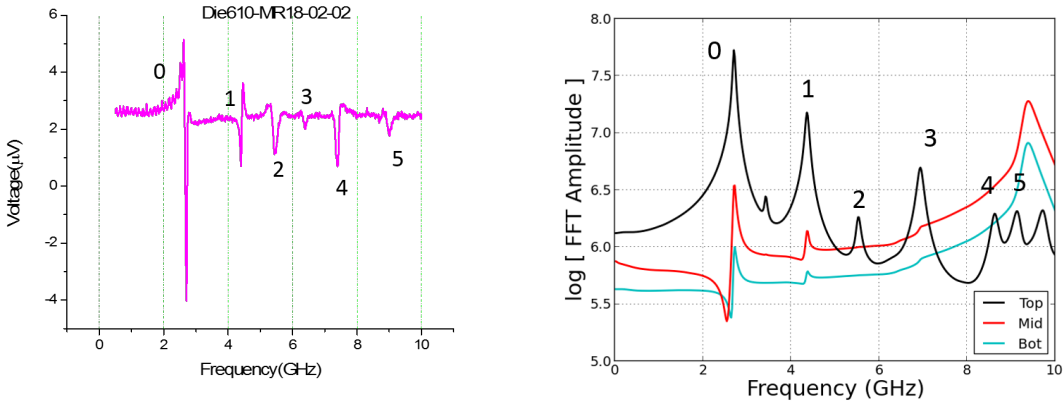


Figure 3.13: (a) ST-FMR spectrum of a 30 nm by 150 nm stadium-shaped STT-MRAM element. Several spin wave eignemode resonances are seen in the spectrum. (b)Fitted spectrum from micromagnetic simluations.

SAFTop(SAFBottom) layer. As we can see from the plot, the amplitude of the top layer is definitely much larger than the other layers, meaning the excitation of the MTJs is dominant by the free layer. The peaks in the spectrum are corresponding to the spin wave modes we observe from the experiment. By tuning the material parameter such as magnetic anisotropy and exchange constant, we can match the frequency position of the first zero mode and the second mode. So firstly, from micromagnetic simulations, we can determine the magnetic anisotropy to be $3.13 * 10^5 J/m^3$ and exchange stiffness constant to be around $5 * 10^{-12} J/m$.

Next we would like to understand the nature of the modes we excited. To do this, we perform the spatial mapping of the mode amplitude and plot it in Fig.3.14. Starting from the top left, we list the model profile for all the five modes. As expected, the first mode is uniform excitation so the amplitude of this mode is uniform. The second mode has two nodes along the short axis. So we label it as Mode(2,0). Then we have modes from Mode(3,0) and Mode(4,0) which have three or four nodes along the short axis. The last mode has one node along the long axis, so it is labeled as Mode(0,1).

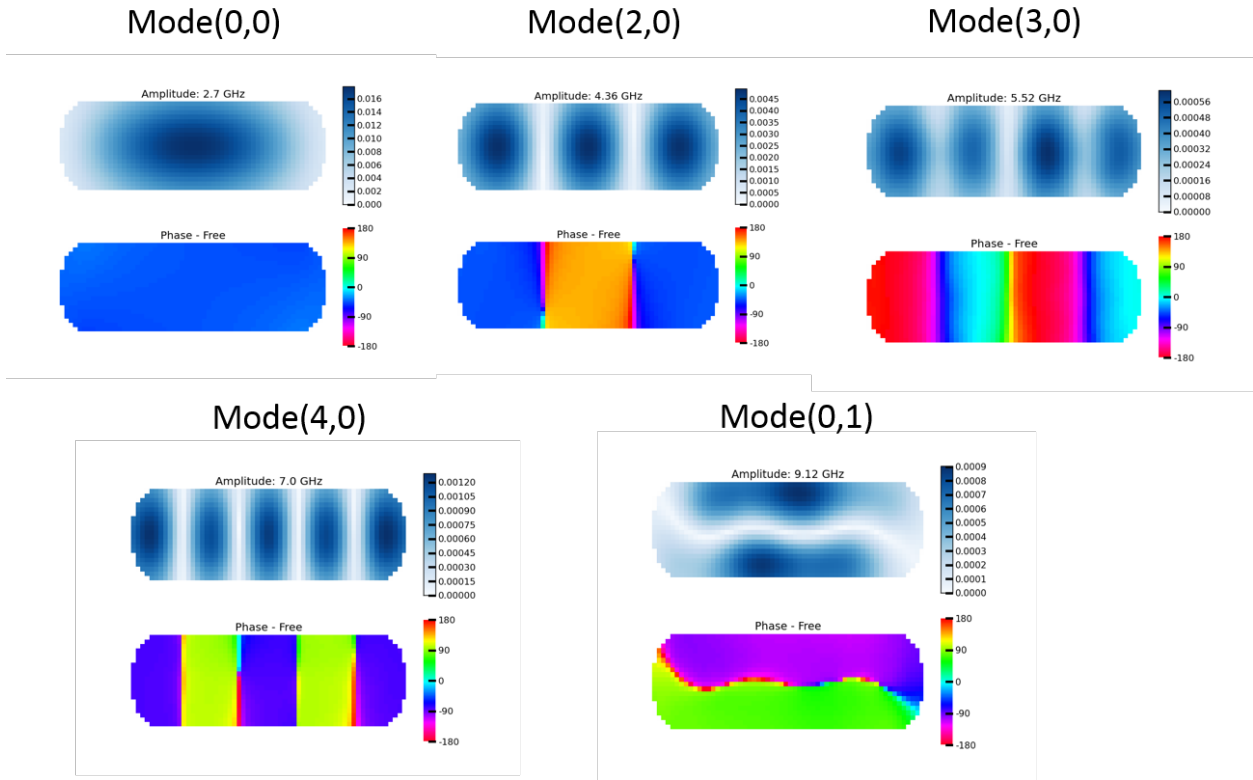


Figure 3.14: Spatial mapping of modes excited in the micromagnetic simulations.

After that, we find that no matter how we tune the magnetic anisotropy and exchange constant, the latter three modes can not be matched very well from experiment and simulations. So we have to consider another possibilities. One thing to consider is magnetic edge damage of the MTJ element. Such modifications are unavoidable in the STT-MRAM fabrication process due to etching of the element, and they are predicted to have significant impact on current-driven switching of the free layer. We tested several micromagnetic models of the magnetic edge damage and found how these models modify the frequencies of spin wave eigenmodes. We then compared the models predictions to our measurements of spin wave spectra by spin torque ferromagnetic resonance. This comparison allowed us to determine which model best describes the experimental data. More specifically, we have tested three models of the magnetic edge damage:

- Magnetic dilution model. In this model, saturation magnetization and exchange stiffness of the free layer of STT-MRAM are reduced in the edge region.
- STT-MRAM shape distortion model. In this model, the MTJ nanopillar shape is distorted with respect to its nominal shape.
- Anisotropy reduction model. In this model, magnetic shape anisotropy is reduced near the sample edges.

Fig.3.15(a) shows the results by exploiting edge damage model in the simulation. From this plot we find that this mode cannot adequately describe the experimentally observed spectrum of spin wave eignemodes in STT-MRAM samples we experimentally studied. Compared with the edge anisotropy model in Fig.3.15(b), now we have a much better agreement between experiment and simulations. We, therefore, conclude that the major impact of the STT-MRAM edge on magnetic properties of the device is reduction of perpendicular magnetic anisotropy near the device edge. This reduction can result in nucleation of current-driven magnetization reversal near the sample edges Comparison of ST-FMR measurements of spin wave mode frequencies can quantify the degree of magnetic anisotropy reduction near the sample edges. We discuss how this can be accomplished in the next paragraph.

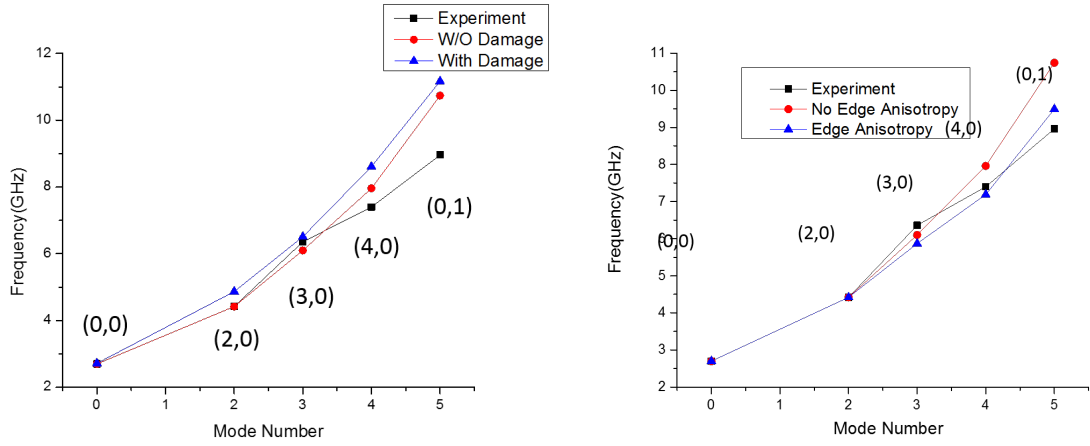


Figure 3.15: (a) ST-FMR spectrum of a 30 nm by 150 nm stadium-shaped STT-MRAM element. Several spin wave eignemode resonances are seen in the spectrum. (b)Fitted spectrum from micromagnetic simulations.

From fitting the first and second mode frequencies, we already have a confidence value of magnetic anisotropy and exchange constant. Then we employ the models of spatially non-uniform parameters of the free layer. The blue symbols in the left panel of Fig.3.15(a) show results of the simulations for the magnetic edge dilution model. In this model, both the saturation magnetization and the exchange constant of the free layer are gradually reduced from their bulk values to zero at the free layer edge. The distance over which this reduction takes place was chosen to be in the 2.5 nm to 7.5 nm range (typical material damage depths due to various types of etching). It is clear from Fig.3.15(a) that the magnetic dilution model does not improve the agreement between theory and experiment. We have also found that shape distortions of the free layer do not reproduce the experimental results well. In contrast, reduction of magnetic anisotropy from $3.13 * 10^5 J/m^3$ in the free layer interior to $3.03 * 10^5 J/m^3$ at the free layer edge over a distance of 2.5 nm gives a much better agreement with the experimental data as shown by blue symbols in the Fig.3.15(b). This type of fitting allows us to obtain the exchange stiffness constant of the free layer, its perpendicular magnetic anisotropy value and the magnitude of reduction of the perpendicular anisotropy at the sample edge.

3.6 Circular STT-MRAM Devices with Broken Symmetry

While stadium-shaped or rectangular samples are convenient for studies of the edge damage due to their particularly simple spin mode structure, studies of circular STT-MRAM samples are important because this shape is the primary candidate for STT-MRAM. We performed ST-FMR measurements of circular STT-MRAM samples and measured their spin wave spectra as a function of the nanopillar diameter. Fig.3.17 shows two examples of such spectra for STT-MRAM cells with diameters of 250 nm and 80 nm measured as a function of out-of-

plane magnetic field. A large number of modes are observed for the 250 nm sample due to the relatively weak geometric confinement of spin waves in the large structure. For these larger devices, it would be relatively hard to identify all the modes excited. While you can still fit for some of the spin-wave modes, the frequency spacings between each mode is relatively small, which makes further quantitatively analysis.

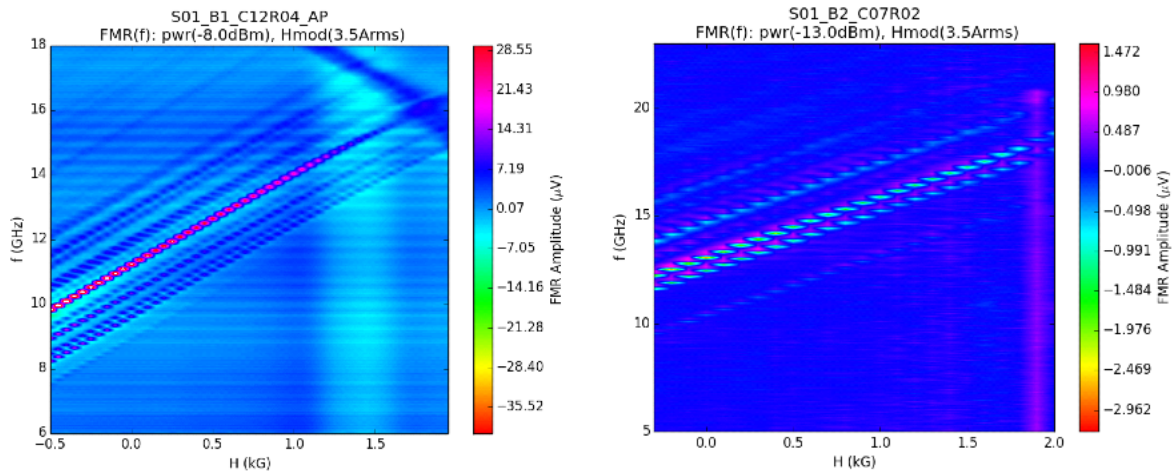


Figure 3.16: ST-FMR spectra of circular STT-MRAM cells with 250 nm diameter (left) and 80 nm diameter (right) measured as a function of the out-of-plane magnetic field applied to the nanopillar.

When we move to much smaller devices, fewer spin wave modes with larger inter-mode frequency gaps are seen for the 80 nm sample. The spin wave mode structure in circular STT-MRAM samples is qualitatively different from that in the stadium-shaped samples. The modes are characterized by two indexes: $n = (0, 1, 2)$ and $L = (0,1)$ [59]. The index n gives the number of spin wave nodes in the radial direction, while the index L describes azimuthal phase variation of the mode. Spatial profiles of the three lowest-frequency modes in a perfectly circular sample with 60 nm diameter are shown in Fig. 3.17. The first mode(labelled as $(0,0)$) is the lowest-frequency quasi-uniform mode. The second mode(labelled as $(0,1)$) is the first higher-order mode, it has larger amplitude at the edges and a node at the center. The last mode in 3.17 is labelled as $(1,0)$, which has a node along the edges of the device. This is the case when we have a perfect circular shape MRAM sample.

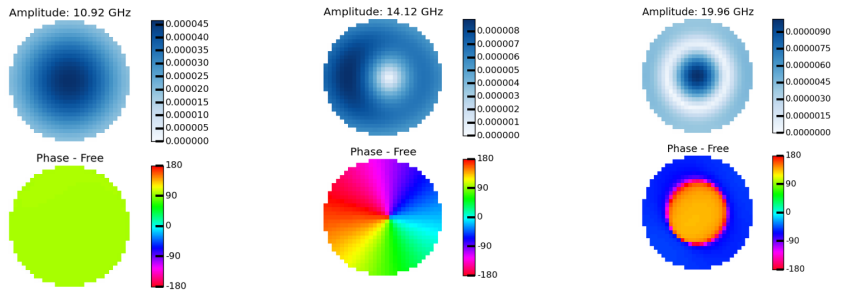


Figure 3.17: Three lowest-frequency spin wave eigenmodes of the free layer of a circular STT-MRAM sample with 60 nm diameter. The top image shows the spatial map of the amplitude of the mode while the bottom image shows the spatial map of the spin wave modes phase

However, in our experimental data, we find the frequency of the second higher-order mode(label as mode(0,1)) is considerably larger than micromagnetic simulations. To confirm this finding, we measured more than ten MRAM devices with the same nominal dimension. The ST-FMR spectra of all circular samples we studied exhibit one common feature: the lowest frequency (quasi-uniform) mode always appears as a singlet while the two higher frequency modes appear as a doublet with relatively small inter-mode frequency splitting (~1GHz). Furthermore, we find there is a distribution of all the three modes frequencies. Fig.3.18(a) summarizes the experimental results, which shows the statistics of the mode frequencies at zero field for different modes. We find that the distribution is somewhat skewed towards lower frequencies. We also notice that there is a clear visibly larger spread for the (1,0) and (0,1) modes compared to the (0,0) mode. This is because the (1,0) and (0,1) mode frequencies are also affected by random in-plane anisotropy fluctuations due to e.g. elliptical shape distortions.

The (0,0) mode frequencies can be used to quantify the average anisotropy field and the anisotropy field distribution. It is also interesting to compare the distributions of the main modes as a function of the device dimensions. Fig.3.19(a) shows the frequency of the Mode 1 versus frequency of the Mode 0 and Fig.3.19(b) shows the frequency of the Mode 2 versus frequency of the Mode 0. We can find a clear linear correlation between the quasi-uniform and

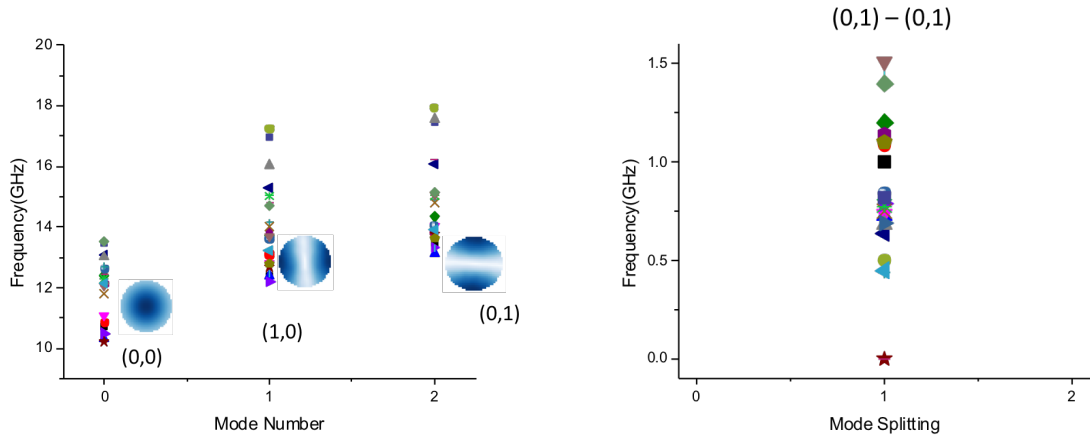


Figure 3.18: (a) Statistics of the mode frequencies at zero field for different modes. (b) Statistics of mode splitting between the $(1,0)$ and $(0,1)$ modes for 80 nm samples.

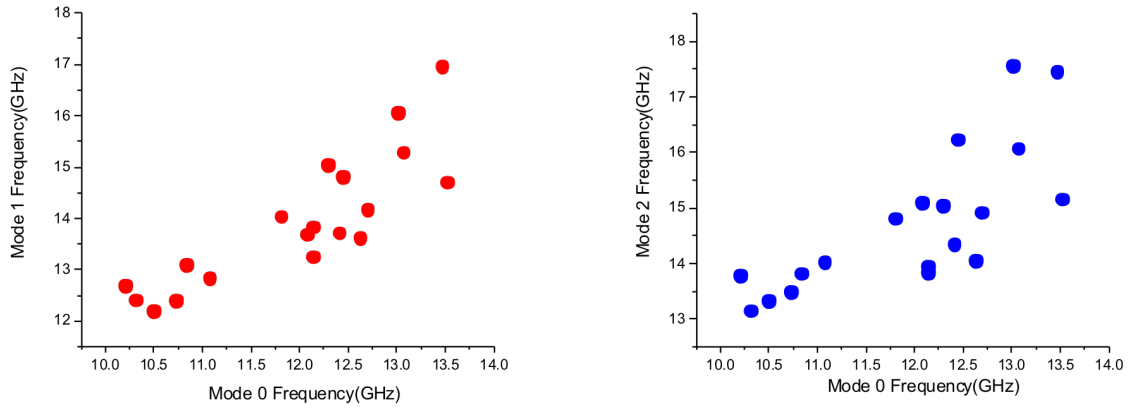


Figure 3.19: Statistics of mode splitting for 80 nm sample. (a):Frequency of the Mode 1 versus frequency of the Mode 0. (b):Frequency of the Mode 2 versus frequency of the Mode 0

the higher order mode frequencies, which reveals sample-to-sample perpendicular anisotropy fluctuations but fairly sample-independent exchange energy of the free layer. Since the exchange energy is closely related with sample dimensions, this also shows that the device geometries do not have large variations.

As we mentioned earlier, micromagnetic simulations of circular devices do not match with experimental data. Fig.3.20(a) ST-FMR spectrum of spin wave eignemodes in a circular 60 nm diameter MTJ nanopillar measured at 1 kG out-of-plane field. There are five modes are visible at low frequency and we are concentrating on the lowest three spin-wave modes. Fig.3.20(b) shows a simulated spectrum for a 60 nm STT-MRAM element. Vertical dashed lines indicate measured mode positions. Experimentally the frequency spacing between mode 1 and mode 2 is less than 1 GHz. However, the spacing in the micromagnetic simulations is quite large.

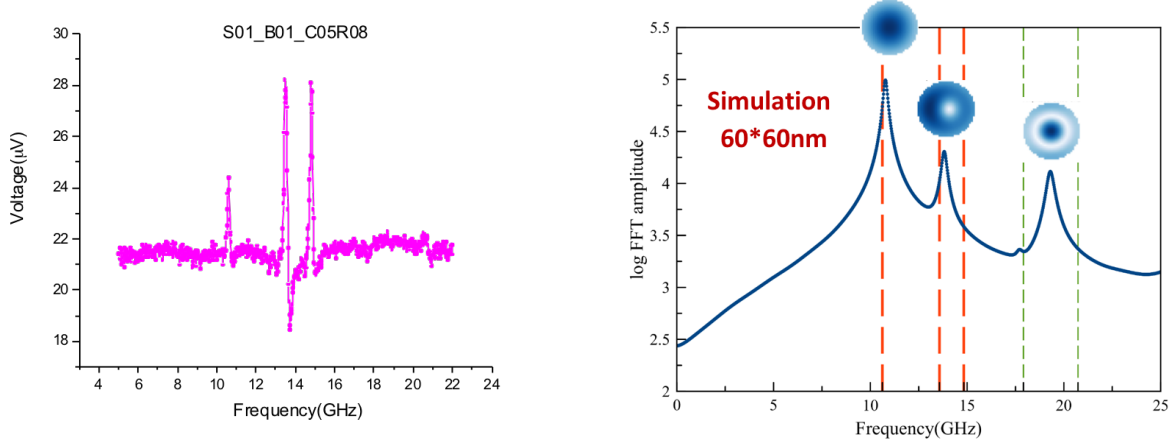


Figure 3.20: (a) ST-FMR spectrum of spin wave eignemodes in a circular 60 nm diameter MTJ nanopillar measured at 1 kG out-of-plane field. (b) Simulated ST-FMR spectrum of a 60 nm circular STT-MRAM element. Vertical dashed lines indicate measured mode positions. Micromagnetic simulated mode profiles are shown next to each mode.

The mode structures and discrepancy can be explained if the perfect circular symmetry of the system is broken. There are several candidates for this broken symmetry and the most possible one is the elliptical distortion of the nanopillar shape. During the fabrication of the STT-MRAM elements, certain processes, such as edge etching, are prone to cause device actual dimension to deviate from perfect circular shape. Such symmetry breaking has little effect on the quasi-uniform ($n=0, L=0$) mode, but it splits the ($n=0, L=1$) mode into two modes with a single node along either the short or the long axis of the ellipse. We

then examine the effect of the shape distortion on the excited spin wave mode structure via micromagnetic simulations. In the simulations, we replace the perfect circular shape by an ellipse with varying eccentricity. By varying eccentricity, we influence the degree of the spin wave mode splitting. Fig.3.21(b) shows a spectrum with device dimension 68 nm * 52 nm. The mode (0,1) split into two modes as we expect. Fig.3.21(a) shows a spectrum with device dimension 64 nm * 56 nm. As we can compare between those two spectrums, the first-order mode splits into two modes and the frequency gap between those two modes is increasing with increased eccentricity. For devices with larger eccentricity the mode gap is larger, which indicates the mode gap is closely related with shape deviations from perfect circular.

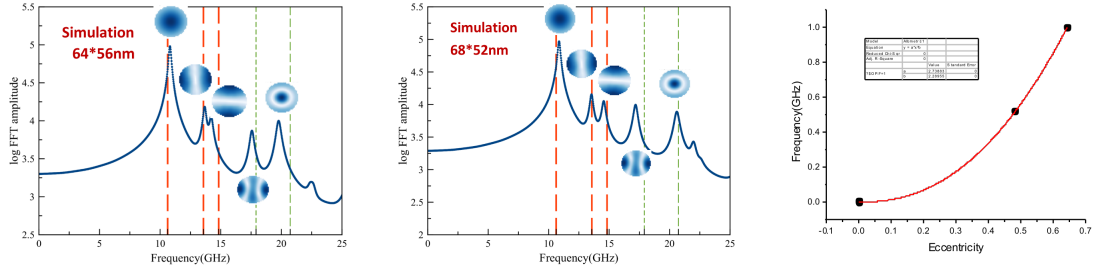


Figure 3.21: ST-FMR spectrum of spin wave eignemodes in a circular 60 nm diameter MTJ nanopillar measured at 1 kG out-of-plane field. Five modes are visible at low frequency. (b) Simulated ST-FMR spectrum of a 5268 nm² elliptical STT-MRAM element. Vertical dashed lines indicate measured mode positions. Micromagnetic simulated mode profiles are shown next to each mode. (right) Simulated splitting (frequency gap) of ($n=0, L=+1$) mode plotted versus eccentricity

With that in mind, Fig.3.21(a) shows the best micromagnetic fit to the experimental spectrum for a circular 60 nm MTJ nanopillar shown in Fig.3.20(a). The vertical dashed lines indicate the measured mode frequencies. The simulated mode frequencies agree well with the experimental results suggesting that the mode splitting observed in the experiment arises from MTJ shape distortions. The micromagnetic fitting gives the value of the perpendicular anisotropy ($K_u = 4.3 * 10^5 J/m^3$) and exchange stiffness constant ($A = 6.01 * 10^{-12} J/m$) of the free layer. Furthermore, Fig.3.21(c) shows simulated splitting (frequency gap) of ($n=0, L=+1$) mode plotted versus eccentricity. This enables us to establish a correlation

between the measured frequency gap and the degree of shape distortion, which is difficult to measure directly.

60nm sample	Mean(GHz)	Standard Deviation (GHz)	80nm sample	Mean(GHz)	Standard Deviation (GHz)	250nm sample	Mean(GHz)	Standard Deviation (GHz)
Mode (0,0)	22.04	1.15	Mode (0,0)	11.97	1.05	Mode (0)	10.32	0.19
Mode (1,0)	23.89	1.16	Mode (1,0)	13.96	1.45	Mode (1)	10.93	0.173
Mode (0,1)	24.62	1.29	Mode (0,1)	14.76	1.44	Gap	0.617	0.200

Figure 3.22: Three lowest-frequency spin wave eigenmodes of the free layer of a circular STT-MRAM sample with 60 nm diameter. The top image shows the spatial map of the amplitude of the mode while the bottom image shows the spatial map of the spin wave modes phase

We then study the mode splitting as a function of the nanopillar diameter. More than 15 devices of each MTJ diameter were measured to obtain reliable statistical distributions of the mode frequencies. First, we find that the 250 nm devices do not show splitting of the ($n=0, L=+1$) mode. This supports the picture of splitting of this mode due to deviations from the perfectly circular shape (little process-induced ellipticity is expected for these large circular devices). Second, for the larger 250 nm devices, standard deviation of the frequency distribution is much smaller than that for the 60 nm and 80 nm devices. We can then conclude that low-energy mode frequencies are sensitive to the average anisotropy over the free layer area. In the larger devices, averaging over a larger number of crystallographic grains and results in a tighter distribution of the free layer anisotropy values.

3.7 Possible Origin of WER Correlation with ST-FMR

We also collected preliminary data suggesting a correlation between ST-FMR spectra of circular MTJ nanopillars with write error rates of the devices. Fig.3.23 shows ST-FMR spectrum of spin wave eignemodes in a circular 40 nm diameter MTJ nanopillar as a function of out-of-plane magnetic field. This sample shows anomalous WER behavior (ballooning).

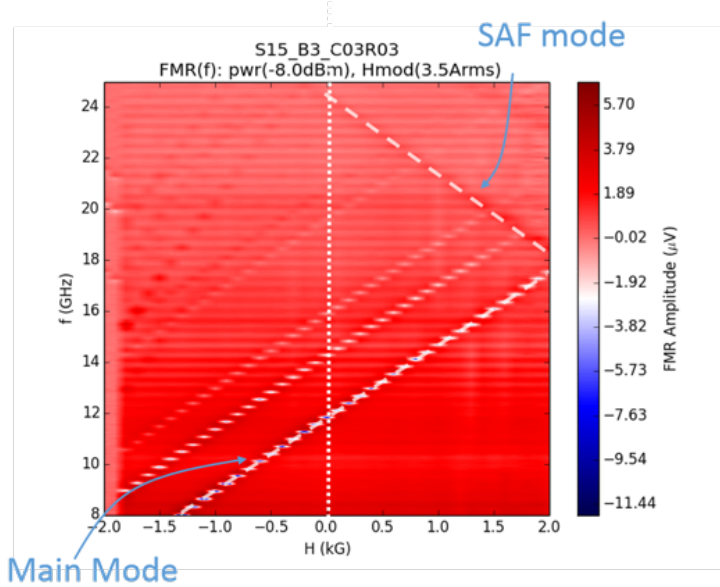


Figure 3.23: ST-FMR spectrum of spin wave eignemodes in a circular 40 nm diameter MTJ nanopillar with known anomalous WER behavior measured as a function of out-of-plane magnetic field. The SAF spin wave mode and the quasi-uniform free layer mode are labeled by dashed lines in the figure.

For this device, the frequency of the SAF mode in zero field is nearly twice the resonance frequency of the quasi-uniform mode of the free layer. This frequency coincidence condition suggests that a nonlinear three-magnon process (confluence of two magnons of the quasi-uniform mode into a single SAF mode magnon) should be resonant for this device in zero field. Such non-linear resonant scattering channel can drain energy an angular momentum supplied by spin torque to the free layer and impede the free layer switching process. Therefore, this nonlinear scattering process is suspected origin of the anomalous WER behavior. For all devices studied so far, we find that MTJs exhibiting anomalous WER do satisfy this nonlinear

resonant scattering (frequency coincidence) condition, while all devices with normal WER do not satisfy the nonlinear resonant scattering condition.

3.8 Field Modulated Mag-noise Measurement

We have developed a novel method of experimental characterization of the spectrum of spin wave eigenmodes of individual STT-MRAM elements. This method is magnetic noise spectroscopy with magnetic field modulation. Previous work[73][74] has demonstrated that even by applying a small DC current which is considerably smaller than the critical switching current, there will be a significant influence of spin transfer torque on thermally activated ferromagnetic resonance excitations. However it has not been showed that the Magnoise measurement can be applied to the Magnetic Tunnel Junctions(MTJs) with perpendicular magnetic anisotropy(PMA). We are also interested in applying the field modulation technique as we did from the ST-FMR measurement.

Fig.3.24 shows the experimental setup for measuring magnetic noise with magnetic field modulation, in which a microwave-frequency noise emitted by the STT-MRAM at a finite bias current is measured via a lock-in detection

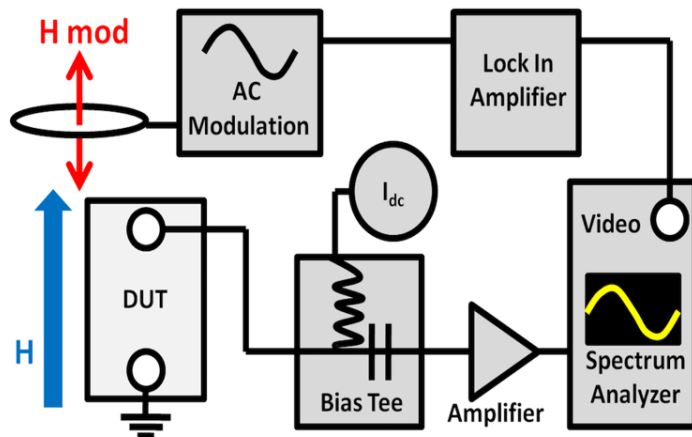


Figure 3.24: Set-up for Magnoise measurement

technique. The microwave noise is emitted at the frequencies of spin wave eigenmodes of the sample, with the most prominent features arising from spin wave eigenmodes of the free layer. The difference between the Magnoise measurement and the ST-FMR measurement is that, other than using a microwave generator to send a ac current into the MTJs, the MTJs are excited by a DC current and the spectrum analyzer is used to detect the ac signal at the resonance frequency.

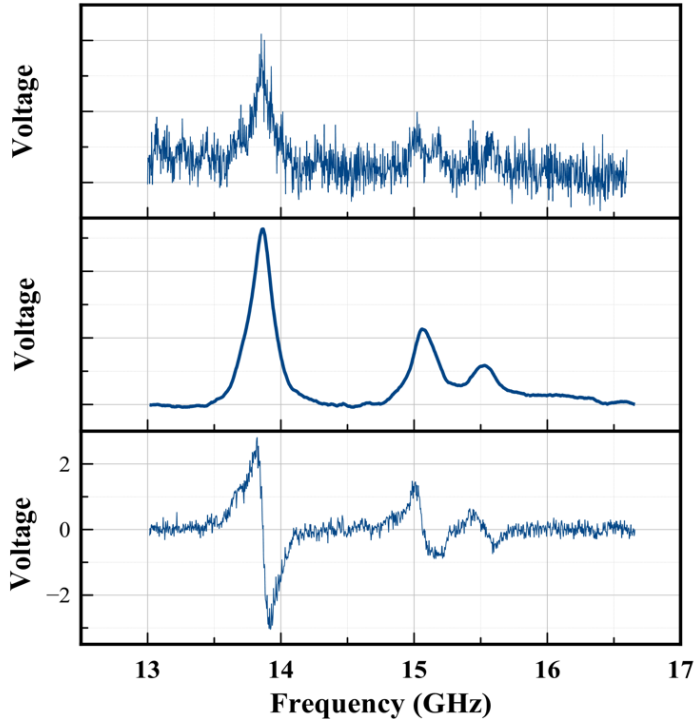


Figure 3.25: Summary of the magnoise measurement. Top: Raw spectrum taken without the field modulation. Middle: Integration of the spectrum taken with the field modulation. Bottom: Raw spectrum taken with the field modulation technique.

The top panel of Fig.3.25 shows the magnetic noise spectrum measured by conventional technique without magnetic field modulation. The conventional method only allows us to reliably measure the frequency of the quasi-uniform spin wave mode. The linewidth of the main mode is hard to fit accurately. We can also only measure the main mode and do not have enough

resolution to accurately fit for the higher order modes. In contrast, the data obtained with magnetic field modulation shown below allow us to detect not only the resonant frequencies but also the spectral linewidth of several spin wave modes of the device. This is enabled by the superior signal-to-noise factor of our technique with magnetic field modulation. The bottom panel of Fig.3.25 shows the same spectrum taken with field modulation technique. The signal-to-noise ratio is much improved and the higher-order modes can be resolved. To illustrate the nature of our field-modulation technique, in the middle panel of the Fig.3.25 we plot the integration of the bottom spectrum from the Fig.3.25. The integrated spectrum resembles the raw spectrum taken without field-modulation technique with all the excited modes coincide with each other. We can conclude that the field-modulation technique only improves the signal-to-noise ratio without distorting the spectrum. The data obtained with magnetic field modulation is of high enough quality to enable determination of the Gilbert damping, magnetic anisotropy and exchange stiffness constant of the free layer.

Now we would like to benchmark between the magnoise noise method and ST-FMR on a typical STT-MRAM cell. Fig.3.26(a) shows the magnetoresistive curve of the MTJ sample explored in this study. This device has TMR ratio around 180 percent and the coercive field close to 2 kG. Fig.3.26(b) shows the ST-FMR spectrum of this device at the AP state with three spin-wave modes excited.

One major feature of the magnoise measurement is to allow large dc bias into the MTJ and study the bias-dependent shift of resonance field and linewidth. Fig.3.27 shows dc-dependent spectrum taken from the magnoise measurement. Fig.3.27(a) shows the direct measurement of the bias-dependent magnoise measurement. Fig.3.27(b) shows the integration of the raw spectrum under dc-bias. Three spin wave modes are visible as labelled.

Now we can directly compare the bias-dependent measurement and main mode fitting using these two techniques. Fig.3.28(a) shows the frequency-domain ST-FMR measurement and Fig.3.28(b) shows the frequency-domain magnoise measurement. We fit both the resonance

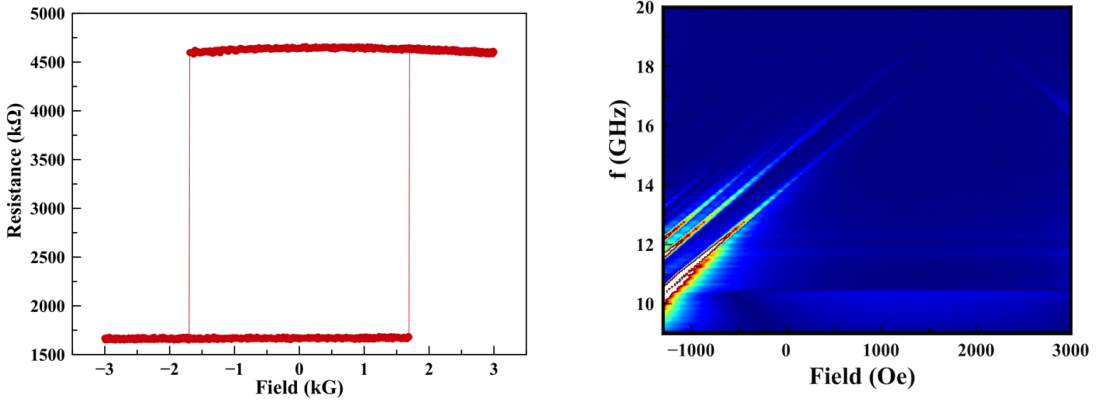


Figure 3.26: (a) The magnetoresistive curve of the studied sample with the TMR ratio around 180 % and the coercive field close to 2 kG. (b) measured ST-FMR 2D spectrum of this device. Three spin-wave modes are visible.

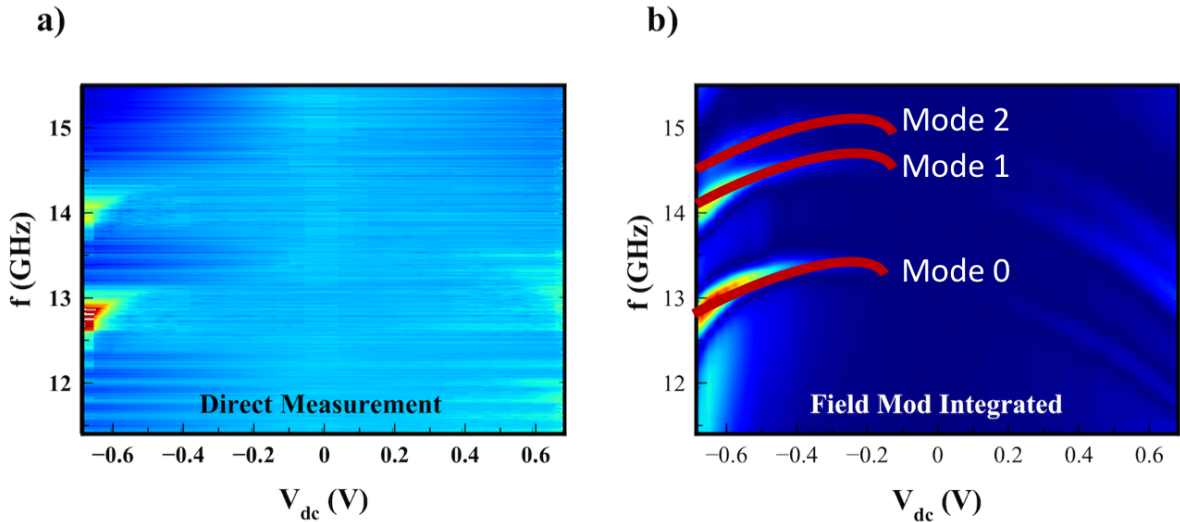


Figure 3.27: (a) Direct measurement of the bias-dependent magnoise measurement. (b) Integration of the raw spectrum under dc-bias. Three spin wave modes are visible as labelled.

frequency on the top panel and the linewidth on the bottom panel. When at the AP state, negative dc bias is the anti-damping spin-torque and can switch the MTJ from the AP state to the P state. There are several observations from the comparisons. First of all, ST-FMR can still measure the data with small(even zero) dc bias while the magnoise measurement is not feasible without large dc bias.

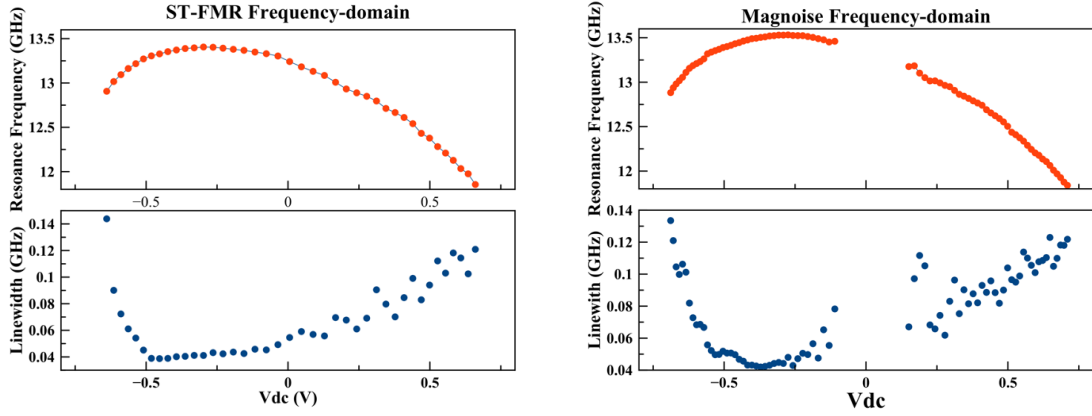


Figure 3.28: (a) ST-FMR data on the frequency domain as a function of dc bias voltage (b) Magnoise data on the frequency domain as a function of dc bias voltage

Secondly, the quantitate value between those two measurements are quite close to each other. This is a important sanity check since the measurement resonance frequency and linewidth should only be determined by intrinsic material properties of the MTJ we studied, not by the experimental methods utilized. For example, the linewidth in both measurement goes to large value when approaching bigger negative dc bias(close to MTJ switching).

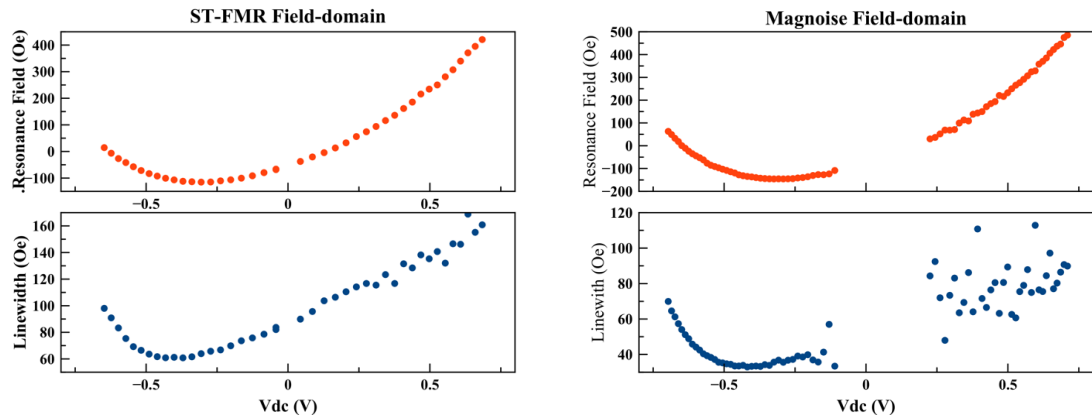


Figure 3.29: (a) ST-FMR data on the field domain as a function of dc bias voltage (b) Magnoise data on the field domain as a function of dc bias voltage

Thirdly, we find that the ST-FMR measurement has better signal-to-noise ratio. It is better expressed in the linewidth measurement under larger positive dc bias where the ST-FMR data

has less fluctuations. To better compare the ST-FMR and the magnoise measurement, we also make field-domain dc-bias using these two methods. Fig.3.29(a) shows the field-domain data from the ST-FMR and Fig.3.29(b) shows the field-domain data from the magnoise noise measurement. The linewidth data shows a considerably larger fluctuations from the magnoise noise measurement at the positive bias current while the ST-FMR still shows a good linear relation.

In summary, the main feature of the magnetic noise method is that it allows measurement of the spin wave spectrum faster than the ST-FMR method. Therefore, this method can be used for rapid screening of magneto-dynamic properties of STT-MRAM cells. However, by compared with the ST-FMR methods in both frequency-domain and field-domain, we find that the ST-FMR usually yields better signal-to-noise ratio spectrum.

3.9 In-plane ST-FMR measurement and Mode identification

While the Spin-torque Ferromagnetic Resonance(ST-FMR) technique is a powerful tool of detecting the spin-wave eigenmodes within the free layer of the Magnetic Tunnel Junctions(MTJs), one needs to be careful about the "modes" excited in the experimental spectrum. There are two main concerns here. First of all, it is important to excite all the spin wave modes of the free layer, from the lowest-frequency quasi-uniform mode to higher modes. Due to different excitation mechanism, either the quasi-uniform mode or some of the higher order modes are possible to be weak in the ST-FMR signal. Mislabelling the modes makes further analysis impossible. Furthermore, as we have seen from the previous chapter, exchange coupling between the free layer and the SAF layer, if not dominant, does exist within the MTJs. Most of the time, we are mainly interested in the free layer dynamic properties and we do not wish to have SAF layer modes mixed with the free layer modes. These two problems are better explained in the following example.

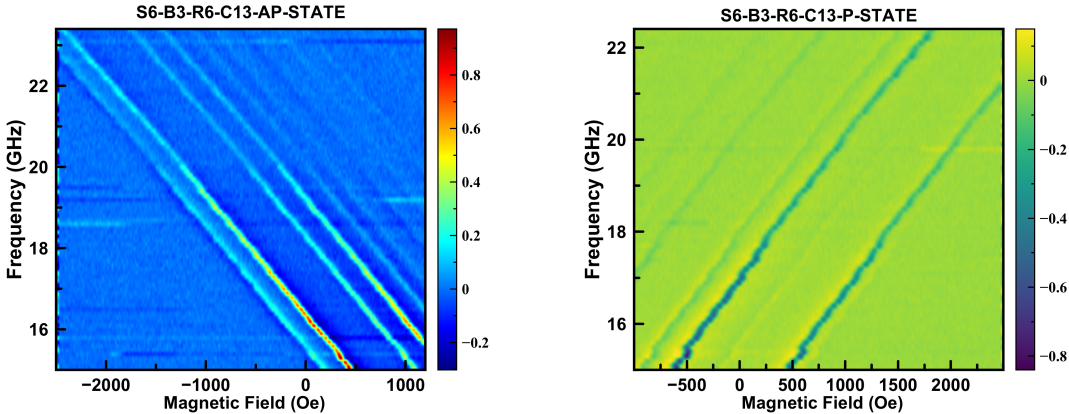


Figure 3.30: 2D contour plot of ST-FMR spectrum taken at AP state(left) and P state(right). Both AP and P state has four lowest obvious spin-wave modes but with different mode spacings.

When we have a big MTJ device and the density of spin-wave modes is large due to later confinement, it is more difficult to identify all the modes excited in the spectrum. Fig.3.30(a) shows a ST-FMR 2D contour plot of a $120 * 60\text{nm}^2$ device. At least we can identify four obvious spin-wave modes from this spectrum with lowest two modes very close to each other. If we focus on one constant-field vertical line, we can see the first mode and the second mode are very close to each other while the amplitude of the first mode is much smaller than the second one. If we look at the 2D ST-FMR contour plot at the parallel state shown in the Fig.3.30(b), it would not make the spin-wave modes identification easier. At the parallel state we also have identified four spin-wave modes with a decent larger gap between the first mode and the second. However we know that the mode spacings are determined by the exchange stiffness of the free layer and there should not be such a obvious difference between the AP and P state. There are generally(which is not necessarily present in the current case) two problems when measuring the MTJ at the parallel state. First of all, the ST-FMR signal is proportional to the absolute value of resistance oscillations under the ac current drive, which is less dominant in the parallel state. This means the parallel state has less signal amplitude compared with the AP state, especially for the quasi-uniform mode. Another problem is that, at the parallel state, since the SAF top layer is parallel to the free layer, it might be possible to excite the SAF modes close to the free layer mode.

The first type of measurements we can make to ensure we excite the free layer spin-wave modes only is to perform DC bias-dependent ST-FMR for both AP and P state. Because of the different spin torque polarity, the free layer and the SAF layer modes should have different curvature when applying the non-zero finite bias current. As we discussed in the previous section, the study of the linewidth as a function of dc bias can also be utilized to fit for the critical voltage of the MTJs. In Fig.3.31(a) and Fig.3.31(b) we have the bias dependent ST-FMR scan at the fix frequency 16 GHz for both AP and P state. What we find is that all the modes we observed at the previous ST-FMR 2D field dispersion contour

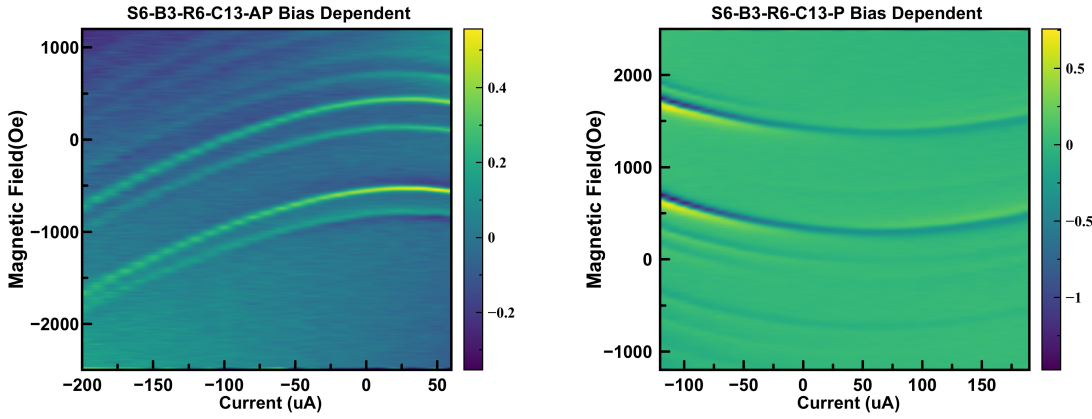


Figure 3.31: Bias dependent ST-FMR spectrum taken at the constant driven frequency 16 GHz for both AP state(left) and P state(right). All the spin-wave modes have the same curvature versus bias.

plot have shown the same curvature under finite bias. This curvature is often determined by the combination of the voltage-controlled magnetic anisotropy and ohmic heating effect.

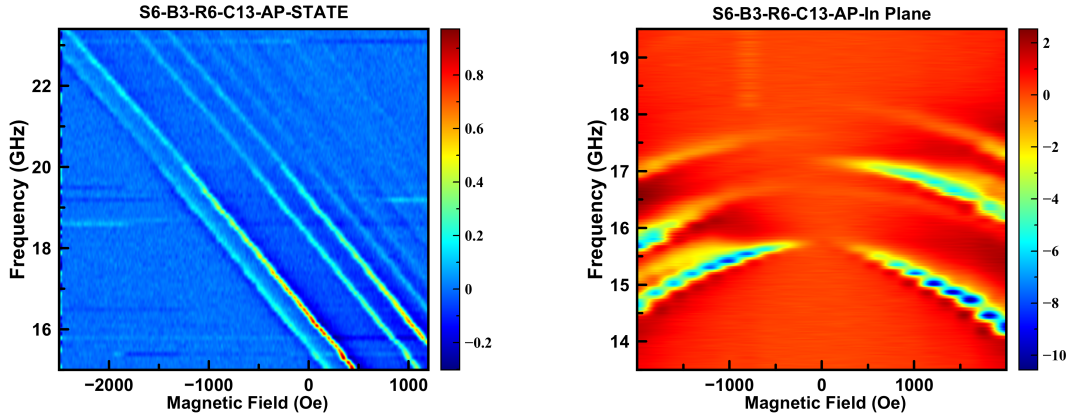


Figure 3.32: 2D contour plot of ST-FMR spectrum taken at AP state with out-of-plane field applied(left) and in-plane field(right). Both spectrum has four lowest spin-wave modes with different relative amplitude.

So far we can conclude that all the spin-wave modes we saw in the out-of-plane ST-FMR measurements are from the free layer. Now we need to identify all the modes without missing some of the modes. We then perform ST-FMR measurement applying the in-plane magnetic field. When we apply the in-plane magnetic field to this MTJ with perpendicular

magnetic anisotropy, we will create misalignment between the free layer and the fixed layer by introducing the hard axis magnetic field. From the Fig.3.32(b) we see such a 2D spectrum with in-plane magnetic field applied at the AP state. In this measurement, the quasi-uniform mode has the largest amplitude compared with other modes due to introduced misalignment. It is also clear that the amplitude of the quasi-uniform mode decrease as the magnetic field decrease. When approaching zero magnetic field, the uniform mode almost becomes invisible. This also help us understand why under perpendicular magnetic field, the main mode is hard to excite. In the next step, we can fit for the modes we excited in the in-plane spectrum and compare with the out-of-plane data. Here for better comparison, we also show the out-of-plane spectrum for the AP state in the Fig.3.32(a). From both the spectrum we can at lease identify four spin-wave modes and we can fit four of them at zero magnetic field(out-of-plane or in-plane).

Experiment	Out-of-Plane	In-Plane
Mode 0 (GHz)	15.63	15.42
Mode 1 (GHz)	16.33	16.23
Mode 2 (GHz)	18.28	18.28
Mode 3 (GHz)	19.22	19.12

Table 3.2: Comparisons between four lowest spin-wave modes at AP state at zero magnetic field with different magnetic field direction(easy-axis out-of-plane and hard-axis in-plane) applied.

The table 3.2 summarizes the mode fitting results. Within certain deviations, it can be seen from the above results that we have good agreements between out-of-plane and in-plane measurements. Moreover, since in-plane hard-axis measurements are able to excite all the spin-wave modes, we can now be confident about our out-of-plane measurement without missing the free layer modes.

3.10 Angular Dependence ST-FMR Measurement

As we have mentioned earlier, ST-FMR measurement at the easy axis is important due to its simplicity in the physics model. In reality, however, the ST-FMR signal at the exact easy axis is usually small. Moreover, firstly, to achieve higher thermal stability, high perpendicular magnetic anisotropy is preferred in the current designs of the MTJs. Secondly, higher resistances of the MTJs is desired for the impedance mismatching. These two factors are negative for improving the ST-FMR signals. So if we can introduce a small angle misalignment to improve the signal without distorting the easy axis nature, that would be of great value for this ST-FMR technique.

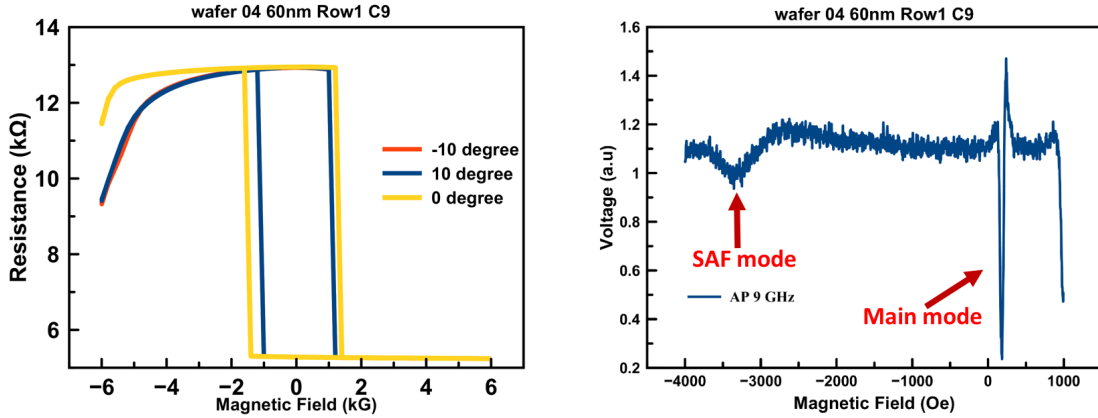


Figure 3.33: (a) Resistance versus Magnetic Field for different magnetic field angles with respect to the sample normal. (b) Example ST-FMR spectrum at 9 GHz for AP state.

The MTJs devices employed in this angular-dependence has relatively simply stack structures to yield less complex ST-FMR spectrum. Fig.3.33(a) shows the resistance versus Magnetic Field for different magnetic field angles with respect to the sample normal. The Anti Parallel(AP) state has resistance around 12910 Ohms with the Parallel(P) state resistance around 5289 Ohms. The TMR ratio is about 140 percent. Fig.3.33(b) shows the example ST-FMR spectrum at 9 GHz for AP state. The peak around zero magnetic magnetic field is the free layer main mode. Above -5 kG, the SAF layer starts to flop and the resistance of the MTJ

starts to decrease. From our previous experience, ST-FMR data above this region is harder to interpret.

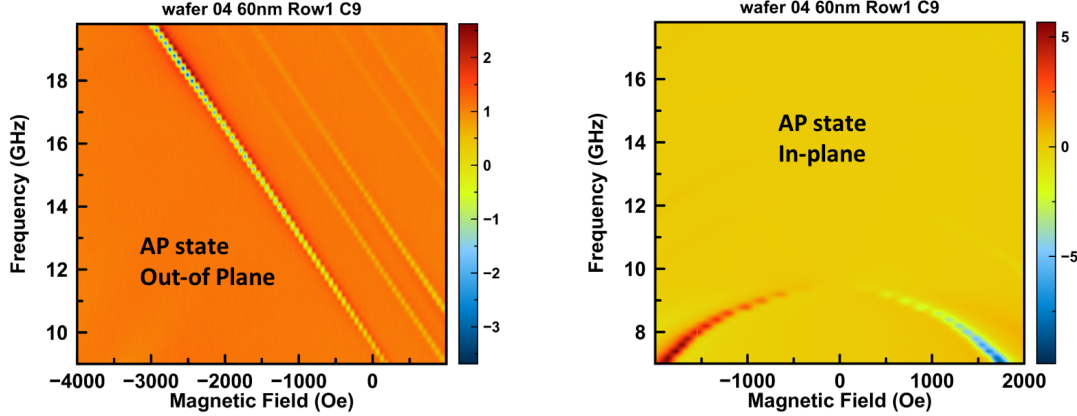


Figure 3.34: (a) ST-FMR 2D contour plot at AP state with field applied perpendicular to the MTJ. (b) ST-FMR 2D contour plot at AP state with field applied parallel to the MTJ.

Fig.3.34(a) shows the ST-FMR 2D contour plot at AP state with field applied perpendicular to the MTJ. We can mainly identify three free layer modes with the lowest main mode has the largest amplitude. The main mode zero field is around 9.58 GHz. Fig.3.34(b) shows the ST-FMR 2D contour plot at AP state with field applied parallel to the MTJ. When applying in-plane magnetic field, only the main mode has been clearly excited and its amplitude increases with increasing in-plane field. The main mode position is around 9.6 GHz, which is close to the out-of-plane data.

Fig.3.35(a) shows the resonance field versus resonance frequency at AP state. For this easy axis geometry, we have a clear linear relation as expected from the Kittel equation. From the fitting we can get the effective anisotropy around 2.8 kOe. Fig.3.35(b) shows HWHM Linewidth versus resonance frequency (lower scale) and magnetic field (upper scale). From 10 GHz to 25 GHz, we have a clear linear dependence of linewidth versus driven frequency, which is consistent with the theoretical predictions of the Gilbert damping. Above -5 kOe, as we see from Fig.3.33(a), the SAF layers become unstable and the linewidth is fluctuating.

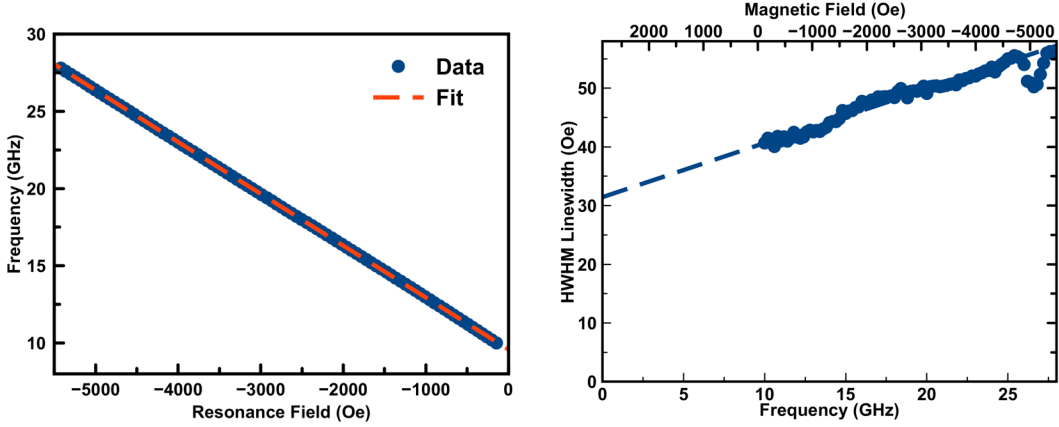


Figure 3.35: (a) Resonance field versus resonance frequency at AP state. (b) HWHM Linewidth versus resonance frequency (lower scale) and magnetic field (upper scale).

We can limit our fitting region from 10 GHz to 25 GHz and fit the data with a line. The slope gives damping constant 0.0031 with the intercept at zero frequency around 31 Oe.

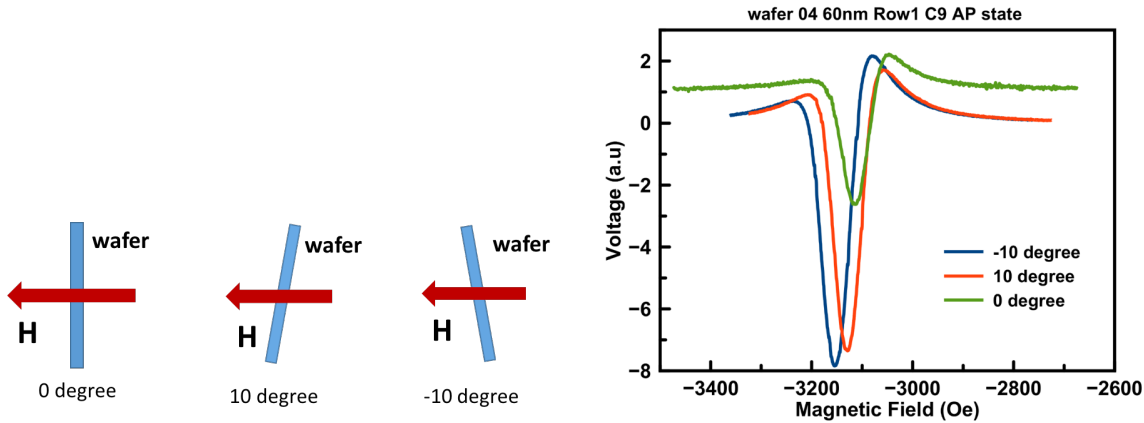


Figure 3.36: (a) Sketches of different angles notations. (b) Example ST-FMR spectrum at 20 GHz for three angles.

So far the magnetic field has been applied exactly perpendicular to the wafer. In the next step, we slightly tilt the wafer so that we can apply the magnetic field off the normal. Fig.3.36(a) shows the sketches of different angles we have applied. By applying these small angles, we are introducing small misalignments of the magnetizations to improve the ST-FMR signal. Fig.3.36(b) shows the example ST-FMR spectrum at 20 GHz for three angles.

By tilting the wafer with small angles, we can at least have 2 times better signal with smaller noise.

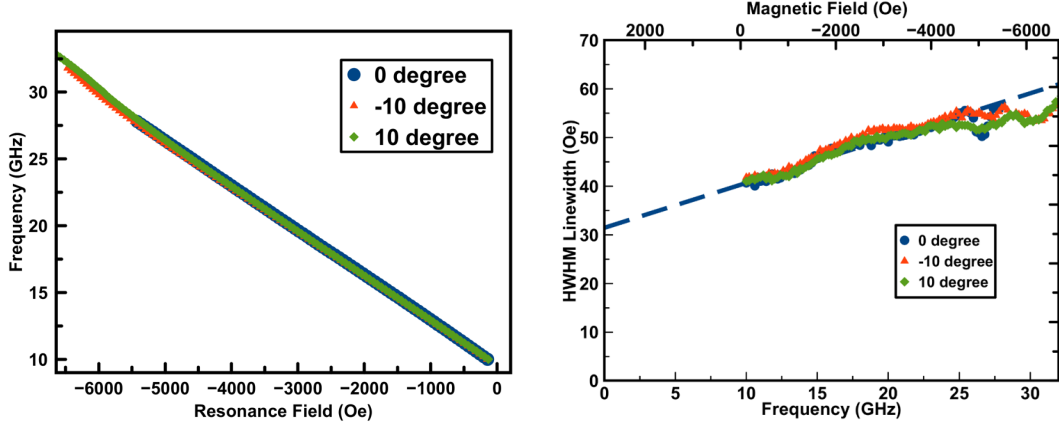


Figure 3.37: (a) Resonance field plotted versus resonance frequency at AP state for different angles. (b) HWHM Linewidth plotted versus resonance frequency at AP state for different angles.

However, would the small tilting affect the mode frequencies and, more importantly, the linewidth of the free layer mode. Fig.3.37(a) shows the resonance field plotted versus resonance frequency at AP state for different angles. We can see that the three groups of data are almost identical. The only region that shows deviations is above -5 kG, where the SAF layers start to become unstable. Fig.3.37(b) shows the HWHM Linewidth plotted versus resonance frequency at AP state for different angles. In the linear region, we can see that the linewidth does not depend on the small angles we applied.

Now we can move the P state measurement. One of the advantage of measuring at the P state is that the SAF layers are more stable and we do no have to worry about the SAF flopping. However, the P state usually has much less signal than the AP state. Fig.3.38(a) shows the resistance versus Magnetic Field for P state up to 9 kG. We can see that the resistance decreases with increasing field, which means the free layer is not fully saturated parallel to the SAF layers. Fig.3.38(b) shows the ST-FMR 2D contour plot at P state with field applied perpendicular to the MTJ. We can also mainly identify three free layer modes.

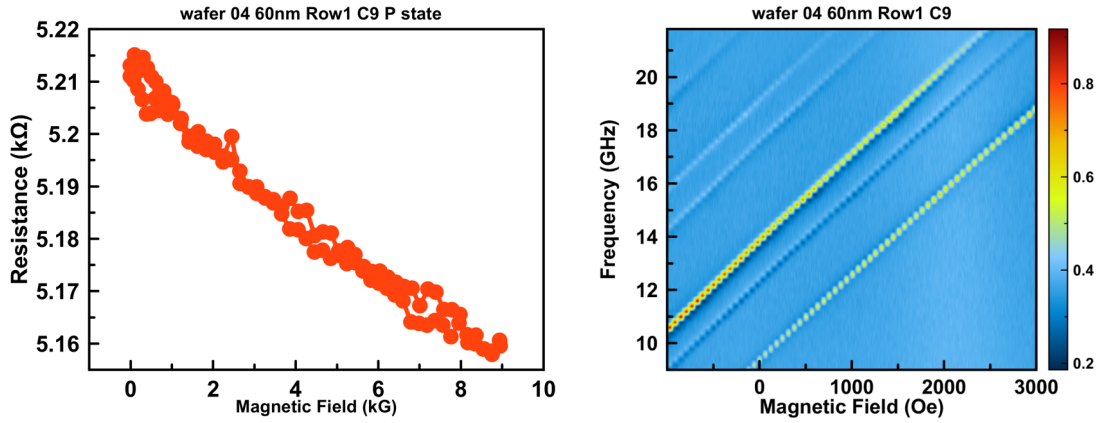


Figure 3.38: (a) Resistance versus Magnetic Field for P state. (b) ST-FMR 2D contour plot at P state with field applied perpendicular to the MTJ.

Compared with AP state, the P state main mode has smaller amplitude with other spin wave modes.

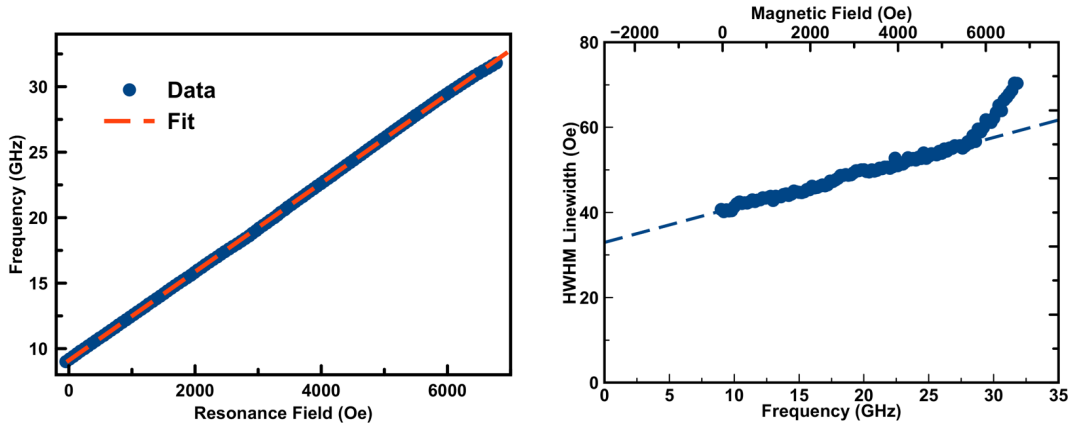


Figure 3.39: (a) Resonance field plotted versus resonance frequency at P state. (b) HWHM Linewidth plotted versus resonance frequency (lower scale) and magnetic field (upper scale).

Fig.3.39(a) shows the resonance field plotted versus resonance frequency at P state. Besides from the linear relations at lower magnetic field, we can see a small deviation from linearity at higher field due to the SAF instability. The effective Anisotropy fitted is around 2.7 kOe, which is very close to the AP state fitting. Fig.3.39(b) gives the HWHM Linewidth plotted versus resonance frequency (lower scale) and magnetic field (upper scale). From 10 GHz to

28 GHz, the linewidth is linearly dependent on the driven frequency. The fitting gives slope 0.0028 and intercept 32.95 Oe. Above 28 GHz, there is a kink of the linewidth data, which is due to the SAF instability.

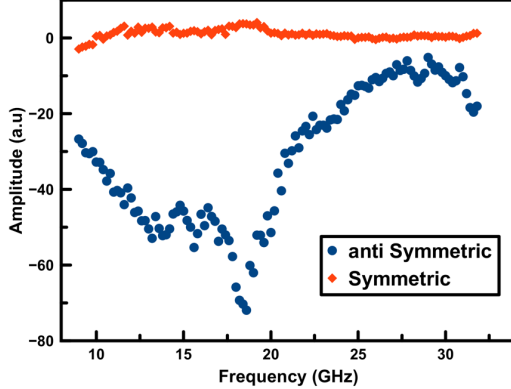


Figure 3.40: ST-FMR signal (symmetric and anti-symmetric components) plotted versus resonance frequency

To learn more about the kink around 28 GHz, we plot the ST-FMR signal (symmetric and anti-symmetric components) plotted versus resonance frequency as showing in Fig.3.40(a). This data is measured at the perpendicular angle and the other two angles have similar dependence. The anti-symmetric component of ST-FMR dominates (typically associated with field-like torque or VCMA). The signal amplitude increases from 10 GHz to 18 GHz and decrease from 18 GHz to 28 GHz. The origin of the initial increase of the signal is not clear and it looks like the interfacial spins are not saturated and collinear. The second kink at 28 GHz is likely to be due to the SAF layer instability at higher magnetic field

Since the P state has smaller ST-FMR signals, it is more important to introduce small misalignment for P state. Fig.3.41(a) shows the example ST-FMR spectrum at 20 GHz for three angles at P state. Again by introducing the tilting, we can improve the signal by at least 2 times. Another thing worth notice is the asymmetry between plus and minus 10 degree. Fig.3.41(b) shows resonance field plotted versus resonance frequency at P state for different angles. We can find that for P state, the resonance field also does not depend on

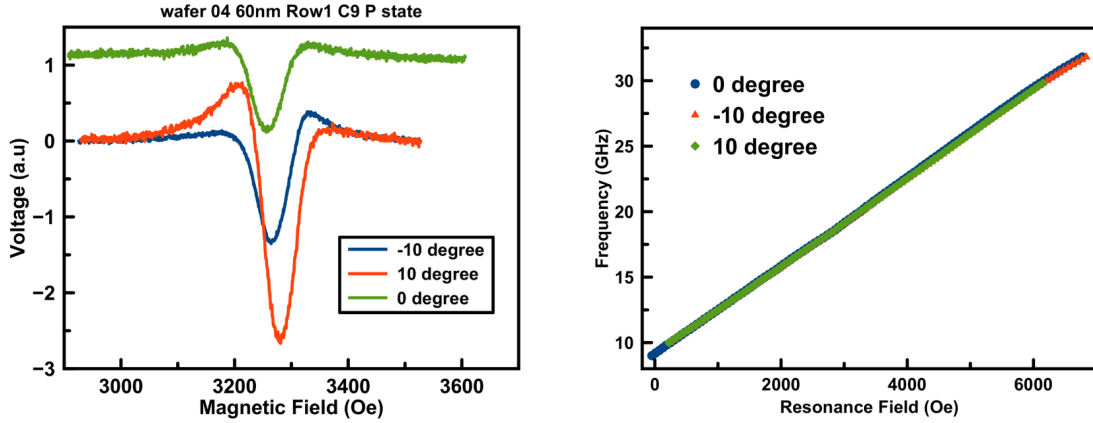


Figure 3.41: (a) Example ST-FMR spectrum at 20 GHz for three angles at P state. (b) Resonance field plotted versus resonance frequency at P state for different angles.

the angles. Fig.3.42(a) shows HWHM Linewidth plotted versus resonance frequency at P state for different angles. The linewidth also does not depend on the small misalignment angle. We also find similar behavior of Linewidth vs field for all three angles with a kink near 28 GHz.

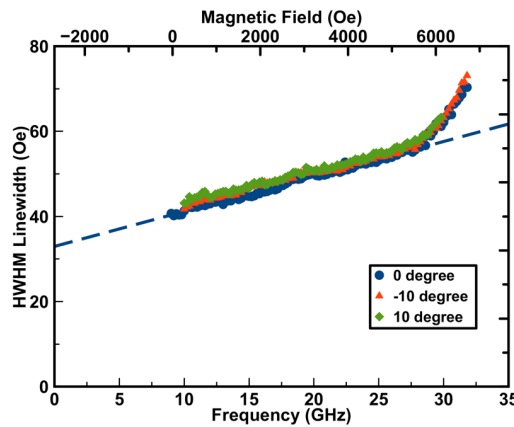


Figure 3.42: HWHM Linewidth plotted versus resonance frequency at P state for different angles

We have measured devices with other sizes and have reached the same conclusion that introducing small angle misalignment is not affecting the linewidth fitting and can greatly improve the signal-to-noise ratio of the ST-FMR measurement.

Chapter 4

Time-domain measurement of spin-torque switching in MTJs

As we have discussed in the previous chapter, magnetization switchin induced by spin-tranfer torque is both useful for understanding the fundamental physics of magnetic dynamics and for applications in magnetic random access memory(MRAM). Measurements in the time domain can provide the most direct information about the switching process. However, the majority of previous time-resolved studies of spin-torque switching required averaging over many events, which would hide individual switching variations. Here we report a single-shot time resolved time-domain measurement similar to the technique developed by Cui.et.al [75]. We have shown that the sensitivity of single-shot resistant measurements have been greatly improved and both prior to switching and during spin-torque switching have been resolved.

4.1 Experimental Setup

Previously, the sketch of time-domain measurement is shown^{4.1}. The general idea is the following: by send the pulse into the magnetic tunnel junctions, the transmitted the signal will depend on the resistance of the device.

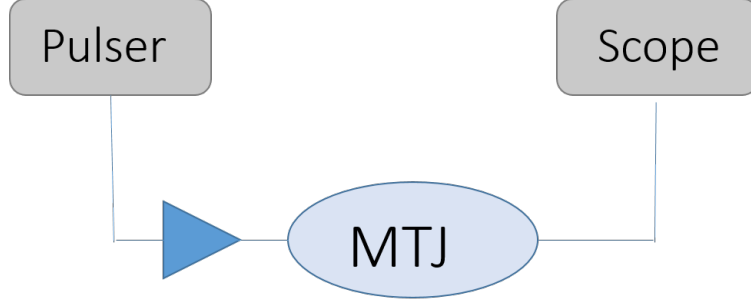


Figure 4.1: Original time-domain setup

If there is magnetic state switching happening during the duration of this pulse, we could be able to resolve it by recording the time-domain signal using a Time scope. This method is very straightforward, however, it is not practical in most cases. To illustrate that, let us calculate the transmitted signal. If we apply the voltage pulse V_{inc} , the transmitted signal will be given as

$$V(t) = \frac{V_{inc}}{1 + G_S(t)Z_0/2} \quad (4.1)$$

where $G_S(t) = 1/R_S(T)$ is the sample conductance(the reciprocal resistance), $Z_0 = 50\Omega$ is the probe impedance. Typically the resistance of the devices is around several thousands ohms, so we have a very strong impedance mismatching here. We can expand the time-dependent voltage signal with respect to a reference, if we use the parallel state conductance G_P as the reference value, and write $G_S(t)$ as $G_S(t) = G_P + \Delta G(t)$, since $\Delta G(t)Z_0$ is usually

much less than 1, we can expand Equation 4.1 as the following:

$$V(t) = \frac{1}{1 + G_P Z_0/2} V_{inc} + \frac{Z_0/2}{(1 + G_P Z_0/2)^2} V_{inc} \Delta G(t) \quad (4.2)$$

The first term in Equation 4.2 is related to the resistance mismatch between the device and RF probe. The second term is coming from the resistance change associated with magnetic dynamics. If we would like to monitor the device resistance, we should expect the second term to be large, at least well above the noise level. However, as we point out, because of the impedance mismatching, the second term would be really smaller, usually around several mill volts. This requires lots of averaging to improve the signal to noise ratio and thereby hide each single switching event.

To improve our signal to noise ratio, we adapt improved measurement set-up shown in Fig. 4.2. As usual, we apply the pulse from a pulse generator. This time, however, we split the into two identical copies. The first copy goes into the device and induce magnetic switching. The second pulse will go through a pulse inverter and it will flip the polarity. What is important here is to choose the pulse inverter so that it does not distort the waveform too much. After the first copy goes through the device, we use a power combiner to combine these two pulses in a way that these two copies should enter the power combiner at the same time.

To accomplish that, we would like to carefully tune the time delay of there two lines so that they have been correctly synchronized. In the current set-up, we adjust the time delay by varying the microwave cable length in the circuit. After we combine these two pulses, we use an amplifier to amplify the signal and send it into the storage scope. In this process, the signal left after we combine these two pulses would only be the part depending on the magnetic state, where any other type of noise should be canceled out. This should greatly improve the signal-to-noise ratio.

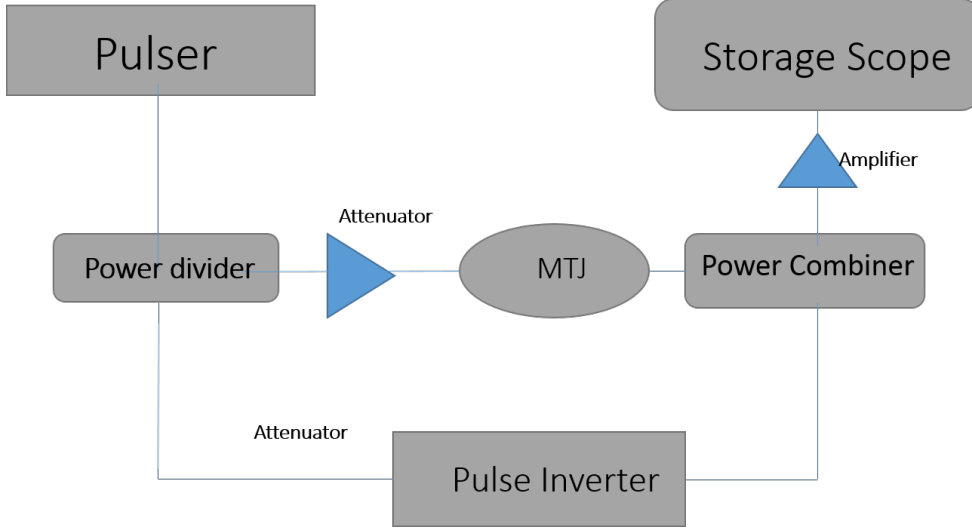


Figure 4.2: Improve time-domain set-up

Before we go to the experiment discussion, we would like to discuss another important source of noises in these type of experiments. Ideally, we want to amplify our voltage signal after the power combiner to be large enough. However, we also have to fight with the bit noise induced by the storage scope. We are using a 64-bit time scope, the bit noise in the measurement is proportional to the voltage resolution used in the time scope. So in order to reduce the bit noise, smaller voltage resolution should be adapted and the signal has to be small enough to fit in this small voltage resolution. Practically, after we amplify the voltage signal, we use proper attenuator(usually around -10 dB).

4.2 Results and Discussion

Now we have set-up correct time delay and pick appropriate attenuation in the circuit, we can send the pulse and observe the time dependent signal. Fig.4.3 shows a typical signal we resolve from a switching. We first initialize the MTJ into anti-parallel state and send through a positive pulse. The polarity of positive pulse corresponds to damping for the anti-parallel

state, so this positive pulse should not induce magnetic switching for anti-parallel state. We record the anti-parallel state signal as the background and label it as AP in Fig.4.3.

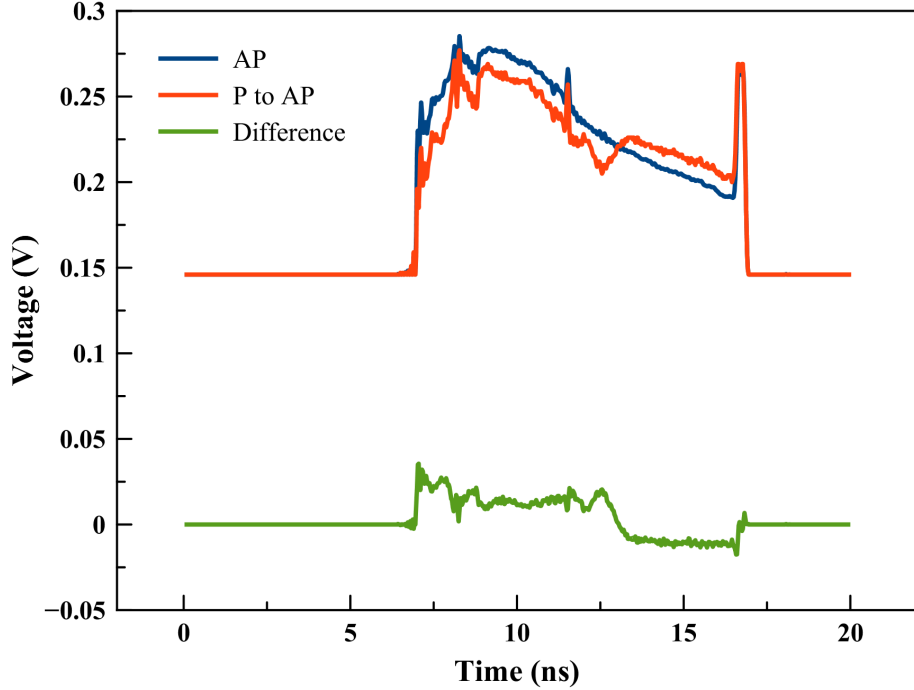


Figure 4.3: A switching signal from time-domain measurement. Anti-parallel signal(blue), PtoAP signal(red) along with the voltage difference(Green)

Then, we initialize the MTJ into parallel state and re-send the positive voltage(which is anti-damping for parallel state). Then we record this signal from the time scope and label as P to AP in Fig.4.4(a). One can clearly find that at the beginning of the pulse, AP and PtoAP signal are clearly separated. At the middle of the pulse, the PtoAP pulse suddenly shifts into AP signal, which is related to the magnetic state change in the MTJ. So we have observe a magnetic switching in time-domain. We can also subtract the background AP signal from the PtoAP and plot it labeled as Difference in Fig.4.4(b). If we look at the Difference signal, we can see that at the beginning of the pulse, the difference is around 30 mV, then it drops to - 10 mV. So we can well separate the anti-parallel and parallel state.

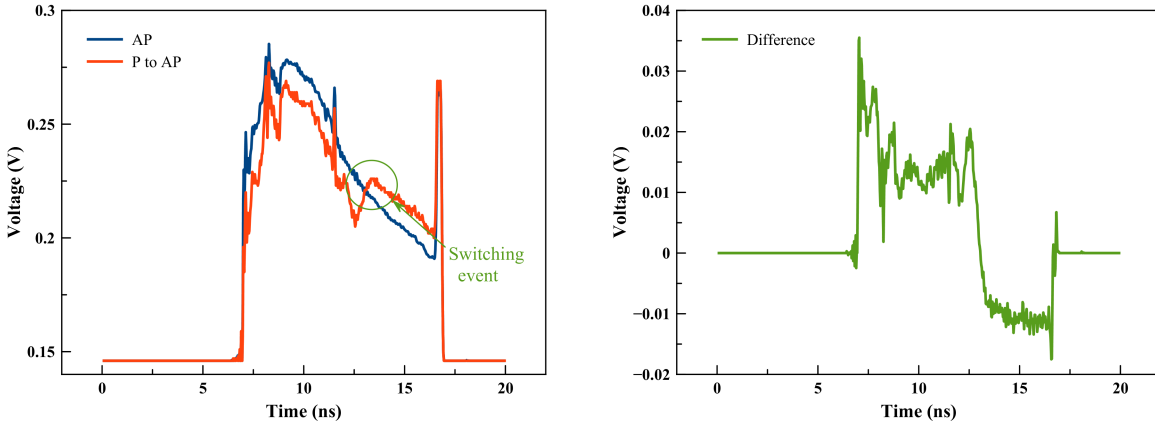


Figure 4.4: (a) Zoomed PtoAP signal(red) and AP state background(blue) (b)Zoomed voltage signal difference.

Now that we have greatly improved the voltage signal to separate two magnetic states, we can study individual switching event without perform averaging to reduce the noise. One thing we can study is the distribution of switching time. From Fig.4.5(a) to Fig.4.5(c) we show several traces from different switching events. Here we only demonstrate the different signals between two state. One can clear find that for different switching traces, we have different switching time, ranging from 2.6 ns, which is at the beginning of the pulse, to 9 ns, which is at the very end of the pulse. This indicates the random nature of this single shot-switching. More importantly, we can obtain a good statistics of switching time as a function of input parameters. Also we find that in Fig.4.5(d) we find that at a fixed voltage, we can still have non-successful switching event, where we find that for this non-successful switching attempt, the system enters a large oscillation. This enables us to further study the different between successful and non-successful switching events.

To further illustrate the random nature of magnetic switching in time-domain, we fix the applied voltage at 425 mV and study the distribution of the switching time as it is shown in Fig.4.6. From other switching probability measurement, we already know that at 425 mV voltage, the device has a very switching probability. From this distribution we find that

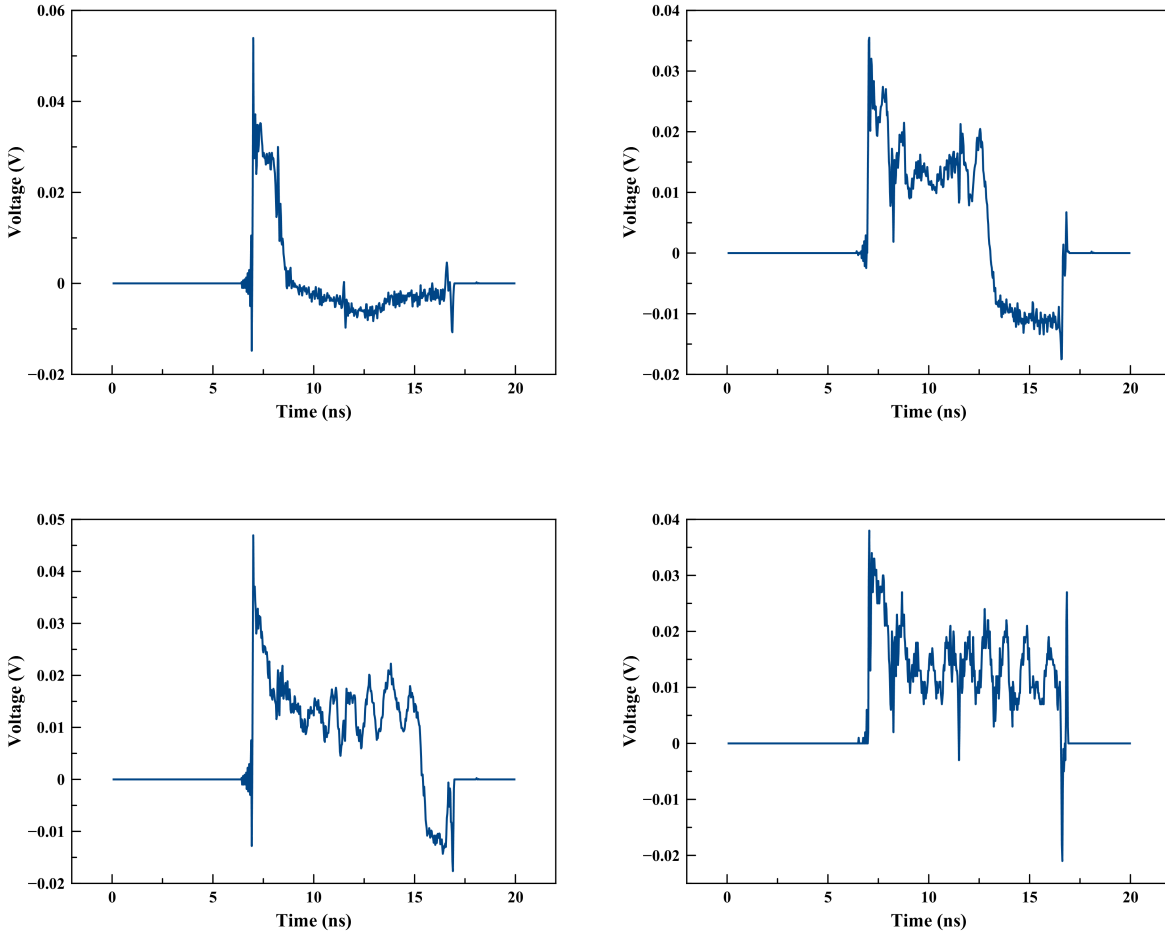


Figure 4.5: Switching events for different individual events.(a)(b)(c) show switching events which switch at 2.6 ns, 6.7 ns and 9 ns respectively. (d) shows the non-switching event.

the switching time is unevenly distributed, it is centered around 4 ns and has a negative skewness. The distribution also gives a very small tail at high switching time, which means switching rarely happens at the tail of the pulse. We try to fit the switching count as a Gaussian function, which gives a good fitting result as it is shown in Fig.4.6.

If we vary the applied voltage and also measure the switching time distribution as Fig.4.6, we typically find that the the peak of the distribution and also the skewness are dependent on the applied voltage. For smaller applied voltage, the center of the switching time moves to higher time period and the skewness of the distribution becomes smaller. That indicates

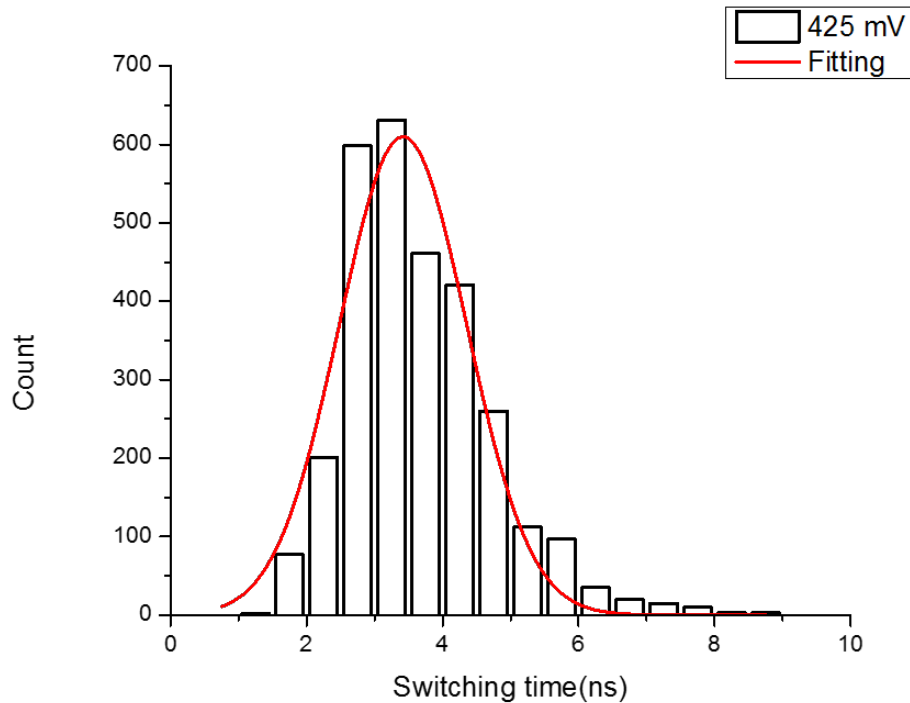


Figure 4.6: Distribution of switching time at constant voltage 425 mV.

that for larger voltage we have more deterministic and fast switching. When the applied voltage is small and the switching probability is low, the switching behavior shows more randomness.

Chapter 5

Write Error Rate measurement

In order to make magnetic tunnel junctions as the cell for future Magnetic Random Access memory, it is important to characterize the switching property for MTJs, which setting the MTJs to a desired state(write). This measurement is known as the Write Error Rate(WER). Formally, applying the electric pulse at different duration and amplitude, by monitoring the resistance before and after the pulse, we can find the switching probability. For optimizing the WER, we need to consider the power consumption and also the switching time. Moreover, from a fundamental physical point of view, it is important to understand the detailed switching mechanism. In the previous chapter, we have already shown how to observe switching in time-domain.

The Write Error Rate(WER) is defined as the ratio between number of non-switching attempt with the total switching attempt. So WER can be understood as the probability of not successful attempt. The typical error used in common computer memory is around 10^{-9} . Therefore, in order to reliably characterize the WER, we need to obtain very large statistics, which is only increasing by taking into account the approximately \sqrt{N} counting error associated with the binary results of a switching attempt. It would take years by employing

conventional DC resistance measurement in this sense. To overcome this, we are going to a quick and accurate measurement of WER with large statistics as a function of certain parameters.

5.1 Experimental Setup

We first show the experiment set-up for write error rate measurement^{5.1}. As we can see, the circuit has been divided into two parts. In the AC part, a Picosecond Pulse Labs 10,0070A pulse generator (PSPL) is used to generate write pulses and an Agilent 33220A Arbitrary Waveform Generator (ARB) provides the reset pulse. We then use a Keithley 2400 source Meter(Keithley) to provide a small DC bias voltage, which will then be National Instruments USB-6251 BNC Digital Acquisition Board (DAQ)

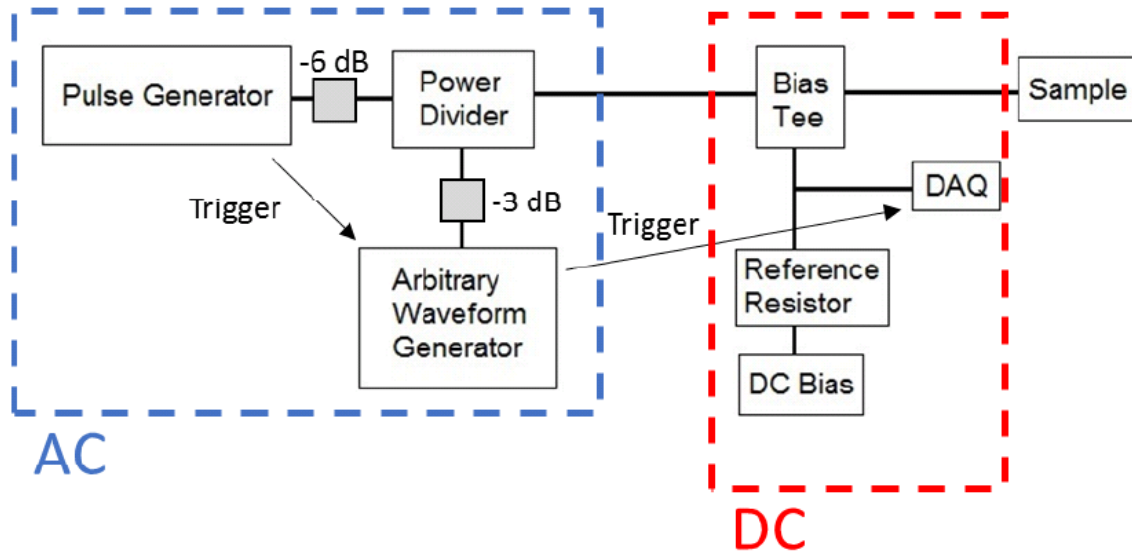


Figure 5.1: Write Error Rate measurement set-up, here we include AC and DC circuit

The PSPL can provide pulses from 100 picoseconds to 10 nanoseconds, while the ARB has a pulse range from 50 nanoseconds to DC. Our goal is to generate a pulse sequence as it is shown in 5.2.

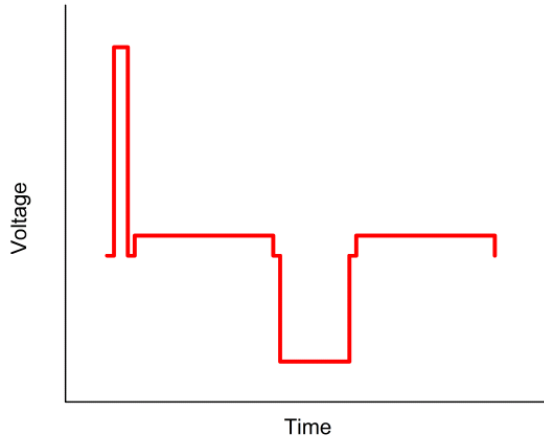


Figure 5.2: Pulse shape used in Write Error Rate Measurement

In order to produce such a pulse sequence, we need to establish correct synchronization. To do that, the following procedure has been carried out:

1. Connect the trigger output of the PSPL to the trigger input of the ARB. This port of the ARB is labeled Ext. Trig., which is located on the rear panel.
2. Set the PSPL trigger method to Internal with a repetition rate appropriate for the length of pulse train used (for the work presented in this thesis, 2.5 kHz was used). Now the PSPL is used to control the remaining instruments
3. Set the ARB trigger to Ext. Trig. (rising edge) and the output mode to Burst. This will allow the ARB to generate a burst of pulse sequence once triggered.
4. Connect the trigger output of the ARB (labeled Sync) to the trigger input of the DAQ, labeled APFI0 (analog programmable function interface) for the model mentioned above.
5. Set the DAQ trigger to APFI0 and the sampling rate to maximum (1.25 MSamples/s in the case of this DAQ)
6. Connect a reference resistor to the DC bias and then connect it to the DC port of the bias tee. Usually this reference resistor should have resistance in the middle of parallel and

anti-parallel state. The DC bias should have constant output and is chosen to have a polarity to favor the switched state.

7. Connect an analog input of the DAQ (any will do) between the reference resistor and the bias tee.

8. Connect the outputs of the PSPL and ARB, with appropriate attenuators to protect the equipment at the hardware level (for the equipment and circuit used here, -6 dB and -3 dB respectively), to the power divider. Then connect the remaining port of the power divider to the AC port of the bias tee. All connection cables used should be rated for the appropriate frequency of the pulses.

The logical behind the experiment setup is explained the following. To measure the switching probability at a fixed pulse, we need to record the resistance before the pulse and after the pulse. Clearly, it would not be practicable to measure the resistance using a Keithley(it would be painfully slow). By inserting a reference resistor between the sample and DC source, the voltage passing through the reference resistor would change according to the sample resistance. By recording the voltage in real time, we can record the resistance of the sample.

Another import aspect of the measurement is to properly reset the state. Of course, using a magnetic field to reset is not acceptable. To accomplish that, we use ARB to generate a opposite pulse as write pulse. To save the sample from electrical breakdown, the reset pulse is usually longer than write pulse and should have relatively low amplitude.

The raw data we get from the automation software such as LabView would be a voltage trace of many switching attempts. Usually LabView is not efficient enough to handle such a great amount of data. So we choose to have LabView to extract two sections of each switch attempt corresponding to the read pulse and write pulse. This method will give us a long

list of initial and final voltages from each switching attempt that can be then translate into resistance and then compare to evaluate the success of each switching attempt.

Given the voltage recorded by the DAQ, we can convert the voltage to resistance of the sample. The DC part of the circuit is a voltage divider, the resistance of the MTJ as a function of the measured DAQ voltage V_{DAQ} is given by

$$R_{\text{MTJ}} = \frac{R_{\text{Ref}} V_{\text{DAQ}}}{V_{\text{DAQ}} - V_{\text{Read}}} \quad (5.1)$$

where R_{Ref} is the value of the reference resistor and V_{Read} is the read voltage. Here the value of V_{Read} should be properly picked. The read voltage should be higher enough to well separate two states, at the same time, higher read voltage would disturb the switching state. To show that, the voltage difference between anti-parallel state and parallel state is the following:

$$\Delta V_{\text{DAQ}} = V_{\text{read}} \frac{(R_{\text{AP}} R_{\text{Ref}} - R_{\text{P}} R_{\text{Ref}})}{(R_{\text{AP}} + R_{\text{Ref}})(R_{\text{P}} - R_{\text{Ref}})} \quad (5.2)$$

where R_{AP} and R_{P} are anti-parallel and parallel resistance of the device. Here we find that the voltage difference is linearly depend on the read voltage.

Now we have to determine an adequate and safe reset voltage and process the raw data output by LabView. One first needs to process some initial data and then optimize based upon the results in an iterative fashion to assess the efficiency of the reset pulse. To analyze the raw data file, a python script carry out the following routine:

1. Read the raw data file and extract all initial and final measured voltage(before and after pulse.)

2. Convert the raw voltage into resistance using Equation 5.2.
3. Determine the device state for each voltage value. This can be done by considering the known parallel and anti-parallel states. Usually, if the read voltage is positive, the AP state should have higher voltage.
4. Compare initial and final voltage for each switching attempt and categorize into three possible cases: switched (the device starts in the correct state and ended in the opposite state), not-switched (the device starts in the correct state and fail to switch), and missed (the device starts at the wrong state.)
5. Sum over all the switching attempt. The write error rate is given as $\frac{N_{NotSwitched}}{N_{Attempts} - N_{missed}}$

To determine the necessary reset voltage, we adapt the following iterative process:

1. Set the write voltage so that most of the switching attempts are successful.
2. Set the reset voltage to a safe and small amount. A good starting point is half of the write voltage.
3. Start the measurement and process the data. Identify the number of missed events, which means the device has not been set properly to the desired initial state.
4. Slowly increase the reset voltage so that the number of missed event is much less than one per cent of the total switching events.

Since the duration of the reset pulses are much longer than write pulses (typical resets pulse duration are 100–500 ns while write pulses are usually smaller than 10 ns). The proper value of reset pulse is very important for this measurement. If the reset pulse is too small, then many of switching attempts would not be used in the final data analysis. If the reset pulse is too large, then we take the risk of device breakdown. Now with our measurement technique explained, we can reliably and efficiently study Write Error Rate as a function of

write pulse and voltage, applied magnetic field or any other interesting parameters. With our experimental set-up, 10^6 switching attempts can be completed in 8.5 minutes.

5.2 Results and Discussion

Detailed switching mechanism by applying the spin transfer torque is still unclear. People have argued that it is possible some sub-area will act as an activation regime which will leads the switching[76]. It is proposed that at finite temperature, switching probability is proportional to applied voltage[77]. However recently people have found anomalous behavior at certain amplitude and polarity[78][79][80]. We would like to test the switching probability measurement on our samples.

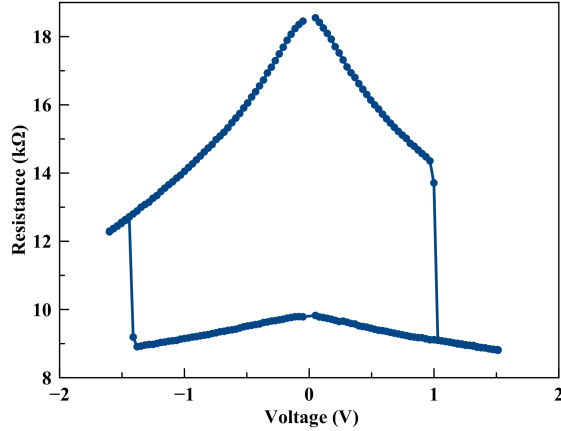


Figure 5.3: Resistance versus dc voltage at zero magnetic field

Before we make Write Error Rate measurement, we need to measure the resistance as a function of dc voltage to identify the switching probablity. Fig.5.3 shows one example of sample resistance as a function of applied dc voltage. At positive polarity, the device starts at high-resistance(anti-parallel)state. The resistance drops with increasing voltage. Around 1 V, the resistance drops to low-resistance(parallel)state and stay at parallel state when the voltage keep increasing. Now if we keep the device to be in the parallel state and start

to apply the negative voltage, around negative 1.5 V, the resistance of the device will go up, which means switching from parallel to anti-parallel. So from this curve we know that by applying the positive voltage pulse, we can switch the device from anti-parallel state to parallel state.

To perform the write error rate measurement, we first initialize the device at the anti-parallel state using magnetic field, then we constantly apply the positive voltage as we discussed in the previous section. Appropriate reset voltage has been chosen to reset the device back into anti-parallel state. In this set-up of measurement we fix the pulse duration to be 10 ns and only varying the pulse amplitude. The result is shown in Fig.5.4

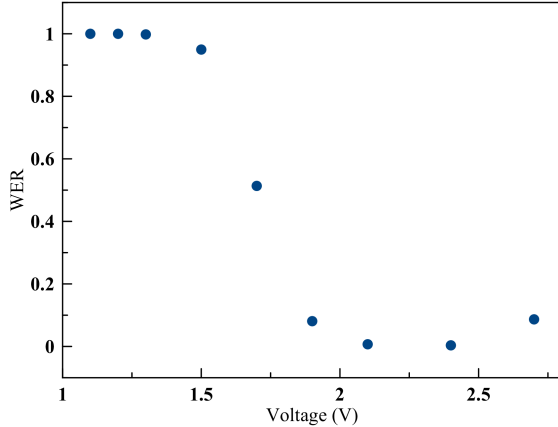


Figure 5.4: Write Error Rate curve for one typical device studied in the experiment.

At low amplitude pulse, the switching probability is indeed very low, close to zero. As we gradually increase the pulse amplitude, around 1.5 V, the device starts to increase and the WER is close to zero at around 2 V applied voltage. So far everything is as expected. However, starting from 2 V when we would normally expect the WER to keep decreasing at increasing applied voltages, we find that however, the WER starts to increase somehow. More formally, from a uniform switching theory, the WER should have Gaussian dependence with respect to voltage at finite temperature[78], so we can call this non-Gaussian behavior to be anomalous WER.

Different mechanism has been proposed to explain the anomalous WER behavior. One possible origin is coming from non-linear coupling between modes excited in MTJs [81][82]. Another suspect is the formation of sub-volume domain in the switching process. Previously, people believe that the switching process is dominate by sub-volume switching[10][76]. However now there is a growing evidence to show that the Dzyaloshinskii-Moriya interaction can significantly affect the switching process and cause the meta-stable state which is unfavorable for switching[83].

Chapter 6

Determination of Exchange Stiffness of STT-MRAM devices with broken symmetry

We have developed one of the world most sensitive spin-torque ferromagnetic resonance(ST-FMR)[64] and we would like to accurately determine the exchange stiffness of the Magnetic Tunnel Junctions. The exchange interaction is essential since it determines the energy scale of two adjacent spins in the magnetic materials. Its value also affect the formation of magnetic structures such as domain walls and vortices. Therefore it is important for both fundamental scientific interest and technology development to measure the exchange stiffness from simple structures such as monolayer superlattices and thin films to complex systems such as the Magnetic Tunnel Junctions(MTJ). It has been demonstrated that the exchange stiffness in in-plane magnetized MTJs can be estimated by measuring the thermal stability factor and fit of model based on nucleation-type magnetization reversal[84] and by modelling from microwave noise spectroscopy[85]. It has also been showed that MTJs with perpendicular magnetic anisotropy can be utilized by characterizing the spin wave dispersion to determine

the exchange stiffness[62][86]. However previous studies involving MTJs are focused on nominal circular devices and only rely on the mode spacings between first higher order modes and quasi-uniform modes. However the symmetry breaking in the nominal circular devices[59],which is often inevitable during the fabrication of the STT-MRAM devices, has altered the spin wave modes. In this chapter we would like to perform a comprehensive review of determining the exchange stiffness on both nominal circular devices and stadium shaped devices with different lateral dimensions.

6.1 Measurement of ST-FMR on nominal circular devices

The experimental set-up is based on Fig.3.1 where we employ the field modulation technique to improve the signal-to-noise ratio. The STT-MRAM devices we measured are CoFeB based Magnetic Tunnel Junctions. We are mainly focused on the field-domain ST-FMR which sweeps the magnetic field at fixed constant driven frequency. We find that the field-domain measurement is usually faster and yields better signal compared with frequency-domain.

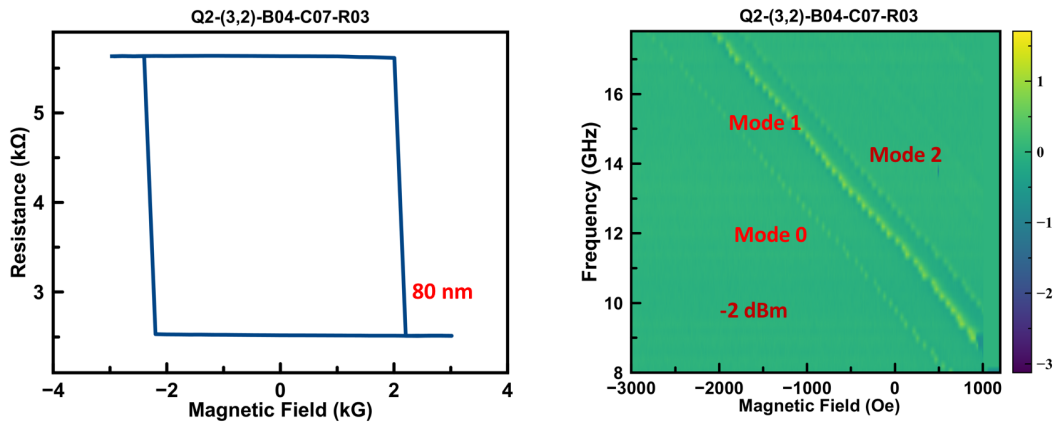


Figure 6.1: (a) Example magnetoresistance of one 80 nm MTJ device (b) 2D contour plot of the ST-FMR signal of this device with -2 dBm power applied at the AP state

We start with nominal circular devices with diameter ranging from 70 nm to 210 nm. Fig.6.1(a) shows an example magnetoresistance of 80 nm MTJ device. This specific device has resistance of 2511 Ohms at the parallel state and 5631 Ohms at the anti-parallel state. The coercive field is about 2100 Oe. Fig.6.1(b) shows the 2D contour plot of the ST-FMR signal of this device with -2 dBm power applied at the AP state. From the 2D contour plot we can mainly identify three of the spin wave modes, each of them labelled on the plot. The lowest mode(Mode 0) is the quasi-uniform main mode of the free layer in the MTJs. Mode 1 and Mode 2 is the split first higher order mode(we will discuss the mode profile in the next section).

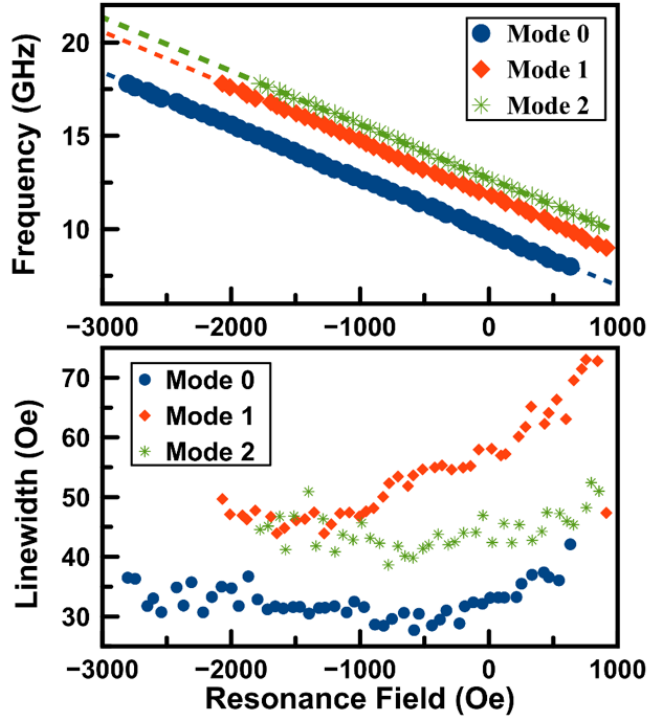


Figure 6.2: Top: the frequency versus resonance field for three lowest modes. Bottom: the HWHM linewidth versus resonance field for all the three modes.

Fig.6.2 summarizes the mode fitting result for all the three modes we excited from this 80 nm device. The top panel shows the frequency versus resonance field for three lowest modes. We can see a linear relation between the driven frequency and the resonance field as

predicted by the Kittel equation. The main mode at zero field is 9.83 GHz and the effective anisotropy field H_k around 3.4 kG. The bottom panel shows the HWHM linewidth versus resonance field for all the three modes. Quite surprisingly, linewidth does not have a strong field dependence from -3000 Oe to 500 Oe (and frequency change by nearly a factor of 4). In theory, the linewidth in the field domain should be given by

$$\Delta H = \alpha \frac{\omega}{\gamma} + \Delta H_0 \quad (6.1)$$

Here, ΔH is the field-domain HWHM linewidth. $\omega = 2\pi f$ is the angular frequency. $\gamma/2\pi$ is the gyromagnetic ratio. Firstly, this non-linear relation reveals that the fundamental understanding of the large non-Gilbert contribution to the damping is lacking. Secondly, we find that the linewidth for this device is relatively small (around 35 Oe). If we use the zero-field linewidth as upper bound, we have an estimation of Gilbert damping around 0.01.

So far we have demonstrated that by performing the ST-FMR measurements, we can determine the "resonance frequency" at zero magnetic field for all the modes excited in the experiment. The frequency of the main mode can be used to determine the effective anisotropy field and the mode spacings between the main mode and the higher order mode is related with the exchange stiffness of the free layer. Before we move to the exchange stiffness, let us first discuss the origin of the ST-FMR signal in this perpendicular magnetized MTJs.

6.2 Summary of Circular Devices: Experimental Data

Now we would like to summarize the experimental data of circular devices with different diameters. As we have demonstrated in Fig.6.1(b), the signature of the spin wave modes excited in these devices are one lowest quasi-uniform main mode(Mode 0) with two split higher-order modes(Mode 1 Mode 2). For each dimension, we can measure over ten devices to obtain mode statistics. The idea of measuring nominally identical devices is to reduce random sample-to-sample variations. For each measured device, we can list the frequencies of three spin-wave modes at zero magnetic field. These raw data can be found from the appendix. From the mode statistics we can extract the average mode frequency and standard deviations.

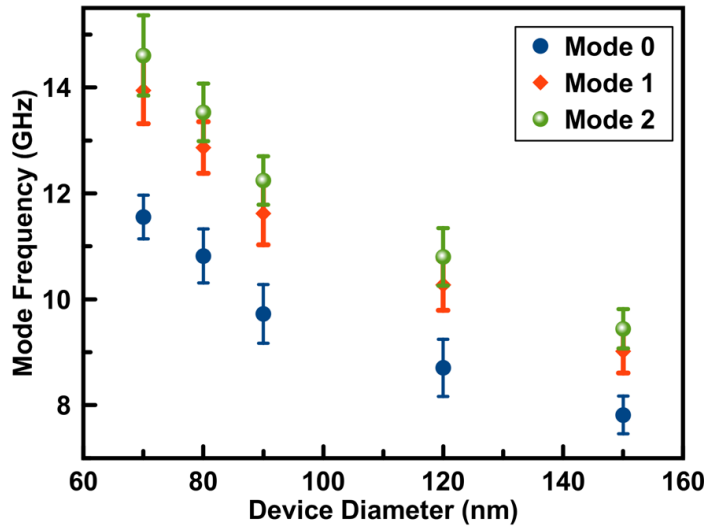


Figure 6.3: Summary of main mode of all the three modes. The error bar indicates the standard deviations obtained from sample statistics.

The summary of main mode and standard deviations of all the three modes are plotted in Fig.6.3. As the device diameter goes up, the mode frequencies of three modes reduces due to shape anisotropy reduction.

Now let us first focus on the main mode and plot it as a function of device diameter as shown in Fig.6.4(a). The effective demagnetization factor is given by[87].

$$N_z \approx 1 - \frac{1}{\pi d} [2 \ln(4 \frac{d}{t}) - 1] \quad (6.2)$$

where the d is the device diameter and t is the free layer thickness. From Eq.6.2 and the fact that $N_x + N_y + N_z = 1$, the total perpendicular anisotropy H_{ku} can be written as[51]

$$H_k = H_{ku} + 2\pi(1 - 3N_z)M_s \quad (6.3)$$

Assuming the free layer thickness 1.6 nm, the fitted result M_s 1820 emu/cm³ and H_{ku} 24 KOe, which is comparably with other independent measured values.

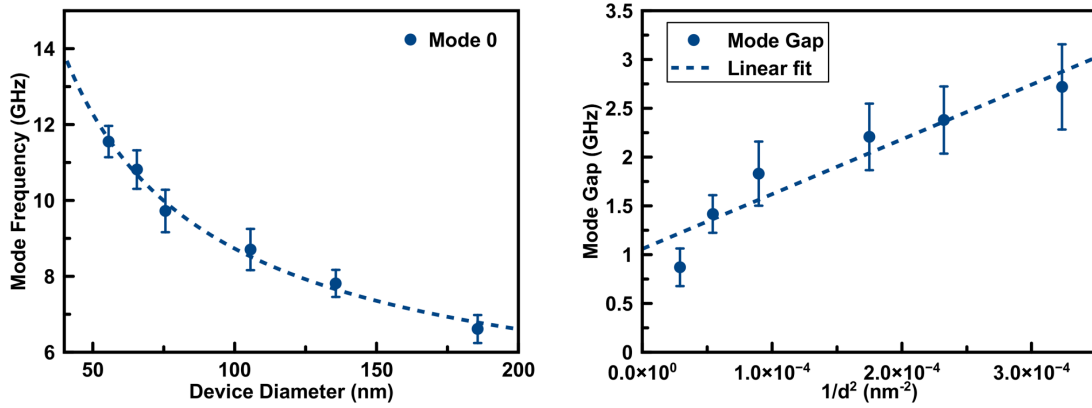


Figure 6.4: (a) Main mode frequency is plotted as a function of device diameter. (b) Mode Gap plotted as a function $1/d^2$ with d represents the diameter of the device.

Fig.6.4(b) shows mode gap plotted as a function $1/d^2$ with d represents the diameter of the device. The mode gap between first two modes in a circular device can be modeled as

$$\hbar(\omega_1 - \omega_0) = D(s/d)^2 \quad (6.4)$$

Here $\omega = 2\pi f$ represents the frequency of the mode. D is the exchange stiffness which is related with exchange constant A_{ex} by $A_{ex} = \frac{DM_s}{2g\mu_B}$. (g : g-factor. M_s saturation magnetization. μ_B Bohr magneton). s is a numerical factor which is close to 3.68. By perform a linear fit of Fig.6.4(b) we can obtain the A_{ex} value of 8.9 pJ/m, which is reduced from the bulk value around 15 pJ/m.

6.3 Micromagnetic Simulations of the Mode Spacing

After we obtained reliable experimental data, we can use Micromagnetic simulation to determine the exchange stiffness based on the mode spacings. Fig.6.5 shows the simulated Magnetic Tunnel Junctions(MTJs) with magnetization and thickness for each active layer. The free layer and SAF top layer magnetization are obtained from independent measurement results and the SAF Bottom layer magnetization is determined by simulating the magnetization versus external magnetic field curve so that the center of the magnetization curve is close to zero. This is because of the balanced SAF layer dipolar field confirmed by the experiment.

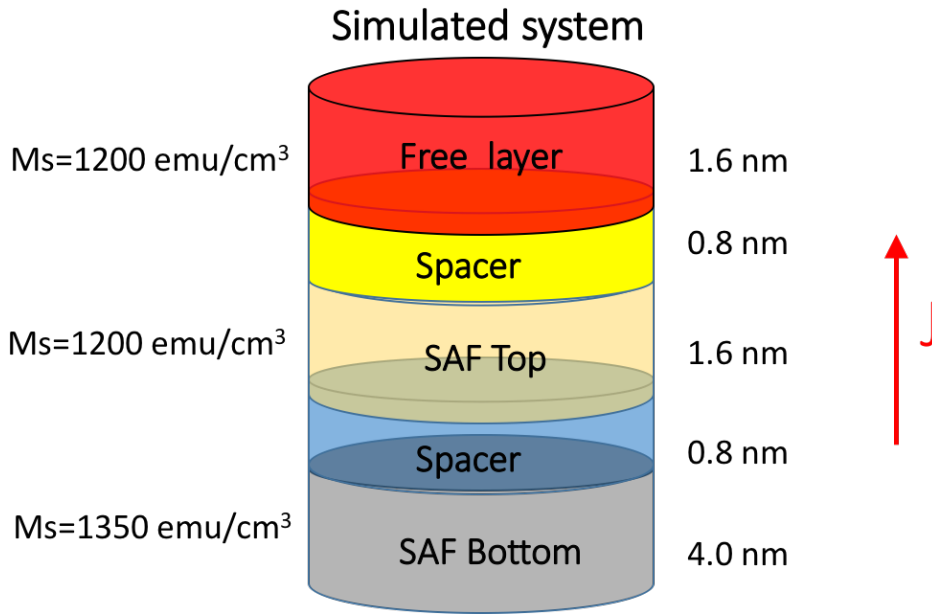


Figure 6.5: Simulated MTJs structures. The magnetization and thickness parameters are listed for each magnetic layer.

In the micromagnetic simulations, we use the perpendicular magnetic anisotropy to fit for the frequencies of the main mode. The mode gap is ideally determined only by the exchange stiffness. Fig.6.6(a) shows a typical simulated spectrum for 70 nm diameter circular devices with the magnet anisotropy $10.5 * 10^5 \text{ J/m}^3$ and the exchange stiffness A_{ex} 12 pJ/m. The mode profiles of these two modes are listed around the spectrum peak. The main mode has

uniform amplitude with small variations around the edges. The first higher-order mode has a node at the center of the circle. As we identified previously, the nominal circular devices have common shape distortions so that the actual size is not perfectly circular. In the next step of the simulations, we introduce such shape distortions to make a ellipse MTJ device. Fig.6.6(b) shows the simulated spectrum of ellipse devices with different degree of symmetry breaking. As we vary the shape distortion, the frequency of the main mode does not change too much, and the first order higher mode splits into two modes(mode 1 and 2). As the ellipticity increases, the frequency of the lower mode 1 decreases while the frequency of the higher mode 2 increases. Fig.6.6(c) shows the splitting of the first order mode(with node in the center) into two separate modes with nodes along the long and short axis of the ellipse.

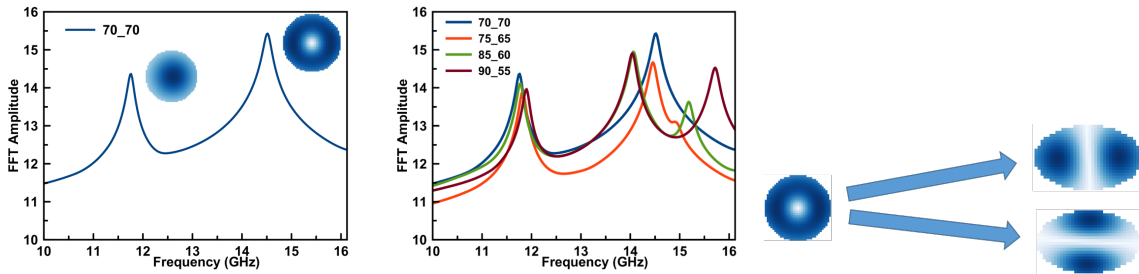


Figure 6.6: (a) Simulated 70 nm diameter spectrum with mode profiles showing around the peak. (b) Simulated spectrum with different elliptical shapes. (c) The mode profile splitting of the first higher order mode into two modes in the ellipse with nodes along short and long axis.

As we mentioned previously, the mode spacings between the main mode and the first higher order mode are ideally determined by the exchange stiffness. The question we need to answer now is how we define the mode spacing with shape distortions. Table.6.1 summarizes the simulated mode frequencies with different geometries and comparisons with the experimental data. As we can see from the table, as we increase the ellipticity, the mode gap (1+2)-0, which is defined as the average of mode 1 and mode 2 minus the mode 0, is nearly constant.

Now we can summarize the procedure of the mode spacing fitting for these nominal circular devices. We will use the average of mode 1 and 2 from the experiment to fit for the mode

	70*70	75*65	85*60	90*55	Experimental
Mode 0	11.74	11.82	11.78	11.9	11.55
Mode 1	14.5	14.46	14.06	14.04	13.94
Mode 2		14.9	15.2	15.72	14.6
Gap (1+2)/2-0	2.76	2.86	2.85	2.9	2.72
Gap 2-1	0	0.44	1.14	1.68	0.66
Aspect ratio	1	1.15	1.41	1.63	

Table 6.1: The simulated mode frequencies with different geometries and comparisons with the experimental data. All the numbers are in GHz unit.

spacings between the simulated mode 1 and 0 in circular device spectrum. It should be noted that the shape distortions can be random across the devices and the actual shape of each device can be different. This will create unavoidable uncertainty in the exchange stiffness fitting.

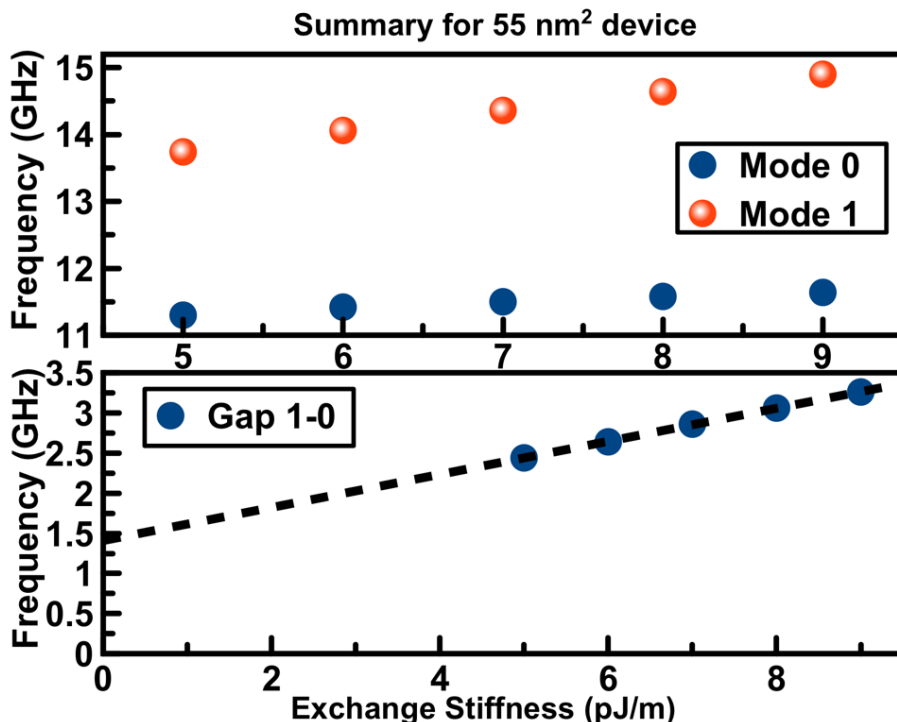


Figure 6.7: Top: Simulated mode frequencies for the first two modes excited in the 55 nm diameter circular devices as a function of the exchange constant. Bottom: The mode spacings as a function the exchange constant with linear fitting.

Before we move to detailed micromagnetic simulations, we need to consider the actual size of the MTJs. In the MTJ fabrication process, we find that the diameter of the MTJs in this batch is typically 14.4 nm smaller than the listed diameter. For nominal 70 nm devices, the input diameter is 55 nm (an integer number of micromagnetic cell size). The top of Fig.6.7 shows the simulated 55 nm frequencies of the main mode and first higher order mode as a function of input exchange stiffness. The frequencies of the two modes are increasing linearly with the exchange stiffness. The bottom of Fig.6.7 shows the mode spacings between the first two modes as a function of A_{ex} , which can be then fit by a line. The linear dependence of the mode spacings on the exchange stiffness is expected as we discussed in the Eq.6.4.

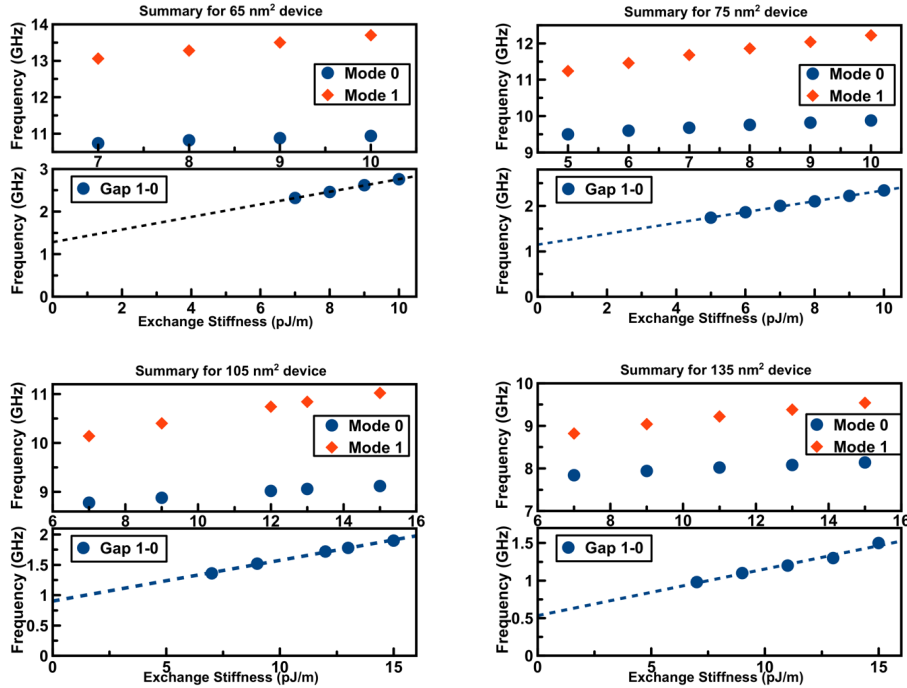


Table 6.2: Circular Device Simulation Summary. For different sizes, Both the frequencies of the two modes and the mode spacing are plotted against the exchange constant

Based on this linear relation, we can determine the best-fit exchange stiffness from the experimental value of mode spacings. Moreover, we can also obtain the standard deviations of the fitted exchange value based on the standard deviations of the mode spacings from the experiment. By varying the diameters of the devices, we can repeat this fitting procedure

for different sizes as listed in the Table.6.2. Typically we find that by varying the device diameter, the mode spacing has similar linear trend versus the exchange stiffness. The linear slope, however, is decreasing as the device diameter increases. Since the linear slope gives the sensitivity of the exchange stiffness fitting, the relatively larger devices mode spacings are less sensitive to the exchange, which introduces larger fitting variations as we will see.

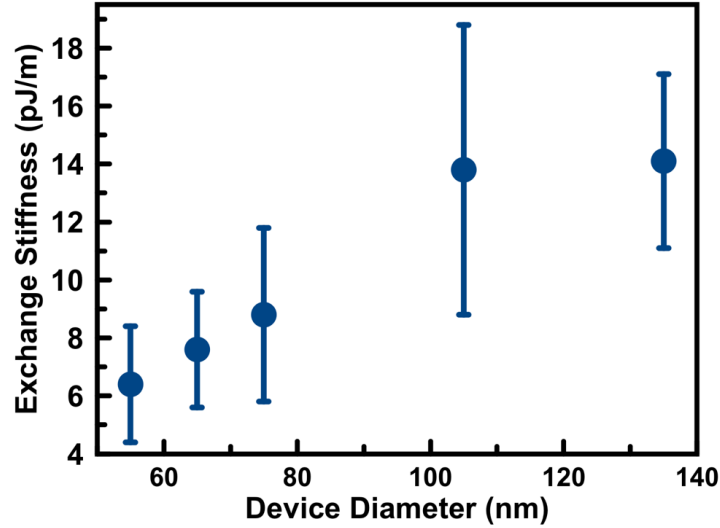


Figure 6.8: Circular Device Simulation Summary. For each nominal device, we list the simulated diameter(15 nm smaller). The exchange stiffness and the standard variations are listed.

Fig.6.8 summarizes the exchange stiffness fitting for different geometries. The values are listed in the Table.6.3. The actual simulated diameters are 15 nm smaller than the nominal size. The exchange stiffness is determined by the experimental mode spacings and simulated linear relations between mode spacings and simulation exchange stiffness. The standard deviations are obtained from the standard deviations of the mode spacing.

There are two major conclusions here. First, we find that for all the five diameters there are reductions of the exchange stiffness compared with the bulk value of the Co and Fe thin films, which is in the range of 15 pJ/m and 25 pJ/m. The reductions of the exchange stiffness from the thin films to the MTJs devices have been observed from our collaborators and from our previous continuous FMR simulations as well. One possible origin is the formation

Nominal Device length (nm)	Device Length* (nm)	A _{ex} (pJ/m)	Error (pJ/m)
70	55	6.4	2
80	65	7.6	2
90	75	8.8	3
120	105	13.8	5
150	135	14.1	3

Table 6.3: Summary of fitted exchange stiffness for different diameters.

of different grains within the MTJs free layer and the reduction of inter-grain exchange couplings.

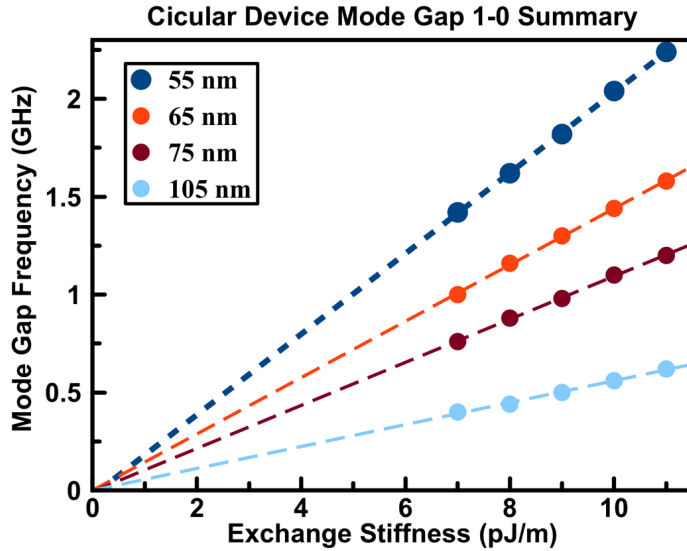


Figure 6.9: Simulations of the mode spacings as a function of the exchange stiffness for different diameters. The MTJs only has a magnetic free layer.

Second, we find that the exchange stiffness is increasing as the device diameter increases. We have not fully understood this behavior at this time. However, as we mentioned earlier, the mode spacings of the larger devices are less sensitive to the exchange stiffness. Moreover, since the determination of the exchange stiffness depends on the actual geometries, if the larger devices deviate more from the nominal size, it would create more error in the exchange stiffness fitting.

Before we move to other geometries, we find that the mode spacings do not go to zero as the exchange stiffness shown in the Fig.6.8. If we would only consider the exchange couplings

between the free layers, the mode spacings should go to zero at zero A_{ex} . To understand this behavior, we perform the same simulation without the SAF layers in the MTJs as shown in the Fig.6.9. Only the dynamics of the free layer is considered in this simulation. We also plot the mode spacings as a function of the A_{ex} for different diameters. We find that the mode spacings go to zero as the A_{ex} goes to zero in this free-layer-only simulation. So we can conclude that the non-zero intercept of the mode spacings at zero A_{ex} is likely due to the dipolar field from the SAF layers on the free layer.

6.4 Study of signal amplitude of ST-FMR signal

While we have not discussed the origin of the ST-FMR signal in the perpendicular magnetized MTJs with magnetic field applied in the easy axis, the exact source of the signal is not very clear. In fact, in a ideal circular device with rotation symmetry, such arrangement should yield no DC self rectification since the spin transfer torque is zero with free layer pinned in the perpendicular direction. However, we can still detect a measurable signal out of this set-up. It is argued that there are local misalignments between the uniaxial anisotropy and applied magnetic field due to shape distortion[62]. It is also possible that the non-uniformity of spin-transfer torque from the tunnel current across the free layer and non-uniform tunnel magnetoresistance (TMR) should contribute to the ST-FMR signal. Previous work has been done to quantitatively measure the spin-transfer-torque in the ST-FMR signal[57][88][89] for the MTJs with in-plane easy axis. At the same time, Ab initio studies has been done to study the spin-transfer torque in MTJs[90]. However, in our field-modulated ST-FMR set-up, such experiments are not accessible since we are actually measuring the field derivatives of the real signal. Nevertheless, we still would like to qualitatively measure the signal amplitude of our ST-FMR data and try to gain some knowledge out of it.

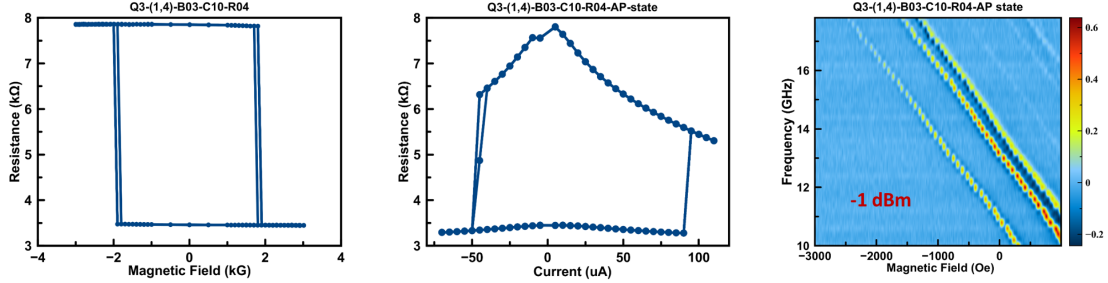


Figure 6.10: (a) Example magnetoresistance of one 60 nm * 80 nm stadium-shaped MTJ device. (b) The resistance versus current loop, with AP state switching to P state at negative dc current and vice versa. (c) 2D contour plot of the ST-FMR signal of this device with -1 dBm power applied at the AP state

The device employed in this study has a stadium shape with lateral dimensions 60 nm * 80 nm. The introduced broken symmetry away from perfect circular is designed to promote better ST-FMR signal. Fig.6.10(a) shows the magnetoresistance of this device, which has resistance of 3445 Ohms at the parallel state and 7800 Ohms at the anti-parallel state. The coercive field is about 1850 Oe. Fig.6.14(a) shows the resistance versus current loop. The negative(positive) current is the anti-damping polarity for AP to P(P to AP)state. This demonstrate the effect of spin-transfer-torque switching. Fig.6.10(c) shows the 2D contour plot of the ST-FMR signal of this device with -1 dBm power applied at the AP state. Again we can mainly identify three of the spin wave modes.

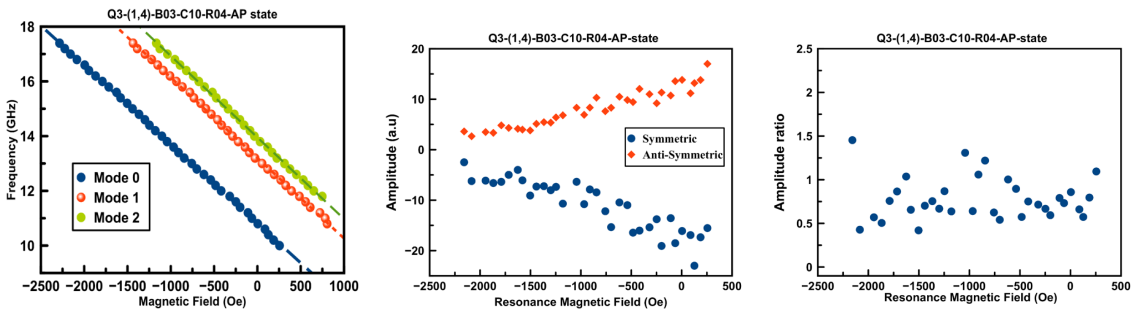


Figure 6.11: (a) The resonance field fitting result for all the three modes. (b) The ST-FMR signal (symmetric and anti-symmetric component) plot versus resonance field. (c) The ratio of two components versus resonance magnetic field.

Fig.6.11(a) summarizes the mode fitting result for all the three modes we excited from this stadium shape device. The linear relation is reproduced as expected. The main mode at zero field is 10.81 GHz and the effective anisotropy field H_k around 3.7 kG. Fig.6.11(b) shows the ST-FMR signal (symmetric and anti-symmetric component) plot versus resonance field. The amplitude is larger at small field and smaller at negative large magnetic field. This is due to magnetic susceptibility as expected. As we can see from Fig.6.10(a) that the MTJ at the AP state aligns better with the external negative magnetic field, which gives smaller ST-FMR amplitude. Fig.6.11(c) shows the ratio of two components versus resonance magnetic field. And we see that the ratio remain relatively unchanged over the resonance field. The ratio of this two components is related with different signal mechanism which will be discussed later.

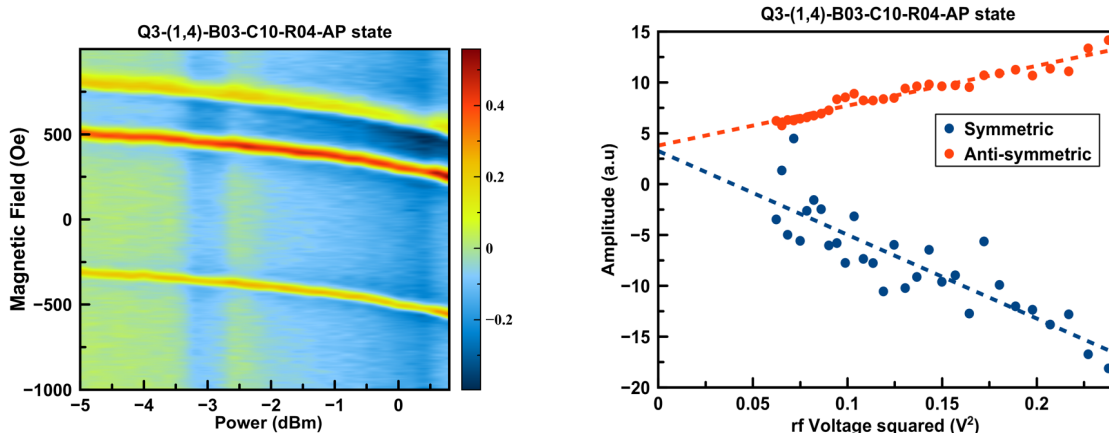


Figure 6.12: (a) The power-dependent ST-FMR field sweep spectrum at AP state with 12 GHz. (b) The amplitude versus the square of rf voltage.

The applied power determines the rf voltage across the MTJs. Fig.6.12(a) shows the power-dependent ST-FMR field sweep spectrum at AP state with 12 GHz. We can then plot the amplitude versus the square of rf voltage as shown in Fig.6.12(b). The good linear fit indicating the ST-FMR signal mainly arises from rectification [91]. As the rf voltage approaches zero, both symmetric and anti-symmetric components goes to zero at a similar value. In fact, if we apply zero dc bias into the MTJ, this limit will go to zero at zero rf

voltage. Thus we can confirm there is also a non-zero contribution from the photo-resistance effect[92].

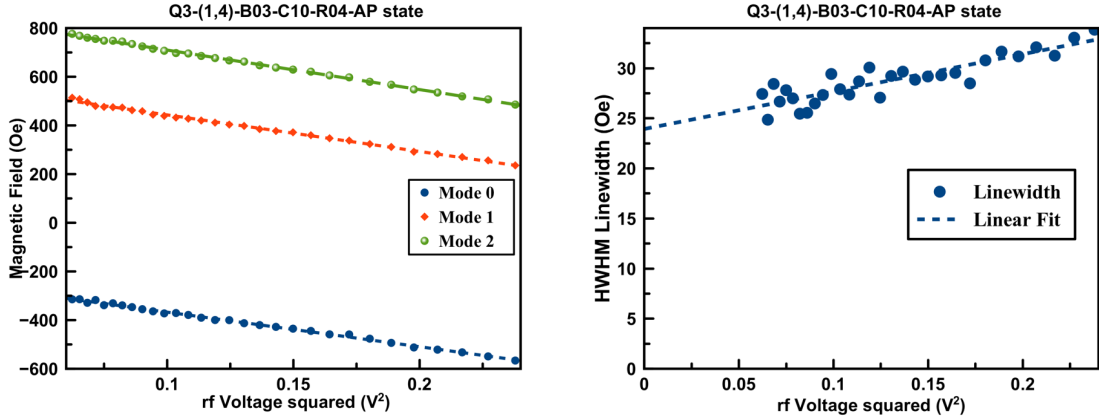


Figure 6.13: (a) The resonance Field versus rf voltage squared for all the modes at 12 GHz. (b) The Mode 0 HWHM linewidth versus rf voltage squared.

Fig.6.13(a) shows the resonance Field versus rf voltage squared for all the modes at 12 GHz and Fig.6.13(b) shows the Mode 0 HWHM linewidth versus rf voltage squared. The linewidth shows a linear dependence with zero rf voltage linewidth around 23 Oe. The linear relation of both resonance field and linewidth ensures that we keep the ST-FMR measurement at the linear region where there is no non-linear broadening of the signal.

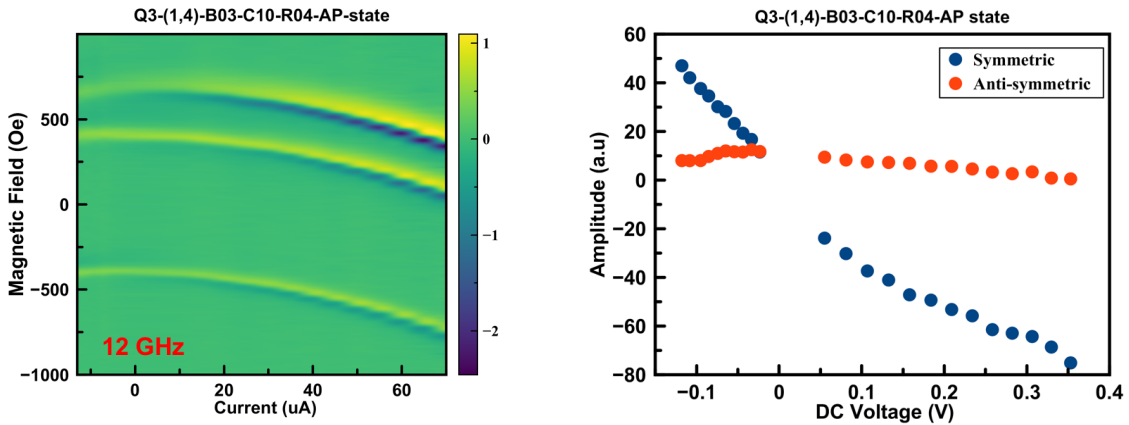


Figure 6.14: (a) The bias-dependent ST-FMR field sweep spectrum at AP state with 12 GHz. (b) FMR signal amplitude versus applied dc voltage.

After we vary the applied power in the ST-FMR measurement, it is also interesting to change the dc bias. Fig.6.14(a) shows the bias-dependent ST-FMR field sweep spectrum at AP state with 12 GHz. All the three modes have the same curvature under external bias, which proves that these are all the spin-wave modes from the free layer. Fig.6.14(b) shows the FMR signal amplitude versus applied dc voltage. We find that the symmetric component (relating to spin transfer torque) shows a quadric+linear dependent and the anti-symmetric component was nearly invariant versus bias.

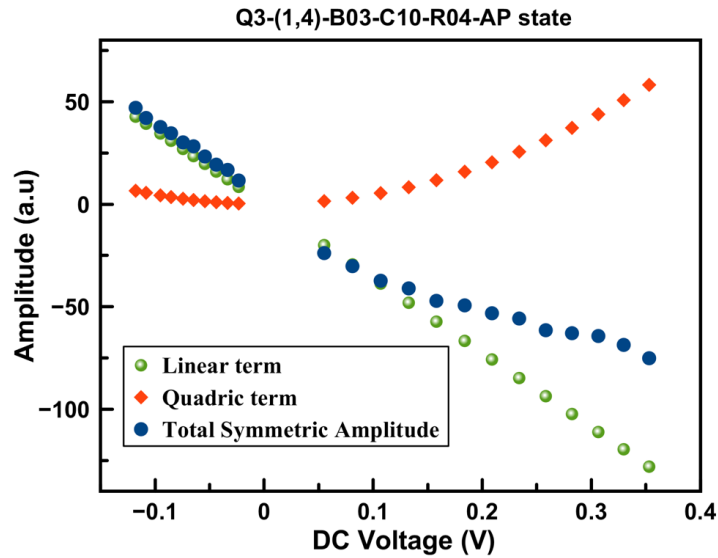


Figure 6.15: Fitting of the FMR symmetric amplitude versus DC voltage as a sum of linear term and quadric term.

We can further analyze the FMR symmetric amplitude versus DC voltage as shown in Fig.6.15. The Symmetric amplitude shows as sum of linear term and quadric term. The linear term, related to the photo-resistance contribution, changes the sign with different polarity of dc voltage. Moreover, the linear term is nearly dominated except at large dc voltage, which indicating that the photo-resistance effect is not negligible in the system!

The ST-FMR signal of MTJs with PMA can be modeled as shown in the Fig.6.16. In the MTJs, there is a small angle θ_{mis} between the free layer and the fixed layer. The magnetic field H is applied in the perpendicular direction. After apply dc bias and microwave power,

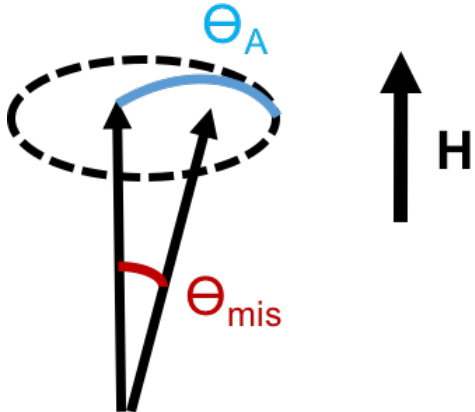


Figure 6.16: Demo of Perpendicular magnetized MTJs angle oscillation with out-of-plane magnetic field.

the resistance of the MTJ can be written as

$$R = R_{dc} + R_{ac} \sin \omega t + R_{20} \sin 2\omega t \quad (6.5)$$

Here the R_{dc} is the time-averaged MTJ resistance and R_{ac} is the oscillating MTJ resistance. R_{20} is the higher harmonic component of the resistance. The amplitude the angular oscillation is θ_A . After we define those variables, the ST-FMR signal can be expressed as

$$V_{ST-FMR} \propto I_{dc}R_{dc} + \frac{1}{2} < I_{ac}R_{ac} > \quad (6.6)$$

The first term is related with contributions from photo-voltage(related to rectification) and the second term is related with photo-resistance(related to time-averaged resistance).

Before we end this section, we can also fit the spin-wave modes under finite dc bias. Fig.6.17(a) shows the resonance field versus bias for three modes. The main mode has both linear and quadratic dependence. The quadratic dependence is harder to analyze since it is a mixed contribution from field-like torque and ohmic heating. The linear term is believed to relate with voltage-controlled magnetic anisotropy(VCMA). The linear slope gives VCMA 244 Oe/V,

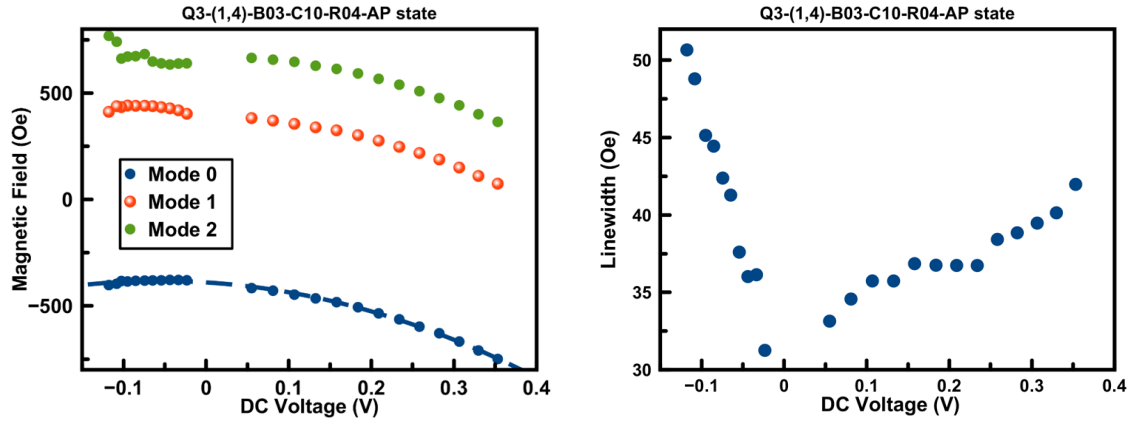


Figure 6.17: (a) The resonance field versus bias for three modes. (b) Mode 0 HWHM linewidth versus applied dc bias.

close to previously measured circular devices. Fig.6.17(b) shows Mode 0 HWHM linewidth versus applied bias. At positive voltage(damping), we find the linewidth increase as increasing voltage(as expected). At negative voltage(anti-damping),however, the linewidth unexpectedly increase with larger negative voltage. This is also a strong evidence of non-linear damping in this type of devices. One possible explanation is that, when approaching the switching region, the free layer has more fluctuations which contributes to the linewidth broadening.

6.5 Summary of Stadium shapes MTJs devices with 60 nm width

As we have measured circular devices with different diameters, for stadium devices, we also have measured devices with nominal 60 nm width and length from 70 nm to 210 nm. Before we move to the mode statistics, we first check the mode structures for these 60 nm devices. Fig.6.18(a) shows the Magneto-resistance curve for one typical 210 nm * 60 nm device. Fig.6.18(b) shows the ST-FMR field sweep 2D spectrum at AP state with example scan at 12 GHz. From the sample trace at 12 GHz, we find that for these larger devices, although the mode density becomes large and there are more higher order modes with smaller mode spacings, we still reproduce the general mode structures as the circular devices: one main mode at the lowest frequency and two first higher-order modes.

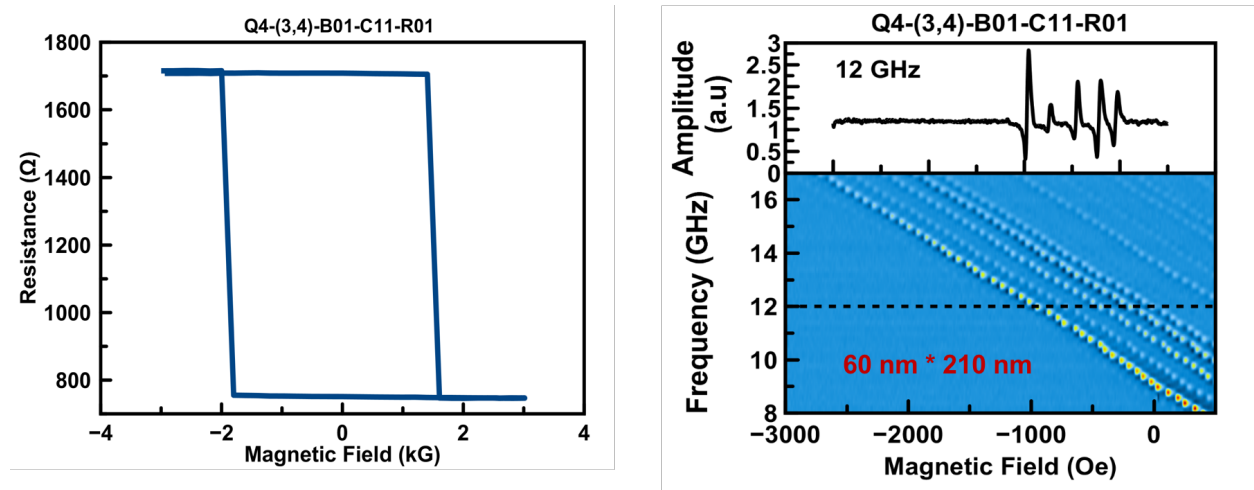


Figure 6.18: (a) Magneto-resistance curve for 210 nm * 60 nm devices (b) ST-FMR field sweep 2D spectrum at AP state with example scan at 12 GHz.

Since we have reproduced the similar mode profiles as circular devices, we will use the same mode spacing as the circular devices to compare with the micromagnetic simulations: the average of the first two higher order modes minus the lowest main mode. To obtain the experimental spacings for stadium-shape devices with different length, we first performed

detailed ST-FMR measurements and obtained good mode frequencies statistics. The summary of the stadium devices with 60 nm nominal width and varying length from 70 nm to 210 nm is listed in Fig.6.19.

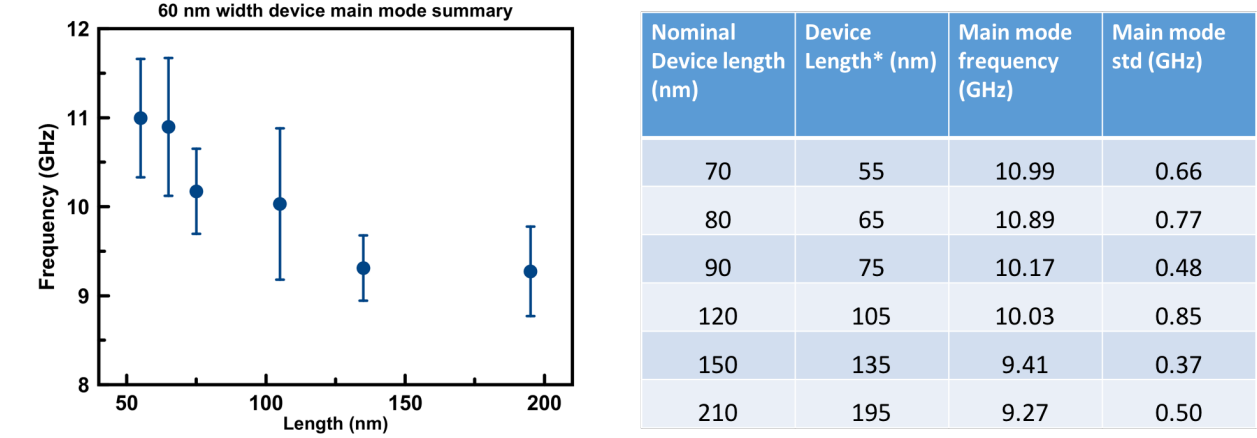


Figure 6.19: Main mode frequency with standard deviations versus device length for 60 width devices. The plotted device length is 15 nm smaller than nominal size

We plot the main mode frequency with standard deviations versus device length for nominal 60 nm width devices. The plotted device length is 15 nm smaller than nominal size. The main mode frequency drops over 15 per cent, which is due to shape anisotropy reductions for larger devices.

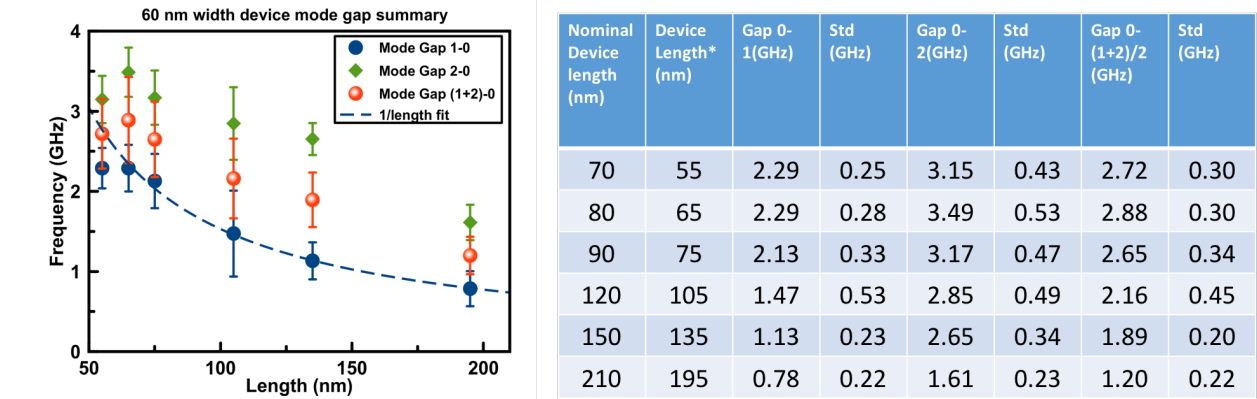


Figure 6.20: Mode gap with standard deviations versus device length for nominal 60 nm width devices. The mode gap is decreasing as increasing length.

In the next step, we plot the mode gap with standard deviations versus device length for nominal 60 nm width devices. The mode gap is decreasing as increasing length. The mode

gap between mode 0 and 1 gives a nice 1/length fit in the limit of large aspect ratio as it plotted in the dash line. We can conclude that the 1/length dependence points to the importance of dipole-dipole contributions to the gap values and it should be possible to extract the exchange parameter from this 1/length dependence. We think that a more advanced fitting function is needed to cover the smaller aspect ratios.

6.5.1 Micromagnetic simulations of stadium devices

We use similar full-stack MTJ structures as shown in Fig.6.5 to perform micromagnetic simulations to determine the exchange stiffness. To account for the real shape, we also reduce 15 nm from the nominal value in the simulations. Fig.6.21 shows the Example of simulation spectrum for $45*65\text{ nm}^2$ device (nominal dimension: $60*80\text{ nm}^2$) with mode profile showing around the peak. For this stadium shape device, there are clear two higher order modes with node along short and long axis. Two key parameters used in Fig.6.21 are magnet anisotropy $10.05 * 10^5\text{ J/m}^3$ and the exchange stiffness $A_{ex} 7\text{ pJ/m}$. The simulated mode frequencies and mode spacings are listed to be compared with the experimental data. We can see that we already have a relatively good fitting result(keep in mind that $A_{ex} 7\text{ pJ/m}$ is the average value for circular devices).

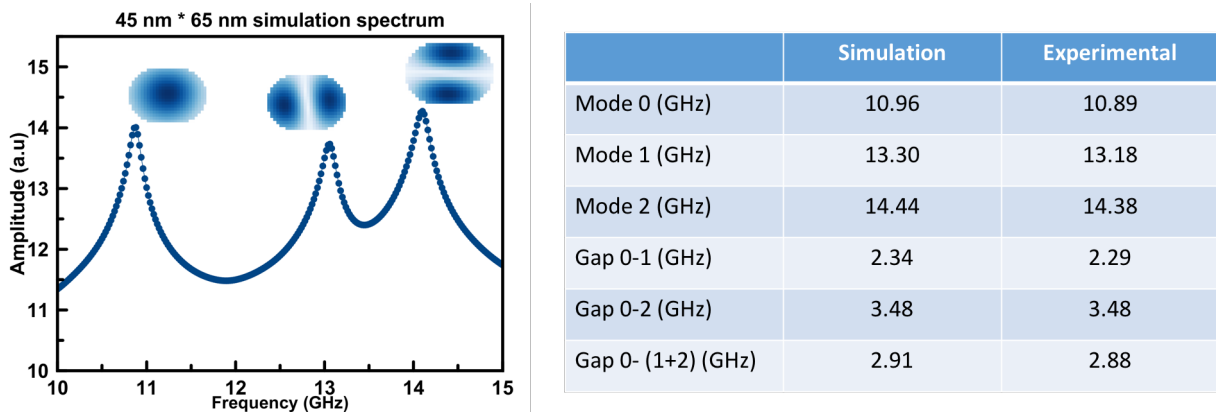


Figure 6.21: Example of simulation spectrum for $45*65\text{ nm}^2$ device.

One advantage of these stadium shape devices is that the mode structures is quite straightforward and we can reproduce the experimentally measured lowest three modes without worrying about the shapes distortions in the circular devices. Fig.6.22(a) shows the experimental mode frequencies compared with simulation values in different exchange stiffness (unit in pJ/m) and Fig.6.22(b) shows the experimental mode frequencies compared with simulation values in different exchange stiffness (unit in pJ/m). As we know, the separation between mode 1-2 is susceptible to device dimension variations, so we still used the mode spacings between the average of mode 1 and mode 2 and mode 0 to determine the exchange stiffness.

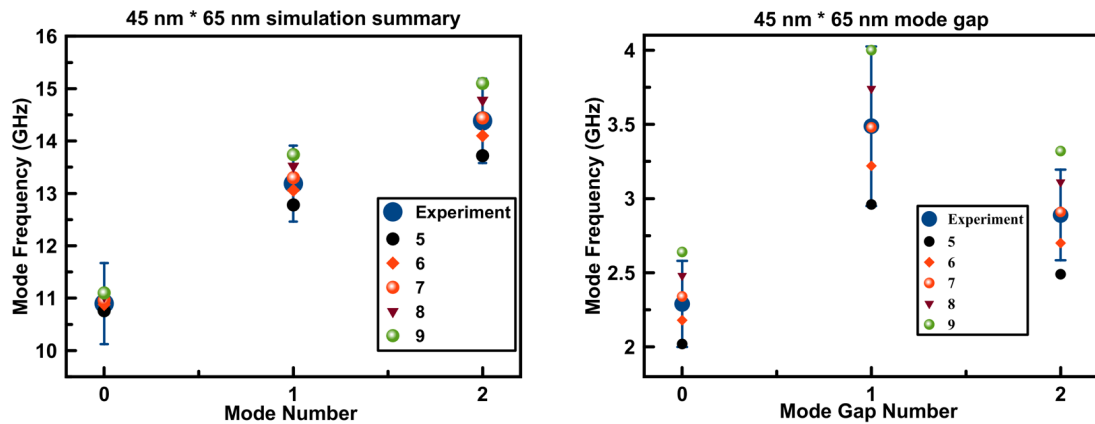


Figure 6.22: (a) Experimental mode frequencies compared with simulation values in different exchange stiffness (unit in pJ/m). (b) Experimental mode spacing compared with simulation values in different exchange stiffness (unit in pJ/m).

Fig.6.24 shows the mode gaps plotted versus simulated exchange stiffness for $45*65\text{ nm}^2$ devices. Compared with circular devices we talked before, we also identify a clear linear dependence between mode spacings and A_{ex} . Similarly, we find that all the mode gaps do not extrapolate to zero in the limit of zero A_{ex} . This is because of the dipole-dipole interactions, which is reducing the sensitivity of this methods for finding the exchange stiffness.

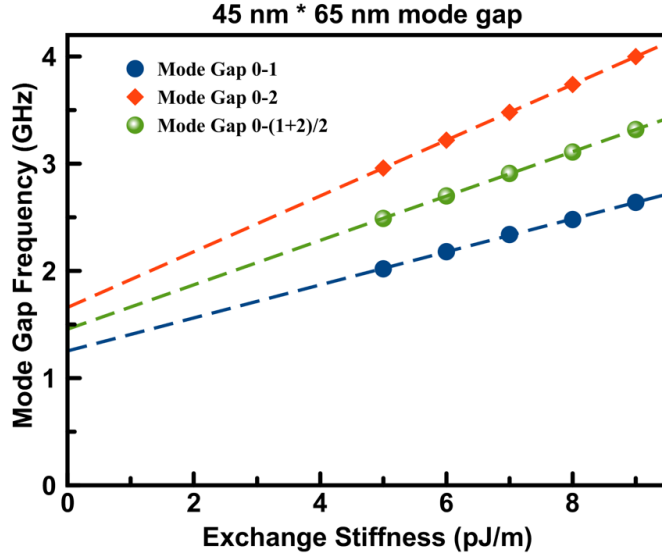


Figure 6.23: Mode Gap plotted versus simulated exchange stiffness for $45*65\text{ nm}^2$ device.

We can then vary the length of the devices at fixed width 45 nm and obtain the A_{ex} as a function of device length as showing in Fig.6.24 with numbers listed in the table. We find that for relatively smaller devices, from 70 nm to 120 nm length, the exchange stiffness fitted is quite close: around 7 pJ/m with similar standard error. Keep mind that the standard error is obtained from the variations of the mode spacings.

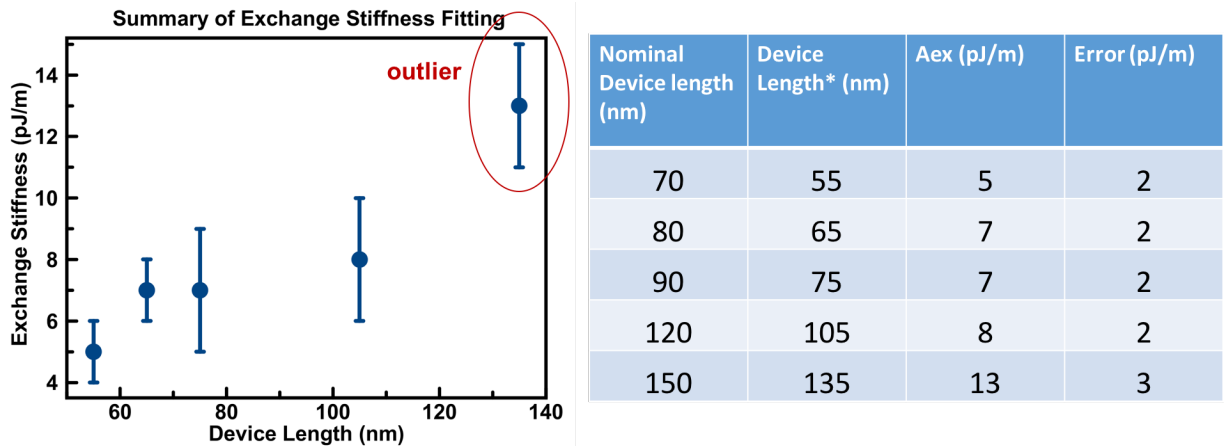


Figure 6.24: Mode Gap plotted versus simulated exchange stiffness for $45*65\text{ nm}^2$ device.

However, for larger devices, we find that there is a strong increase of exchange stiffness for 150 nm devices. It is not clear the origin of this outlier point but we believe it is an artifact

for this particular geometry. First of all by performing in-plane ST-FMR measurements, we make sure that there is no missing modes and the mode identification is correct. Secondly, we also find that resistance-area product for this 45-nm-width group does not show any anomaly for larger devices. So the outlier only has two possible origins: one is that the dipole-dipole interaction for larger devices is more pronounced, which reduces the reliability of our methods of exchange stiffness fitting. The second one is that the real size of larger devices is not the value we used in the simulations. If the device's size is not nearly 15 nm smaller than the nominal value, we can not trust the values we obtained from the micromagnetic simulations.

6.6 Summary of stadium shapes MTJs devices with 45 nm width

To complete our studies of stadium shapes, we have measured devices with constant nominal width 45 nm and varying length from 60 nm to 120 nm. As usual the actual size of the devices is roughly 15 nm smaller than the nominal values. So for this 45 nm width group of devices, the aspect ratio is larger than the previous devices we have measured. The aspect ratio is greater than 1.5 and we will see how it can be reflected in the mode structures.

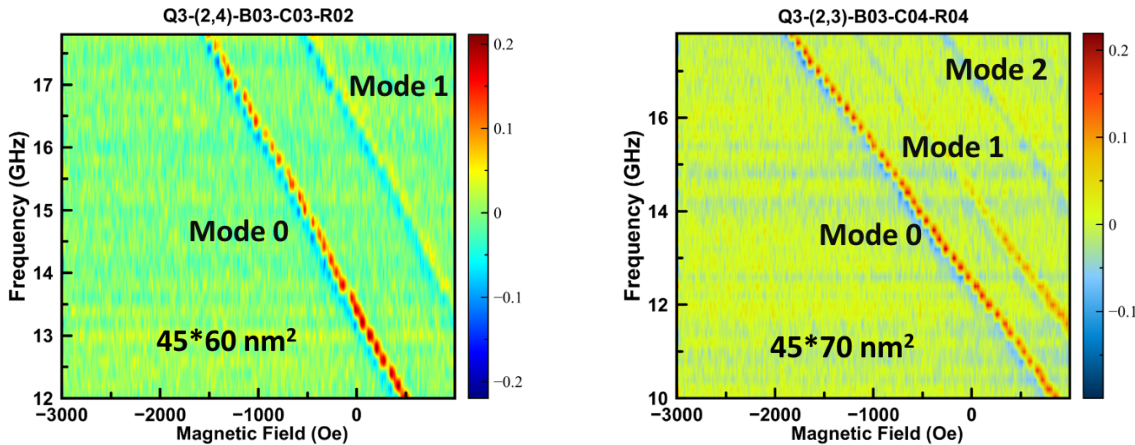


Figure 6.25: (a) Examples of 2D ST-FMR contour plot for nominal $45 \times 60 \text{ nm}^2$ device. (b) Examples of 2D ST-FMR contour plot for nominal $45 \times 70 \text{ nm}^2$ device.

We show the example 2D ST-FMR contour plots for these 45 nm devices in the above. The sample shown in Fig.6.25(a) is $45 \times 60 \text{ nm}^2$ and Fig.6.25(b) shows a $45 \times 70 \text{ nm}^2$ device. The major difference for devices with 45 nm width is that the mode spacing between mode 1 and mode 2 is quite large. Remember that for this group of samples, the actual aspect ratio is greater than 1.5 so that the energy barrier between these two higher order modes are larger. In the experiment, we usually find that we can only excite the mode 1 clearly for these higher aspect ratio devices. For example, in Fig.6.25(a) there is only mode 1 visible in the plot and in Fig.6.25(b), the mode 2 can only be seen faintly and can be not fitted in detail.

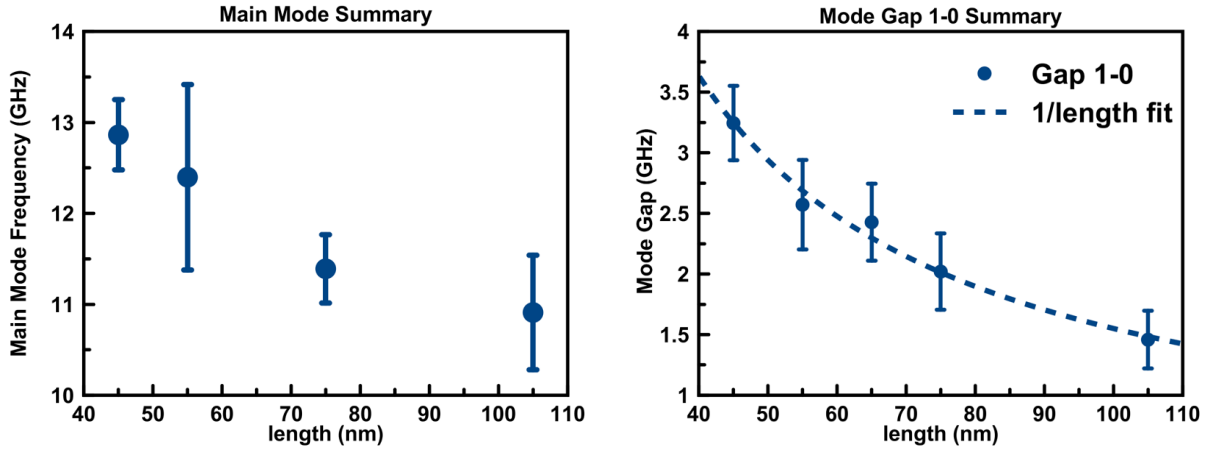


Figure 6.26: (a) Average main (0) mode frequency (with standard deviations) plotted versus actual device length (b) Mode Gap 1-0 shows a 1/length fit

One advantage of these high aspect ratio device is that good separations of between higher-order modes allows us to use the mode gap between main mode and mode 1 to determine the exchange stiffness without worrying about shape distortions. For devices with each length, we measure about ten samples to obtain mode statistics. Fig.6.26(a) shows the average main (0) mode frequency (with standard deviations) plotted versus actual device length. We also observed a clear reduction of main mode as increasing length due to decreasing shape anisotropy. Fig.6.26(b) shows the mode spacings between the first two modes plotted versus the device length. The mode spacing also shows a good 1/length fit which indicates the dipolar-dipolar interaction is not negligible in the system.

Previously we mentioned that it is important to know the real dimension of the device in the exchange stiffness fitting. One good indication of the device geometry is the resistance of the device. Fig.6.27(a) shows the AP state main mode frequency plotted versus AP state resistance for this group of devices. Clearly it shows correlation between main mode frequency and AP state resistance as we expected. For larger devices, the area is larger and the resistance is smaller, at the same time the main mode frequency is smaller as we discussed. Fig.6.27(b) shows mode Gap frequency plotted versus AP state resistance. The

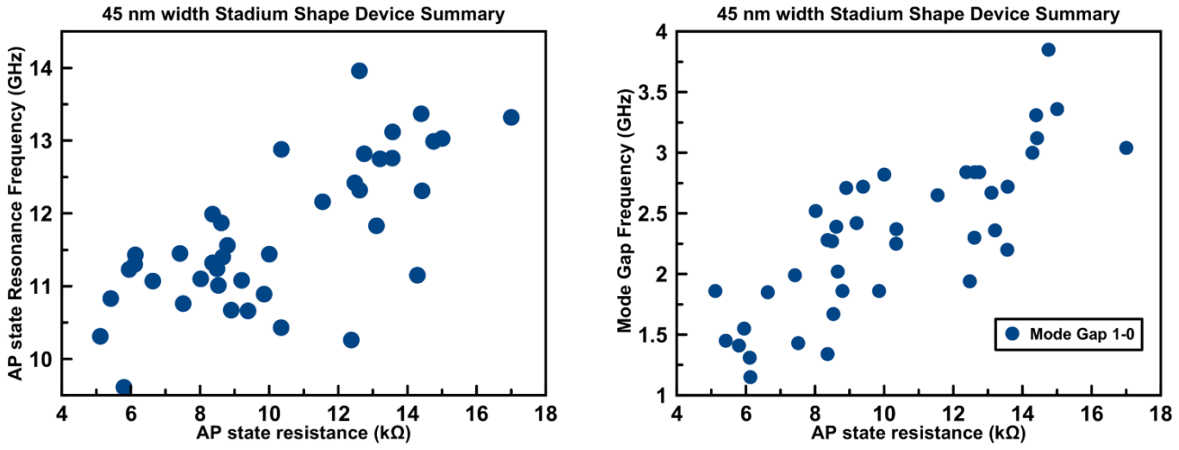


Figure 6.27: (a) AP state main mode frequency plotted versus AP state Resistance. (b) Mode Gap frequency plotted versus AP state Resistance

frequency gaps also scales approximately linearly with AP state resistance for the stadium shaped devices. We also find that in the limit of zero AP resistance, the mode gap frequency also goes to zero as expected. So we can fit for the mode gap based on the resistance which is much easier to measure compared with ST-FMR measurement.

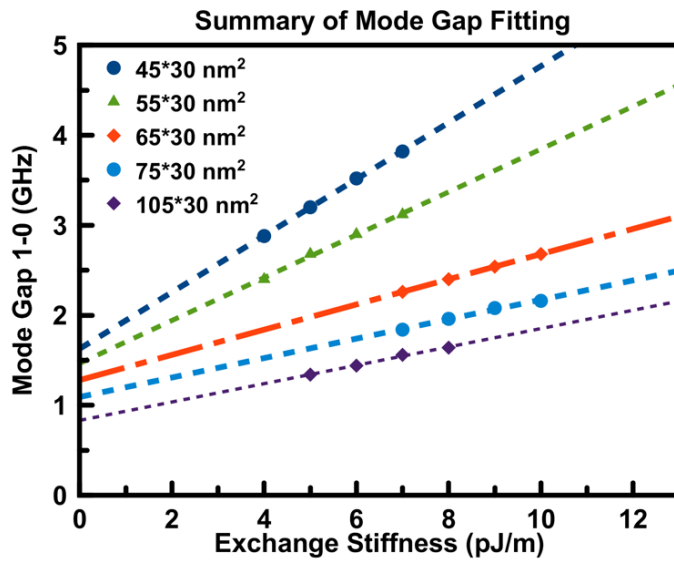


Figure 6.28: mode gap plotted versus simulated exchange stiffness for different geometries with same 30 nm width

Based on the experimental data we obtained from Fig.6.26(a) and Fig.6.26(b), we can perform similar micromagnetic simulations to determine the exchange stiffness. The only difference compared with previous simulations is that we now use the mode spacing between the main mode and the first higher order mode for comparisons between experimental data and simulation outputs. Fig.6.28 summarizes the mode gap plotted versus simulated exchange stiffness for different geometries with same width. Firstly, we find that the mode gap between mode 1-0 does not go to zero when approaching zero A_{ex} . This will agrees with our consumptions of non-negligible dipolar-dipolar interactions. Secondly, the slope of mode spacings versus the input exchange stiffness is steeper for nearly circular devices. This enables us to have more precise determination of the exchange stiffness.

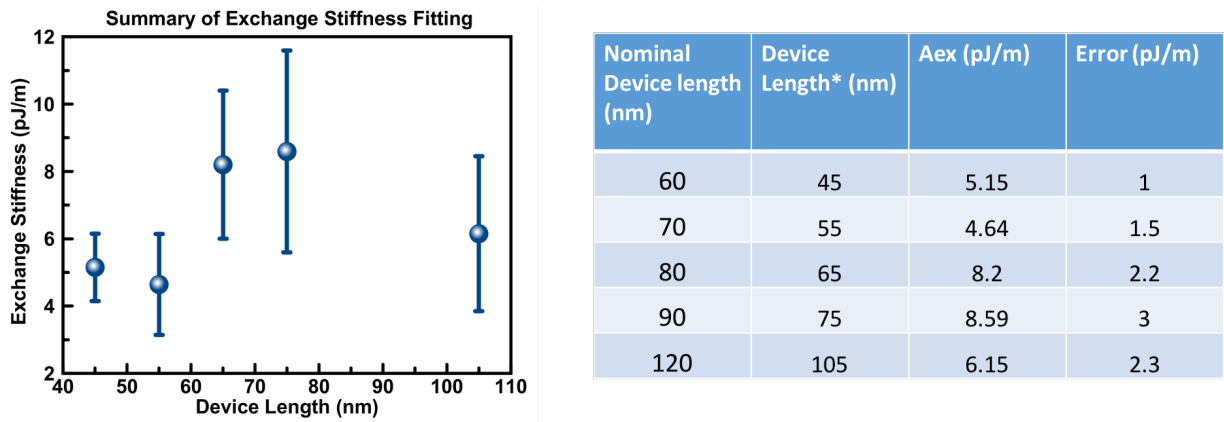


Figure 6.29: Summary of exchange stiffness fitting: size dependence of width 45 nm

Fig.6.29 summarizes the exchange stiffness fitting result for devices with same width(nominal 45 nm) and varying length. Compared with nearly circular devices, we have much less standard deviations thanks to improved sensitivity. For this group of devices, the fitted A_{ex} is near 5 pJ/m. The similar reductions of exchange stiffness from bluk values has also been reported[93], which might originates different composition and thickness of CoFeB used in the free layer as well as annealing conditions[94]. Furthermore, the fact that we have better fitting results for this group of higher aspect ratio devices than the nearly circular devices might not be best for study of A_{ex} due to shape distortions and eigenmodes mixing.

Bibliography

- [1] Wikipedia contributors. Ferromagnetism — Wikipedia, the free encyclopedia, 2018. [Online; accessed 03-March-2018].
- [2] Mark Johnson and R. H. Silsbee. Interfacial charge-spin coupling: Injection and detection of spin magnetization in metals. *Phys. Rev. Lett.*, 55:1790–1793, Oct 1985.
- [3] M. N. Baibich, J. M. Broto, A. Fert, F. Nguyen Van Dau, F. Petroff, P. Etienne, G. Creuzet, A. Friederich, and J. Chazelas. Giant magnetoresistance of (001)fe/(001)cr magnetic superlattices. *Phys. Rev. Lett.*, 61:2472–2475, Nov 1988.
- [4] G. Binasch, P. Grünberg, F. Saurenbach, and W. Zinn. Enhanced magnetoresistance in layered magnetic structures with antiferromagnetic interlayer exchange. *Phys. Rev. B*, 39:4828–4830, Mar 1989.
- [5] M. Julliere. Tunneling between ferromagnetic films. *Physics Letters A*, 54(3):225 – 226, 1975.
- [6] W. H. Butler, X.-G. Zhang, T. C. Schulthess, and J. M. MacLaren. Spin-dependent tunneling conductance of Fe|MgO|Fe sandwiches. *Phys. Rev. B*, 63:054416, Jan 2001.
- [7] D.C. Ralph and M.D. Stiles. Spin transfer torques. *Journal of Magnetism and Magnetic Materials*, 320(7):1190 – 1216, 2008.
- [8] Arne Brataas, Andrew D. Kent, and Hideo Ohno. Current-induced torques in magnetic materials. *Nat Mater*, 11(5):372–381, May 2012.
- [9] C. Wang, Y.-T. Cui, J. Z. Sun, J. A. Katine, R. A. Buhrman, and D. C. Ralph. Bias and angular dependence of spin-transfer torque in magnetic tunnel junctions. *Phys. Rev. B*, 79:224416, Jun 2009.
- [10] Yiming Huai, Frank Albert, Paul Nguyen, Mahendra Pakala, and Thierry Valet. Observation of spin-transfer switching in deep submicron-sized and low-resistance magnetic tunnel junctions. *Applied Physics Letters*, 84(16):3118–3120, 2004.
- [11] Jian-Gang (Jimmy) Zhu and Chando Park. Magnetic tunnel junctions. *Materials Today*, 9(11):36 – 45, 2006.

- [12] S. Tehrani, B. Engel, J. M. Slaughter, E. Chen, M. DeHerrera, M. Durlam, P. Naji, R. Whig, J. Janesky, and J. Calder. Recent developments in magnetic tunnel junction mram. *IEEE Transactions on Magnetics*, 36(5):2752–2757, Sep 2000.
- [13] Sbiaa R., Meng H., and Piramanayagam S. N. Materials with perpendicular magnetic anisotropy for magnetic random access memory. *physica status solidi (RRL) Rapid Research Letters*, 5(12):413–419.
- [14] Zhitao Diao, Alex Panchula, Yunfei Ding, Mahendra Pakala, Shengyuan Wang, Zhanjie Li, Dmytro Apalkov, Hideyasu Nagai, Alexander Driskill-Smith, Lien-Chang Wang, Eugene Chen, and Yiming Huai. Spin transfer switching in dual mgo magnetic tunnel junctions. *Applied Physics Letters*, 90(13):132508, 2007.
- [15] Yiming Huai, Frank Albert, Paul Nguyen, Mahendra Pakala, and Thierry Valet. Observation of spin-transfer switching in deep submicron-sized and low-resistance magnetic tunnel junctions. *Applied Physics Letters*, 84(16):3118–3120, 2004.
- [16] W. J. Gallagher and S. S. P. Parkin. Development of the magnetic tunnel junction mram at ibm: From first junctions to a 16-mb mram demonstrator chip. *IBM Journal of Research and Development*, 50(1):5–23, Jan 2006.
- [17] R. Scheuerlein, W. Gallagher, S. Parkin, A. Lee, S. Ray, R. Robertazzi, and W. Reohr. A 10 ns read and write non-volatile memory array using a magnetic tunnel junction and fet switch in each cell. In *2000 IEEE International Solid-State Circuits Conference. Digest of Technical Papers (Cat. No.00CH37056)*, pages 128–129, Feb 2000.
- [18] S. Tehrani, J. M. Slaughter, M. Deherrera, B. N. Engel, N. D. Rizzo, J. Salter, M. Durlam, R. W. Dave, J. Janesky, B. Butcher, K. Smith, and G. Gryniewich. Magnetoresistive random access memory using magnetic tunnel junctions. *Proceedings of the IEEE*, 91(5):703–714, May 2003.
- [19] R. D. Gomez, T. V. Luu, A. O. Pak, K. J. Kirk, and J. N. Chapman. Domain configurations of nanostructured permalloy elements. *Journal of Applied Physics*, 85(8):6163–6165, 1999.
- [20] K. Yu. Guslienko, V. Novosad, Y. Otani, H. Shima, and K. Fukamichi. Field evolution of magnetic vortex state in ferromagnetic disks. *Applied Physics Letters*, 78(24):3848–3850, 2001.
- [21] E. Girgis, J. Schelten, J. Shi, J. Janesky, S. Tehrani, and H. Goronkin. Switching characteristics and magnetization vortices of thin-film cobalt in nanometer-scale patterned arrays. *Applied Physics Letters*, 76(25):3780–3782, 2000.
- [22] B. D. Schrag, A. Anguelouch, Gang Xiao, P. Trouilloud, Yu Lu, W. J. Gallagher, and S. S. P. Parkin. Magnetization reversal and interlayer coupling in magnetic tunneling junctions. *Journal of Applied Physics*, 87(9):4682–4684, 2000.

- [23] S. Mangin, D. Ravelosona, J. A. Katine, M. J. Carey, B. D. Terris, and Eric E. Fullerton. Current-induced magnetization reversal in nanopillars with perpendicular anisotropy. *Nature Materials*, 5:210 EP –, Feb 2006. Article.
- [24] Kumiko Nomura, Keiko Abe, Hiroaki Yoda, and Shinobu Fujita. Ultra low power processor using perpendicular-stt-mram/sram based hybrid cache toward next generation normally-off computers. *Journal of Applied Physics*, 111(7):07E330, 2012.
- [25] Hao Meng and Jian-Ping Wang. Spin transfer in nanomagnetic devices with perpendicular anisotropy. *Applied Physics Letters*, 88(17):172506, 2006.
- [26] Shinji Yuasa, Taro Nagahama, Akio Fukushima, Yoshishige Suzuki, and Koji Ando. Giant room-temperature magnetoresistance in single-crystal fe/mgo/fe magnetic tunnel junctions. *Nature Materials*, 3:868 EP –, Oct 2004.
- [27] Stuart S. P. Parkin, Christian Kaiser, Alex Panchula, Philip M. Rice, Brian Hughes, Mahesh Samant, and See-Hun Yang. Giant tunnelling magnetoresistance at room temperature with mgo (100) tunnel barriers. *Nature Materials*, 3:862 EP –, Oct 2004.
- [28] S. Ikeda, J. Hayakawa, Y. Ashizawa, Y. M. Lee, K. Miura, H. Hasegawa, M. Tsunoda, F. Matsukura, and H. Ohno. Tunnel magnetoresistance of 604% at 300k by suppression of ta diffusion in cofebmgocofeb pseudo-spin-valves annealed at high temperature. *Applied Physics Letters*, 93(8):082508, 2008.
- [29] S. Ikeda, K. Miura, H. Yamamoto, K. Mizunuma, H. D. Gan, M. Endo, S. Kanai, J. Hayakawa, F. Matsukura, and H. Ohno. A perpendicular-anisotropy cofeb-mgo magnetic tunnel junction. *Nature Materials*, 9:721 EP, Jul 2010.
- [30] H. Tomita, S. Miwa, T. Nozaki, S. Yamashita, T. Nagase, K. Nishiyama, E. Kitagawa, M. Yoshikawa, T. Daibou, M. Nagamine, T. Kishi, S. Ikegawa, N. Shimomura, H. Yoda, and Y. Suzuki. Unified understanding of both thermally assisted and precessional spin-transfer switching in perpendicularly magnetized giant magnetoresistive nanopillars. *Applied Physics Letters*, 102(4):042409, 2013.
- [31] D. C. Worledge, G. Hu, David W. Abraham, J. Z. Sun, P. L. Trouilloud, J. Nowak, S. Brown, M. C. Gaidis, E. J. OSullivan, and R. P. Robertazzi. Spin torque switching of perpendicular tacofebmgo-based magnetic tunnel junctions. *Applied Physics Letters*, 98(2):022501, 2011.
- [32] T. Kishi, H. Yoda, T. Kai, T. Nagase, E. Kitagawa, M. Yoshikawa, K. Nishiyama, T. Daibou, M. Nagamine, M. Amano, S. Takahashi, M. Nakayama, N. Shimomura, H. Aikawa, S. Ikegawa, S. Yuasa, K. Yakushiji, H. Kubota, A. Fukushima, M. Oogane, T. Miyazaki, and K. Ando. Lower-current and fast switching of a perpendicular tmr for high speed and high density spin-transfer-torque mram. In *2008 IEEE International Electron Devices Meeting*, pages 1–4, Dec 2008.
- [33] T. Maruyama, Y. Shiota, T. Nozaki, K. Ohta, N. Toda, M. Mizuguchi, A. A. Tulapurkar, T. Shinjo, M. Shiraishi, S. Mizukami, Y. Ando, and Y. Suzuki. Large voltage-induced

- magnetic anisotropy change in a few atomic layers of iron. *Nature Nanotechnology*, 4:158 EP –, Jan 2009.
- [34] Wei-Gang Wang, Mingen Li, Stephen Hageman, and C. L. Chien. Electric-field-assisted switching in magnetic tunneljunctions. *Nature Materials*, 11:64 EP –, Nov 2011. Article.
 - [35] MaruyamaT., ShiotaY., NozakiT., OhtaK., TodaN., MizuguchiM., TulapurkarA A., ShinjoT., ShiraishiM., MizukamiS., AndoY., and SuzukiY. Large voltage-induced magnetic anisotropy change in a few atomic layers of iron. *Nat Nano*, 4(3):158–161, Mar 2009.
 - [36] S. Kanai, Y. Nakatani, M. Yamanouchi, S. Ikeda, F. Matsukura, and H. Ohno. In-plane magnetic field dependence of electric field-induced magnetization switching. *Applied Physics Letters*, 103(7):072408, 2013.
 - [37] S. Kanai, Y. Nakatani, M. Yamanouchi, S. Ikeda, H. Sato, F. Matsukura, and H. Ohno. Magnetization switching in a cofeb/mgo magnetic tunnel junction by combining spin-transfer torque and electric field-effect. *Applied Physics Letters*, 104(21):212406, 2014.
 - [38] H. Sato, M. Yamanouchi, S. Ikeda, S. Fukami, F. Matsukura, and H. Ohno. Perpendicular-anisotropy cofeb-mgo magnetic tunnel junctions with a mgo/cofeb/ta/cofeb/mgo recording structure. *Applied Physics Letters*, 101(2):022414, 2012.
 - [39] Seung-Eun Lee, Yasutaka Takemura, and Jea-Gun Park. Effect of double mgo tunneling barrier on thermal stability and tmr ratio for perpendicular mtj spin-valve with tungsten layers. *Applied Physics Letters*, 109(18):182405, 2016.
 - [40] H. Sato, M. Yamanouchi, S. Ikeda, S. Fukami, F. Matsukura, and H. Ohno. Mgo/cofeb/ta/cofeb/mgo recording structure in magnetic tunnel junctions with perpendicular easy axis. *IEEE Transactions on Magnetics*, 49(7):4437–4440, July 2013.
 - [41] G. Hu, J. H. Lee, J. J. Nowak, J. Z. Sun, J. Harms, A. Annunziata, S. Brown, W. Chen, Y. H. Kim, G. Lauer, L. Liu, N. Marchack, S. Murthy, E. J. O’Sullivan, J. H. Park, M. Reuter, R. P. Robertazzi, P. L. Trouilloud, Y. Zhu, and D. C. Worledge. Stt-mram with double magnetic tunnel junctions. In *2015 IEEE International Electron Devices Meeting (IEDM)*, pages 26.3.1–26.3.4, Dec 2015.
 - [42] Ioan Mihai Miron, Kevin Garello, Gilles Gaudin, Pierre-Jean Zermatten, Marius V. Costache, Stéphane Auffret, Sébastien Bandiera, Bernard Rodmacq, Alain Schuhl, and Pietro Gambardella. Perpendicular switching of a single ferromagnetic layer induced by in-plane current injection. *Nature*, 476:189 EP –, Jul 2011.
 - [43] Can Onur Avci, Kevin Garello, Ioan Mihai Miron, Gilles Gaudin, Stphane Auffret, Olivier Boulle, and Pietro Gambardella. Magnetization switching of an mgo/co/pt layer by in-plane current injection. *Applied Physics Letters*, 100(21):212404, 2012.

- [44] Michihiko Yamanouchi, Lin Chen, Junyeon Kim, Masamitsu Hayashi, Hideo Sato, Shunsuke Fukami, Shoji Ikeda, Fumihiro Matsukura, and Hideo Ohno. Three terminal magnetic tunnel junction utilizing the spin hall effect of iridium-doped copper. *Applied Physics Letters*, 102(21):212408, 2013.
- [45] Luqiao Liu, Chi-Feng Pai, Y. Li, H. W. Tseng, D. C. Ralph, and R. A. Buhrman. Spin-torque switching with the giant spin hall effect of tantalum. *Science*, 336(6081):555–558, 2012.
- [46] Chi-Feng Pai, Luqiao Liu, Y. Li, H. W. Tseng, D. C. Ralph, and R. A. Buhrman. Spin transfer torque devices utilizing the giant spin hall effect of tungsten. *Applied Physics Letters*, 101(12):122404, 2012.
- [47] Murat Cubukcu, Olivier Boulle, Marc Drouard, Kevin Garello, Can Onur Avci, Ioan Mihai Miron, Juergen Langer, Berthold Ocker, Pietro Gambardella, and Gilles Gaudin. Spin-orbit torque magnetization switching of a three-terminal perpendicular magnetic tunnel junction. *Applied Physics Letters*, 104(4):042406, 2014.
- [48] J.C. Slonczewski. Current-driven excitation of magnetic multilayers. *Journal of Magnetism and Magnetic Materials*, 159(1):L1 – L7, 1996.
- [49] Jian-Gang (Jimmy) Zhu and Chando Park. Magnetic tunnel junctions. *Materials Today*, 9(11):36 – 45, 2006.
- [50] Charles Kittel. Interpretation of anomalous larmor frequencies in ferromagnetic resonance experiment. *Phys. Rev.*, 71:270–271, Feb 1947.
- [51] Charles Kittel. On the theory of ferromagnetic resonance absorption. *Phys. Rev.*, 73:155–161, Jan 1948.
- [52] J. C. Sankey, P. M. Braganca, A. G. F. Garcia, I. N. Krivorotov, R. A. Buhrman, and D. C. Ralph. Spin-transfer-driven ferromagnetic resonance of individual nanomagnets. *Phys. Rev. Lett.*, 96:227601, Jun 2006.
- [53] A. A. Tulapurkar, Y. Suzuki, A. Fukushima, H. Kubota, H. Maehara, K. Tsunekawa, D. D. Djayaprawira, N. Watanabe, and S. Yuasa. Spin-torque diode effect in magnetic tunnel junctions. *Nature*, 438(7066):339–342, Nov 2005.
- [54] Jian Zhu, J. A. Katine, Graham E. Rowlands, Yu-Jin Chen, Zheng Duan, Juan G. Alzate, Pramey Upadhyaya, Juergen Langer, Pedram Khalili Amiri, Kang L. Wang, and Ilya N. Krivorotov. Voltage-induced ferromagnetic resonance in magnetic tunnel junctions. *Phys. Rev. Lett.*, 108:197203, May 2012.
- [55] Wei-Gang Wang, Ming Li, Stephen Hageman, and C. L. Chien. Electric-field-assisted switching in magnetic tunnel junctions. *Nat Mater*, 11(1):64–68, Jan 2012.
- [56] Hans T. Nembach, Justin M. Shaw, Carl T. Boone, and T. J. Silva. Mode- and size-dependent landau-lifshitz damping in magnetic nanostructures: Evidence for nonlocal damping. *Phys. Rev. Lett.*, 110:117201, Mar 2013.

- [57] Yong-Tao Slonczewski John C. Buhrman Robert A. Ralph Daniel C. Sankey, Jack C. Cui. Measurement of the spin-transfer-torque vector in magnetic tunnel junctions. *Nat Phys*, 4(1):67–71, Jan 2008.
- [58] A. Helmer, S. Cornelissen, T. Devolder, J.-V. Kim, W. van Roy, L. Lagae, and C. Chappert. Quantized spin-wave modes in magnetic tunnel junction nanopillars. *Phys. Rev. B*, 81:094416, Mar 2010.
- [59] V. V. Naletov, G. de Loubens, G. Albuquerque, S. Borlenghi, V. Cros, G. Faini, J. Grollier, H. Hurdequin, N. Locatelli, B. Pigeau, A. N. Slavin, V. S. Tiberkevich, C. Ulysse, T. Valet, and O. Klein. Identification and selection rules of the spin-wave eigenmodes in a normally magnetized nanopillar. *Phys. Rev. B*, 84:224423, Dec 2011.
- [60] Xiaoyong Liu, Wenzhe Zhang, Matthew J. Carter, and Gang Xiao. Ferromagnetic resonance and damping properties of cofeb thin films as free layers in mgo-based magnetic tunnel junctions. *Journal of Applied Physics*, 110(3), 2011.
- [61] G. D. Fuchs, J. C. Sankey, V. S. Pribiag, L. Qian, P. M. Braganca, A. G. F. Garcia, E. M. Ryan, Zhi-Pan Li, O. Ozatay, D. C. Ralph, and R. A. Buhrman. Spin-torque ferromagnetic resonance measurements of damping in nanomagnets. *Applied Physics Letters*, 91(6), 2007.
- [62] Christopher J. Safranski, Yu-Jin Chen, Ilya N. Krivorotov, and Jonathan Z. Sun. Material parameters of perpendicularly magnetized tunnel junctions from spin torque ferromagnetic resonance techniques. *Applied Physics Letters*, 109(13):132408, 2016.
- [63] Xiaoyong Liu, Wenzhe Zhang, Matthew J. Carter, and Gang Xiao. Ferromagnetic resonance and damping properties of cofeb thin films as free layers in mgo-based magnetic tunnel junctions. *Journal of Applied Physics*, 110(3):033910, 2011.
- [64] A. M. Goncalves, I. Barsukov, Y.-J. Chen, L. Yang, J. A. Katine, and I. N. Krivorotov. Spin torque ferromagnetic resonance with magnetic field modulation. *Applied Physics Letters*, 103(17), 2013.
- [65] H. C. Tong, C. Qian, L. Miloslavsky, S. Funada, X. Shi, F. Liu, and S. Dey. The spin flop of synthetic antiferromagnetic films. *Journal of Applied Physics*, 87(9):5055–5057, 2000.
- [66] César L. Ordóñez Romero, Boris A. Kalnikos, Pavol Krivosik, Wei Tong, Pavel Kabos, and Carl E. Patton. Three-magnon splitting and confluence processes for spin-wave excitations in yttrium iron garnet films: Wave vector selective brillouin light scattering measurements and analysis. *Phys. Rev. B*, 79:144428, Apr 2009.
- [67] Eric R. Evarts, Matthew R. Pufall, and William H. Rippard. Continuous-film vs. device-level ferromagnetic resonance in magnetic tunnel junction thin films. *Journal of Applied Physics*, 113(8):083903, 2013.

- [68] Motoya Shinozaki, Eriko Hirayama, Shun Kanai, Hideo Sato, Fumihiro Matsukura, and Hideo Ohno. Damping constant in a free layer in nanoscale cofeb/mgo magnetic tunnel junctions investigated by homodyne-detected ferromagnetic resonance. *Applied Physics Express*, 10(1):013001, 2017.
- [69] M. J. Donahue and D. G. Porter. OOMMF User's Guide, Version 1.0, 1999.
- [70] Sankha S. Mukherjee, Feiming Bai, David MacMahon, Chih-Ling Lee, Surendra K. Gupta, and Santosh K. Kurinec. Crystallization and grain growth behavior of cofeb and mgo layers in multilayer magnetic tunnel junctions. *Journal of Applied Physics*, 106(3):033906, 2009.
- [71] S. Ikeda, K. Miura, H. Yamamoto, K. Mizunuma, H. D. Gan, M. Endo, S. Kanai, J. Hayakawa, F. Matsukura, , and H. Ohno. *Nature Mater.*, 9:721, 2010.
- [72] R. D. McMichael and M. D. Stiles. Magnetic normal modes of nanoelements. *Journal of Applied Physics*, 97(10), 2005.
- [73] S. Petit, C. Baraduc, C. Thirion, U. Ebels, Y. Liu, M. Li, P. Wang, and B. Dieny. Spin-torque influence on the high-frequency magnetization fluctuations in magnetic tunnel junctions. *Phys. Rev. Lett.*, 98:077203, Feb 2007.
- [74] Valeri Synogatch, Neil Smith, and J. R. Childress. Ferromagnetic resonance in tunnel junctions: Mag-noise and complex impedance analysis. *Journal of Applied Physics*, 93(10):8570–8572, 2003.
- [75] Y.-T. Cui, G. Finocchio, C. Wang, J. A. Katine, R. A. Buhrman, and D. C. Ralph. Single-shot time-domain studies of spin-torque-driven switching in magnetic tunnel junctions. *Phys. Rev. Lett.*, 104:097201, Mar 2010.
- [76] J. Z. Sun, R. P. Robertazzi, J. Nowak, P. L. Trouilloud, G. Hu, D. W. Abraham, M. C. Gaidis, S. L. Brown, E. J. O'Sullivan, W. J. Gallagher, and D. C. Worledge. Effect of subvolume excitation and spin-torque efficiency on magnetic switching. *Phys. Rev. B*, 84:064413, Aug 2011.
- [77] J.Z Sun. Current-driven magnetic switching in manganite trilayer junctions. *Journal of Magnetism and Magnetic Materials*, 202(1):157 – 162, 1999.
- [78] T. Min, J. Z. Sun, R. Beach, D. Tang, and P. Wang. Back-hopping after spin torque transfer induced magnetization switching in magnetic tunneling junction cells. *Journal of Applied Physics*, 105(7), 2009.
- [79] J. Z. Sun, M. C. Gaidis, G. Hu, E. J. OSullivan, S. L. Brown, J. J. Nowak, P. L. Trouilloud, and D. C. Worledge. High-bias backhopping in nanosecond time-domain spin-torque switches of mgo-based magnetic tunnel junctions. *Journal of Applied Physics*, 105(7), 2009.

- [80] Zihui Wang, Yuchen Zhou, Jing Zhang, and Yiming Huai. Bit error rate investigation of spin-transfer-switched magnetic tunnel junctions. *Applied Physics Letters*, 101(14), 2012.
- [81] Eric R. Evarts, Ranko Heindl, William H. Rippard, and Matthew R. Pufall. Correlation of anomalous write error rates and ferromagnetic resonance spectrum in spin-transfer-torque-magnetic-random-access-memory devices containing in-plane free layers. *Applied Physics Letters*, 104(21), 2014.
- [82] C Wang, H Seinige, and M Tsoi. Current-driven parametric resonance in magnetic multilayers. *Journal of Physics D: Applied Physics*, 46(28):285001, 2013.
- [83] J. Sampaio, A. V. Khvalkovskiy, M. Kuteifan, M. Cubukcu, D. Apalkov, V. Lomakin, V. Cros, and N. Reyren. Disruptive effect of dzyaloshinskii-moriya interaction on the magnetic memory cell performance. *Applied Physics Letters*, 108(11), 2016.
- [84] H. Sato, M. Yamanouchi, K. Miura, S. Ikeda, R. Koizumi, F. Matsukura, and H. Ohno. Cofeb thickness dependence of thermal stability factor in cofeb/mgo perpendicular magnetic tunnel junctions. *IEEE Magnetics Letters*, 3:3000204–3000204, 2012.
- [85] T. Devolder, L. Bianchini, K. Miura, K. Ito, Joo-Von Kim, P. Crozat, V. Morin, A. Helmer, C. Chappert, S. Ikeda, and H. Ohno. Spin-torque switching window, thermal stability, and material parameters of mgo tunnel junctions. *Applied Physics Letters*, 98(16):162502, 2011.
- [86] T. Devolder, J.-V. Kim, L. Nistor, R. Sousa, B. Rodmacq, and B. Diny. Exchange stiffness in ultrathin perpendicularly magnetized cofeb layers determined using the spectroscopy of electrically excited spin waves. *Journal of Applied Physics*, 120(18):183902, 2016.
- [87] M Beleggia, M De Graef, and Y T Millev. The equivalent ellipsoid of a magnetized body. *Journal of Physics D: Applied Physics*, 39(5):891, 2006.
- [88] Hitoshi Kubota, Akio Fukushima, Kay Yakushiji, Taro Nagahama, Shinji Yuasa, Koji Ando, Hiroki Maehara, Yoshinori Nagamine, Koji Tsunekawa, David D. Djayaprawira, Naoki Watanabe, and Yoshihige Suzuki. Quantitative measurement of voltage dependence of spin-transfer torque in mgo-based magnetic tunnel junctions. *Nature Physics*, 4:37 EP –, Nov 2007.
- [89] Lin Xue, Chen Wang, Yong-Tao Cui, J. A. Katine, R. A. Buhrman, and D. C. Ralph. Network analyzer measurements of spin transfer torques in magnetic tunnel junctions. *Applied Physics Letters*, 101(2):022417, 2012.
- [90] Christian Heiliger and M. D. Stiles. Ab initio studies of the spin-transfer torque in magnetic tunnel junctions. *Phys. Rev. Lett.*, 100:186805, May 2008.
- [91] N. Mecking, Y. S. Gui, and C.-M. Hu. Microwave photovoltaic and photoresistance effects in ferromagnetic microstrips. *Phys. Rev. B*, 76:224430, Dec 2007.

- [92] M. Harder, Z. X. Cao, Y. S. Gui, X. L. Fan, and C.-M. Hu. Analysis of the line shape of electrically detected ferromagnetic resonance. *Phys. Rev. B*, 84:054423, Aug 2011.
- [93] T. Dohi, S. Kanai, F. Matsukura, and H. Ohno. Electric-field effect on spin-wave resonance in a nanoscale cofeb/mgo magnetic tunnel junction. *Applied Physics Letters*, 111(7):072403, 2017.
- [94] M. Yamanouchi, A. Jander, P. Dhagat, S. Ikeda, F. Matsukura, and H. Ohno. Domain structure in cofeb thin films with perpendicular magnetic anisotropy. *IEEE Magnetics Letters*, 2:3000304–3000304, Dec 2011.

Appendix A

Appendix Title

A.1 Detailed System Design of Perpendicular station

We have developed one of the most sensitive Spin-torque ferromagnetic resonance perpendicular magnetic stations. Here we describe the detailed system designs.

First of all, here is all the equipments needed to build the out-of-plane magnetic probe station:

1. GMW Dipole Electromagnet Model 3470
2. Kepco bipolar operational power supply model Model 50-8M
3. Cascade RF probe : SG-120um
4. Cascade RPP210-AI probe positioner (both the probe and the positioner are non-magnetic)
5. Sentech Output 720p Cased Camera

Perpendicular ST-FMR station

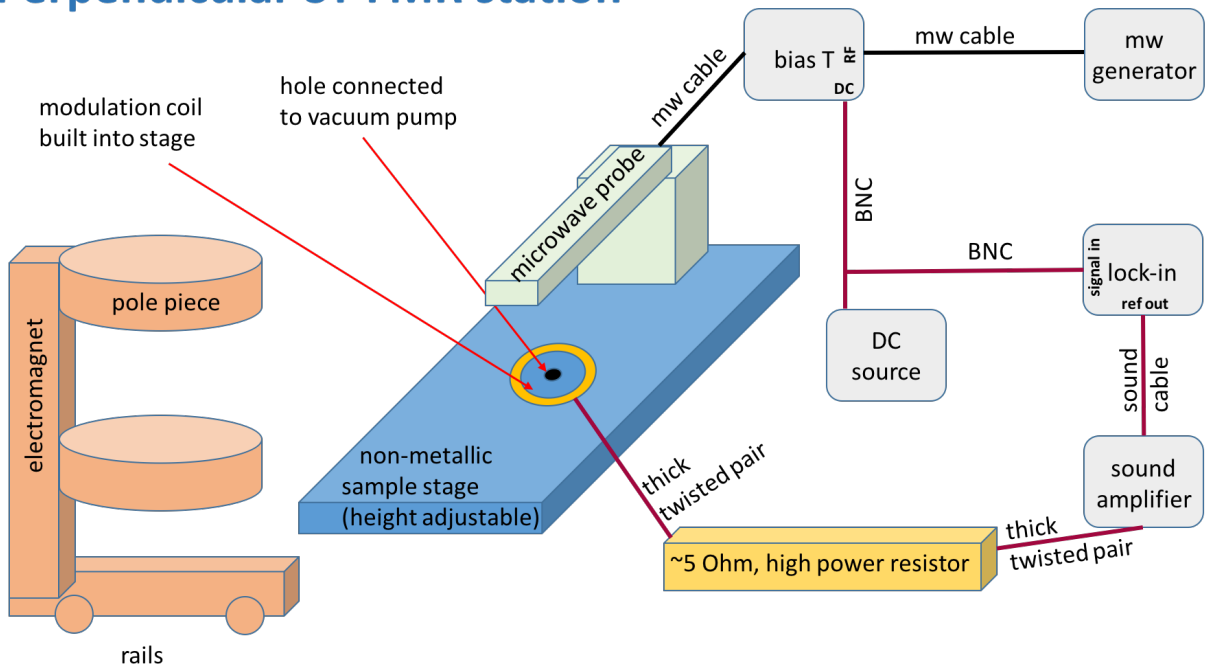


Figure A.1: Perpendicular ST-FMR station Setup

6. Navitar 12X Zoom Lens System

7. AmScope LED-80M 80-LED Microscope Ring Light

Fig.A.1 sketches the design of the out-of-plane station. The magnet is fixed vertically on metal frame and the stage height is adjustable. At first, we can land the probe to make contact of the sample with the magnet moving away(shown in Fig.A.2(a)). After making contact of the sample, first remove the camera (the setup could be improved by making a stationary camera). Then we can slide in the magnet so that the sample is located in the center of the magnet. It is important not to touch the probe and microwave cable when sliding the magnet. After moving the magnet we are ready to make ST-FMR measurement as showing in Fig.A.2(b).

Here is the list of equipments needed for making ST-FMR measurements up to 40 GHz.

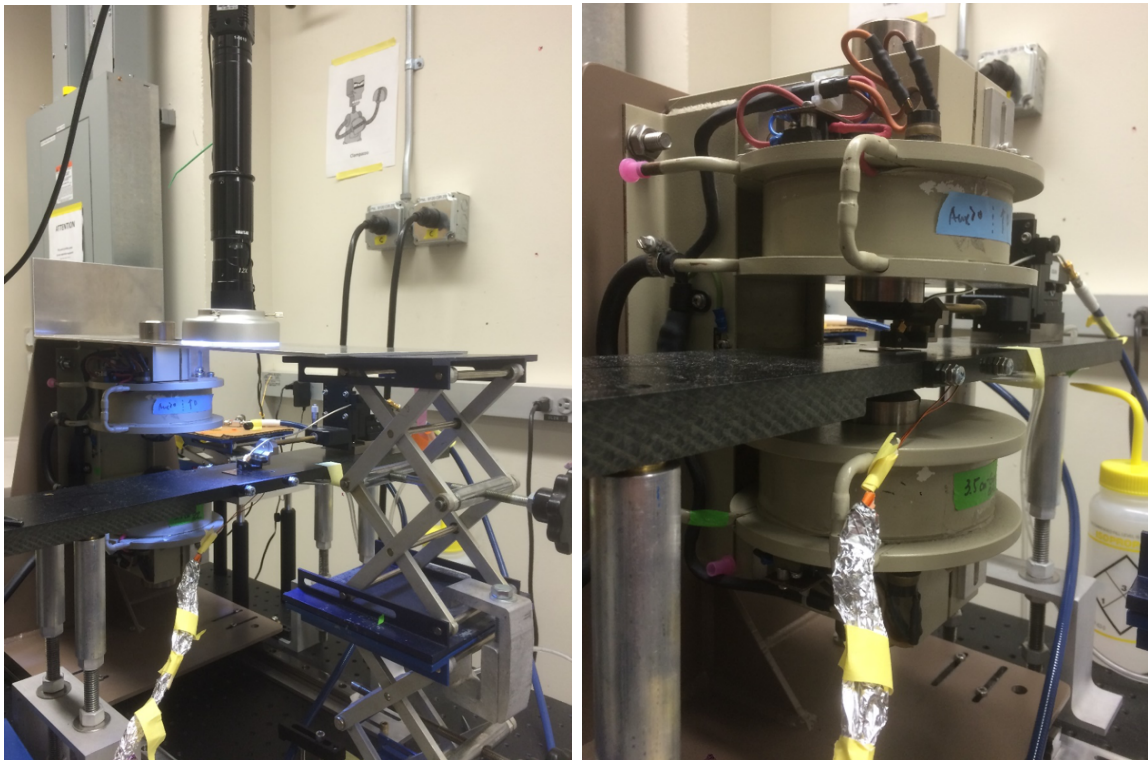


Figure A.2: Operation of Out-of-plane probe station

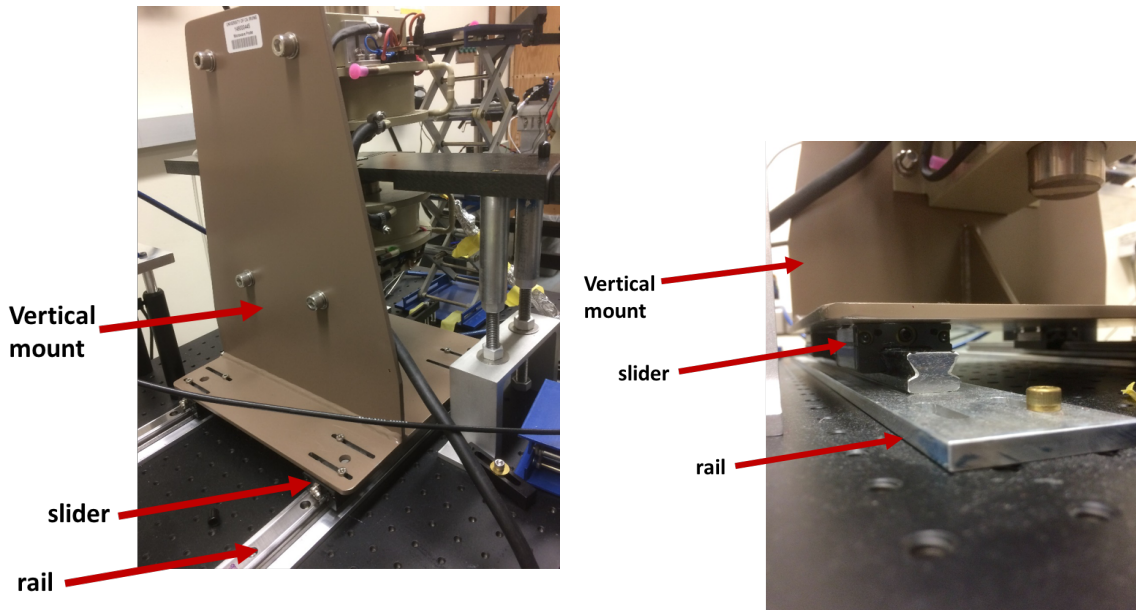


Figure A.3: (a) Side view of the magnet. (b) Bottom view of the magnet

1. Signal recovery 7225 DSP lock-in Amplifier
2. Hittite HMC-T2240 synthesized signal generator, 10 MHz to 40 GHz
3. Clear Microwave Broadband Bias Tee BT50K40 50Khz-40GHz
4. Keithley 2400 Source Meter (DC Source)
5. Microwave cable : Teledyne Accutest R95-0004-072 (72 inch 1GHz- 40GHz)
6. Pomona BNC cables

When connecting the microwave cables, there are two small things worth notice. Firstly, all the connectors should be cleaned regularly. Secondly, the microwave cables should be supported to release all the possible tensions.

The last pieces of equipments needed is the field modulation setup. Here is the list:

1. Behringer EUROPOWER Professional 4,000-Watt Stereo Power Amplifier
2. TE CONNECTIVITY / CGS CJT10004R7JJ Through Hole Wire wound Resistor, 4.7 Ohm
3. High quality cable connecting from lock-in to the input of the sound amplifier : Monster Performer 500 - 10' Speaker Cable
4. BK Precision 2831E Ammeter to control the current through the copper wire

When making the field-modulation coil, it is better to use any low resistance copper wire for magnetic field modulation coil. For out-of-plane field modulations, we use an external coil above the sample as shown in Fig.A.4(a). In-plane field modulation can be achieved by simply placing straight wire above the sample as shown in Fig.A.4(b). In our current design,

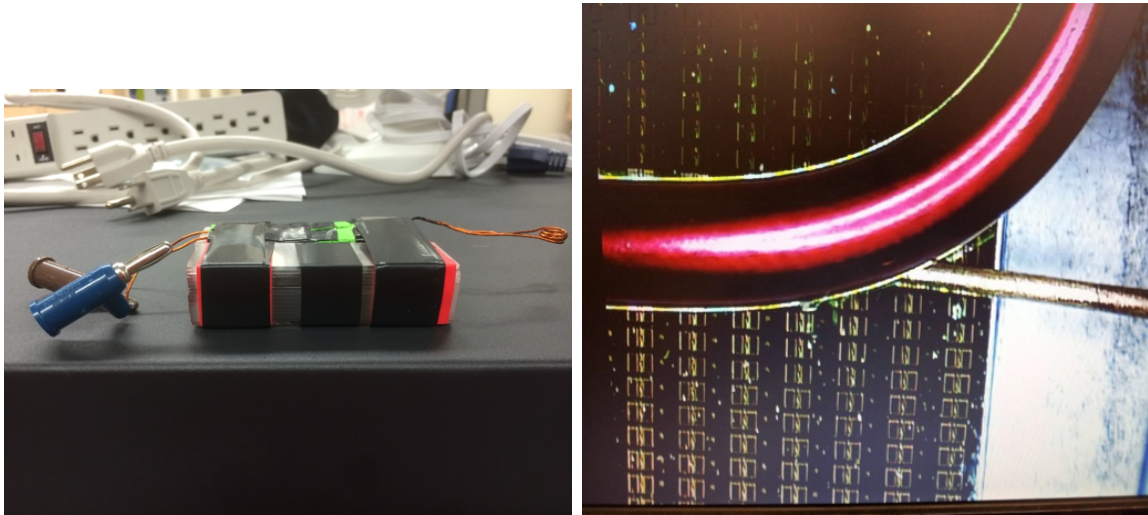


Figure A.4: (a) Coil for out-of-plane modulation (b) Wire for in-plane modulation

we embed the coil into the plastic base right under the sample. It is important to ensure that the wire is not in contact with the sample or any other parts of the microwave setup.

In the experiment, two parameters need to be determined for the field modulation: the amplitude of modulation field and the frequency of the modulation ac field. Typically Increasing the modulation field increases the signal amplitude, but not infinitely as shown in Fig.A.5(a). If you are over-modulating, the signal becomes distorted and the linewidth broadens as shown in Fig.A.5(b). In our current setup, the input ac current is about 3.6 A to achieve the modulation field around a few oersted field, which is enough to have decent signal-to-noise ratio without distorting the spectrum.

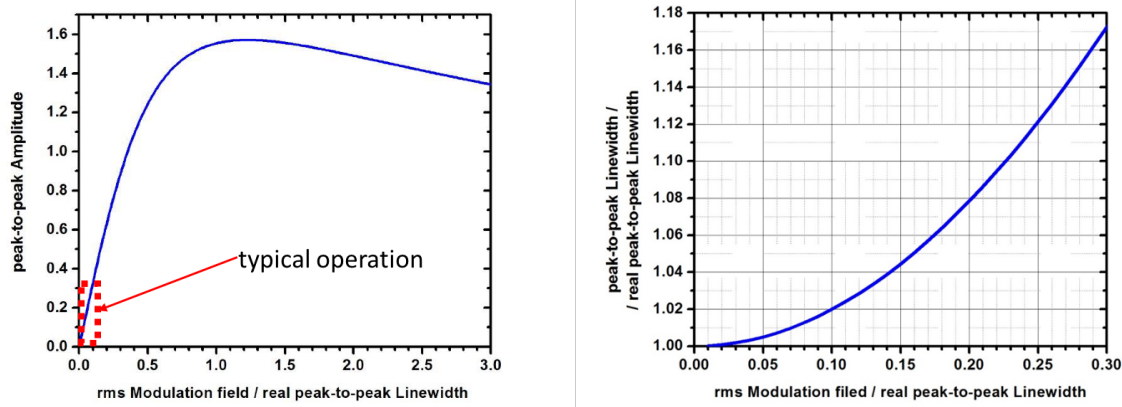


Figure A.5: (a) Peak-to-peak amplitude versus rms modulation field over real peak-to-peak linewidth. (b) peak-to-peak linewidth over real peak-to-peak linewidth versus rms modulation field over real peak-to-peak linewidth.

Mode 0	10.98	11.92	11.57	11.98	10.94	11.71	10.94	11.84	11.38	11.8	12.09
Mode 1	12.85	14.6	13.98	14.64	13.21	14.28	13.05	13.6	14.29	14.66	14.01
Mode 2	13.75	15	15.4	15.33	13.2	15.48	13.66	14.57	14.86	15.24	14.18
Gap 0-1	1.87	2.68	2.41	2.66	2.27	2.57	2.11	1.76	2.91	2.86	1.92
Gap 0-2	2.77	3.08	3.83	3.35	2.26	3.77	2.72	2.73	3.48	3.44	2.09
Gap (1+2)/2 - 0	2.32	2.88	3.12	3.005	2.265	3.17	2.415	2.245	3.195	3.15	2.005

Table A.1: C06 70nm summary

Mode 0	9.83	10.5	11.05	10.54	11.89	11.39	11.2	10.39	10.61	10.39	11.07
Mode 1	11.76	12.68	13.24	12.61	13.78	13.6	13.19	12.85	13.47	12.6	13.02
Mode 2	12.71	13.04	13.86	13.04	14.88	14.29	13.5	14.06	13.79	12.99	13.99
Gap 0-1	1.93	2.18	2.19	2.07	1.89	2.21	1.99	2.46	2.86	2.21	1.95
Gap 0-2	2.88	2.54	2.81	2.5	2.99	2.9	2.3	3.67	3.18	2.6	2.92
Gap (1+2)/2 - 0	2.405	2.36	2.5	2.285	2.44	2.555	2.145	3.065	3.02	2.405	2.435

Table A.2: C07 80nm Summary

A.2 Statitscs of mode position of circular devices

Mode 0	9.94	10.19	9.28	10.54	9.14	9.14	9.6	9.77	9.13	10.51
Mode 1	11.65	12.41	10.93	12.29	11.2	11.2	12.07	11.8	10.69	11.96
Mode 2	12.15	12.66	12.07	12.29	12.05	12.05	12.36	12.9	11.26	12.65
Gap 0-1	1.71	2.22	1.65	1.75	2.06	2.06	2.47	2.03	1.56	1.45
Gap 0-2	2.21	2.47	2.79	1.75	2.91	2.91	2.76	3.13	2.13	2.14
Gap 0-(1,2)	1.96	2.345	2.22	1.75	2.485	2.485	2.615	2.58	1.845	1.795

Table A.3: C08 90nm summary

Mode 0	7.88	9.62	9.09	8.97	9.07	8.84	9.24	8.35	8.75	8.77	7.96
Mode 1	9.55	11.4	10.43	10.36	10.4	10.25	10.47	10.23	10.35	10.57	9.89
Mode 2	9.96	11.59	10.52	11.2	10.7	10.52	11.8	10.59	11.31	10.61	10.49
Gap 0-1	1.67	1.78	1.34	1.39	1.33	1.41	1.23	1.88	1.6	1.8	1.93
Gap 0-2	2.08	1.97	1.43	2.23	1.63	1.68	2.56	2.24	2.56	1.84	2.53
Gap 0-(1,2)	1.875	1.875	1.385	1.81	1.48	1.545	1.895	2.06	2.08	1.82	2.23

Table A.4: C09 120 nm

Mode 0	8.02	7.61	7.81	8.13	7.86	7.94	7.85	7.46	7.18	8.33	8.73	7.98	7.65
Mode 1	9.71	8.8	9.36	9.13	9.27	9.37	9.16	8.79	8.13	9.3	9.73	9.14	8.77
Mode 2	9.9	8.96	9.83	9.81	9.52	9.37	9.44	9.42	8.71	9.91	10.22	9.6	9.21
Gap 0-1	1.69	1.19	1.55	1	1.41	1.43	1.31	1.33	0.95	0.97	1	1.16	1.12
Gap 0-2	1.88	1.35	2.02	1.68	1.66	1.43	1.59	1.96	1.53	1.58	1.49	1.62	1.56
Gap 0-(1,2)	1.785	1.27	1.785	1.34	1.535	1.43	1.45	1.645	1.24	1.275	1.245	1.39	1.34

Table A.5: C10 150 nm summary